Integrated Sensors for Process Monitoring and Health Monitoring in Microsystems

Yufei Liu

A thesis submitted for the degree of Doctor of Philosophy

Heriot-Watt University

School of Engineering and Physical Sciences

April 2011

Abstract

This thesis presents the development of integrated sensors for health monitoring in Microsystems, which is an emerging method for early diagnostics of status or "health" of electronic systems and devices under operation based on embedded tests. Thin film meander temperature sensors have been designed with a minimum footprint of 240 μm × 250 μm. A microsensor array has been used successfully for accurate temperature monitoring of laser assisted polymer bonding for MEMS packaging. Using a frame-shaped beam, the temperature at centre of bottom substrate was obtained to be ~50 ℃ lower than that obtained using a top-hat beam. This is highly beneficial for packaging of temperature sensitive MEMS devices. Polymer based surface acoustic wave humidity sensors were designed and successfully fabricated on 128 ° cut lithium niobate substrates. Based on reflection signals, a sensitivity of 0.26 dB/RH% was achieved between 8.6 %RH and 90.6 %RH. Fabricated piezoresistive pressure sensors have also been hybrid integrated and electrically contacted using a wire bonding method. Integrated sensors based on both $LiNbO_3$ and ZnO/Si substrates are proposed. Integrated sensors were successfully fabricated on a $LiNbO_3$ substrate with a footprint of 13 mm × 12 mm, having multi monitoring functions for simultaneous temperature, measurement of humidity and pressure in the health monitoring applications.

Declaration

I hereby declare that this thesis is based on my original work except for quotations and citations which have been duly acknowledged, which was mainly carried out at the Joint Research Institute for Integrated Systems (IIS) of the Edinburgh Research Partnership in Engineering and Mathematics (ERPem), between School of Engineering and Physical Sciences (EPS) in Heriot-Watt University and Institute for Integrated Micro and Nano Systems (IMNS) in University of Edinburgh. I also declare that this thesis has not been submitted for any other degree, at these, or any other universities. Some material of this thesis may also appear in the author's publications listed on page ix.

<div align="right">

Yufei Liu

April 2011

</div>

Acknowledgements

ACADEMIC REGISTRY
Research Thesis Submission

Name:	YUFEI LIU		
School/PGI:	School of Engineering and Physical Sciences		
Version: *(i.e. First, Resubmission, Final)*	Final	Degree Sought (Award and Subject area)	Doctor of Philosophy

Declaration

In accordance with the appropriate regulations I hereby submit my thesis and I declare that:

1) the thesis embodies the results of my own work and has been composed by myself
2) where appropriate, I have made acknowledgement of the work of others and have made reference to work carried out in collaboration with other persons
3) the thesis is the correct version of the thesis for submission and is the same version as any electronic versions submitted*.
4) my thesis for the award referred to, deposited in the Heriot-Watt University Library, should be made available for loan or photocopying and be available via the Institutional Repository, subject to such conditions as the Librarian may require
5) I understand that as a student of the University I am required to abide by the Regulations of the University and to conform to its discipline.

* Please note that it is the responsibility of the candidate to ensure that the correct version of the thesis is submitted.

Signature of Candidate:	*Yufei Liu*	Date:	

Submission

Submitted By *(name in capitals):*	YUFEI LIU
Signature of Individual Submitting:	*Yufei Liu*
Date Submitted:	

For Completion in Academic Registry

Received in the Academic Registry by *(name in capitals):*			
Method of Submission (Handed in to Academic Registry; posted through internal/external mail):			
E-thesis Submitted (**mandatory for final theses from January 2009**)			
Signature:		Date:	

Please note this form should bound into the submitted thesis.

Table of Contents

List of Publications

Yufei Liu, Jun Zeng and Changhai Wang, **Accurate Temperature Monitoring in Laser Assisted Polymer Bonding for MEMS Packaging Using an Embedded Microsensor Array**, *Journal of Microelectromechanical Systems*, Vol. 19 , Issue: 4, Aug 2010, pp. 903-910.

Yufei Liu, Jun Zen, and Changhai Wang, **In-situ temperature monitoring for process control in laser assisted polymer bonding for MEMS packaging,** *in 2nd IEEE Electronics System-Integration Technology Conference, 2008. ESTC 2008 London UK.* pp. 199-204.

Yufei Liu, Jun Zen, and Changhai Wang, **Temperature monitoring in laser assisted polymer bonding for MEMS packaging using a thin film sensor array,** *in IEEE Sensors Applications Symposium, 2009. SAS 2009 New Orleans USA.* pp. 52-55.

Y. Liu, J. Zeng and C.H. Wang, **Temperature Monitoring in Laser Bonding for MEMS Packaging**, *Proceedings of IMAPS MicroTech 2009 on Bio-Sensors and MEMS Packaging, IMAPS 2009 Edinburgh UK.* pp. 87-90.

Changhai Wang, Jun Zen, and Yufei Liu. **Recent advances in laser assisted polymer intermediate layer bonding for MEMS packaging**. *Proceedings of International Conference on Electronic Packaging Technology & High Density Packaging, 2009. ICEPT-HDP 2009. Beijing China.* pp. 31-35.

C.H. Wang, Y. Liu, M. Desmulliez, and A. Richardson. **Integrated sensors for health monitoring in advanced electronic systems**. *Proceedings of 4th International Design and Test Workshop 2009, IDT 2009, Riyadh, Saudi Arabia.* pp. 1-6.

Chapter 1   Introduction

1.1   Background and Motivation

The market for Micro-Electro-Mechanical-Systems (MEMS) has grown steadily over the last decade, with both multi-chip module (MCM), system in package (SiP) and system on chip (SoC) technologies playing more important roles in the integration of MEMS devices and Microsystems. MCM is a specialized electronic package where multiple integrated circuits (ICs), semiconductor dies or other discrete components are packaged onto a unifying substrate and facilitating their use as a single component. As an extension of the MCM concept, SiP technology is a response to the demands for higher level integration and functionality including radio frequency (RF) and non-electrical functions, which supports both the concept of chip stacking (3D integration) and uses substrates that include passives, electrical and non-electrical interconnects and, in the future, active devices. Applications of SiP based microsystems are in areas such as ambient intelligence, intelligent sensing and medical technologies where fault tolerance and self monitoring are key requirements (e.g. health care, aerospace, implants…) [1-4].

Advanced sensors and monitoring technologies are important in prioritizing the repair and rehabilitation process, improving the cost-effectiveness of inspection and maintenance, and ultimately enhancing the lifetime and safety of the systems. Embedded environmental "health" monitoring has also been implemented in infrastructure systems, such as bridges, highways, buildings, pipelines, and many mechanical structures, such as aerospace vehicles or heavy mining equipment. The failure of such structures can cause large economic loss, and even the loss of lives. By using an array of sensors to continuously monitor such structures, the embedded health monitoring sensors can provide an early indication of problems such as damage to the structure from fatigue, corrosion or impact, and this information can be used to undertake corrective action before the damage develops to a stage where a catastrophic failure occurs [5-9].

Most of the component technologies required for heterogeneous microsystems exist but the integration and associated manufacture of these systems places major challenges on the test and reliability validation processes. Embedded health monitoring in

Microsystems will initiate research into the possibility of realizing a methodology to support low-cost integration of functions able to self-test components and system interconnects during production testing. It will also allow monitoring of key parameters in mission mode and provide a level of fault tolerance / self-repair. This work will build on low cost self-test concepts for MEMS and study both fault modeling and structural reliability for Microsystems technologies.

In this thesis, the embedded health monitoring sensors have been investigated, which could be used to monitor the key faults and degradation behaviour in environmental parameters correlated with system reliability variations in mission mode. Besides the application of health monitoring in Microsystems, there are also huge demands for integrated sensors for normal environmental monitoring, e.g. the temperature, humidity, and pressure monitoring at airports and motorways. Both sensing and testing functions have been studied together with the test control and access infrastructure for the abilities of self monitoring and self repairing. The research work includes the potential to realize:

1. temperature, humidity and pressure/stress sensors for integration in a microsystem health monitoring architecture;
2. integration technologies for health monitoring multi-sensor systems based on silicon and piezoelectric substrates;
3. solutions for embedded sensing;
4. implementation solutions including on-chip and on-substrate;
5. investigation of further applications of the embedded health monitoring sensors.

1.2   Thesis Outline

The diagram of the thesis outline is shown in Fig. 1.1. Chapter 2 introduce the MEMS technology including the MCM and SiP technologies, and presents a research review of the typical sensors used for embedded health monitoring. The review covers different types of temperature sensors, humidity sensors and pressure/stress sensors.
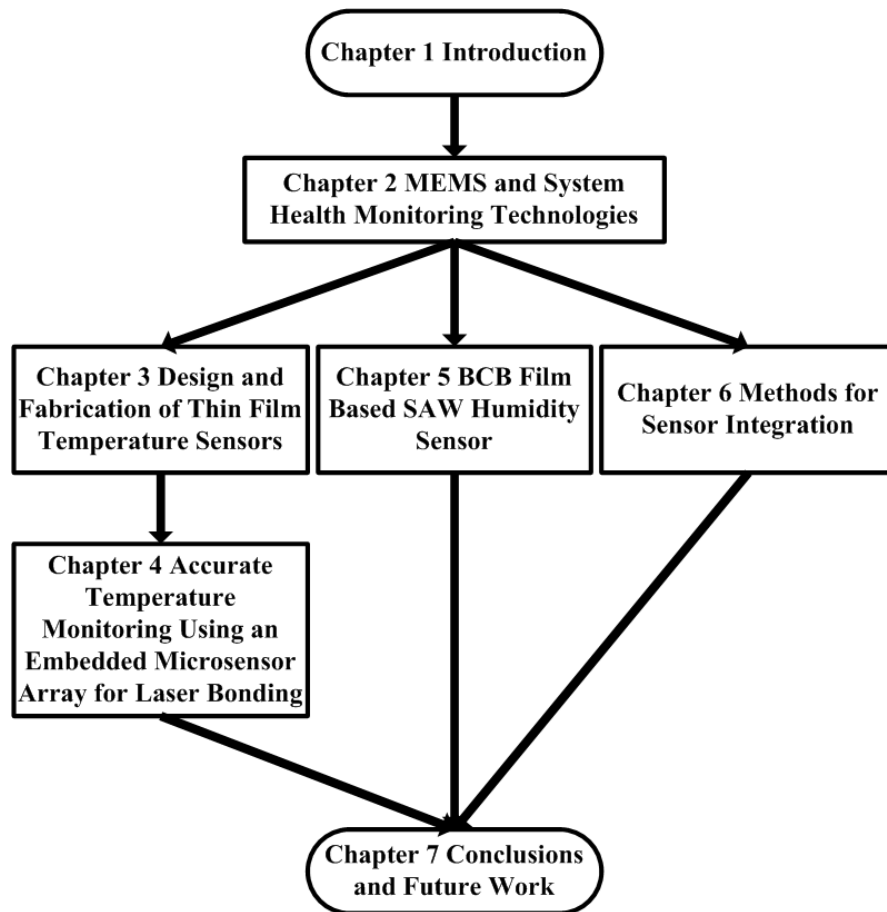
Figure 1.1 Diagram of thesis outline.

Chapter 3 describes the design, fabrication and testing of the metal based thin film temperature sensors, which have been designed in meander structures with track widths of 3, 5, 7 and 10 μm. Based on the finite element method (FEM) simulation, a photomask has been designed and produced on the soda-line glass substrates. During the devices fabrication, a platinum layer, deposited by sputtering and patterned by ion-beam etching, was fabricated as the temperature sensing film. Nickel was also selected for the fabrication of the thin film temperature sensors. Nickel was deposited by electron beam evaporation and patterned using a wet etching process. The footprint of the successfully fabricated thin film temperature sensor with 3 μm track width was only 240 μm $\times$ 250 μm. The platinum based thin film temperature sensors displayed a linear response to temperature between 25°C and 375°C.

Chapter 4 presents an experimental study of an embedded accurate processing temperature monitoring of laser assisted polymer bonding for MEMS packaging, using an embedded thin film microsensor array. The work was carried out using a fibre coupled diode laser system and the benzocyclobutene (BCB) polymer as the bonding

material. The BCB has been cured by laser heating and for creating the sealed cavities for housing the MEMS devices. To create the top-hat and frame shaped laser beam profiles, the beam forming optical elements were used. In the sensor array, the peripheral sensors were embedded underneath the polymer sealing rings which allow precise monitoring of the temperature profile of the polymer track during the laser assisted BCB curing. The sensor at the centre of the sensor array monitored the temperature that would be experienced by a MEMS device in manufacturing environments. The results show that accurate temperature monitoring can be obtained using the embedded sensor arrays. A lower temperature was obtained at the centre of the bottom (device) substrate than the bonding temperature of the polymer ring. This is a highly desirable effect for packaging of temperature sensitive devices. In addition, the effects of substrate material and heat dissipation on the resultant temperature profiles have been investigated.

Chapter 5 studies the design and fabrication of the surface acoustic wave (SAW) based humidity sensors, based on the summaries of the BCB moisture absorption ability and the principals of piezoelectric effect and SAW sensing. After studies of the equivalent circuit, behaviour modelling and the power consumption analysis of the SAW sensors, inter-digital transducer (IDT) fingers, with width of 4, 8 and 16 μm, were fabricated both on bulk materials such as $LiNbO_3$ and thin film layers such as ZnO on top of silicon wafers. Both these materials are piezoelectric and it is this property which is exploited in the humidity sensor. The SAW, created by the IDTs on the piezoelectric substrates, is sensitive to the mass loading effect caused by the moisture absorption, which results in a resonance frequency shift and changes of the wave amplitude. CYCLOTENE 4000 resins (Photo-BCB) supplied by Dow Chemical have been selected as the moisture absorption layer coated to the SAW sensors on the piezoelectric substrates. The transmission and reflection signals of the fabricated sensors were measured using a HP8510 Network Analyzer.

Chapter 6 firstly investigates the hybrid integration of the piezoresistive pressure sensors. The process flow of the multi-sensor integration based on both $LiNbO_3$ and ZnO/Si substrates have been proposed, and the integrated sensors as a single chip on the $LiNbO_3$ substrates have been successfully fabricated. The IDTs of SAW humidity sensors were fabricated using depositing aluminium and wet etching process, while the contact pads of the pressure sensors were produced at the same time. Either platinum

deposited using sputtering and patterned with ion-beam etching process or nickel deposited using electro-beam evaporation and patterned with wet etching process. Finally, the piezoresistive pressure sensors have been integrated using the hybrid integration and then connected to the electrical pads using wire bonding.

Chapter 7 is the conclusion of this thesis and the discussion of the future work. Long term stability of SAW based humidity sensor and fabricated temperature monitoring micro-chip are shown and discussed as the future work.

Chapter 2   MEMS and System Health Monitoring Technologies

2.1   Micro-Electro-Mechanical Systems (MEMS) Technology

Micro-electro-mechanical systems (MEMS) are small integrated devices or systems that combine electrical and mechanical components. The foundation of MEMS technology is the capability of creating controllable, mechanical, moveable structures using IC processing technology [10]. MEMS technology is about high-level integration of dissimilar functions including motion, light, sound, electromagnetic radiation and analysis of data. Computation, analysis and central control of these input/output functions could result in a fully integrated system of incredible versatility [11]. The development of MEMS technology can be traced back to Richard P. Feynman, the Nobel Physics Prize winner, who gave a talk "There's Plenty of Room at the Bottom" on 29th Dec. 1959 at the annual meeting of the American Physical Society [12]. Both the scale and roadmap of MEMS are shown in Fig. 2.1 and Fig. 2.2 [13]. The development of MEMS and related technologies are shown as follows [13-15],

- 1954: The piezoresistive effect of silicon and germanium reported by C.S. Smith. Silicon-based pressure sensors have been widely produced since this discovery.
- 1958: Silicon strain gauges commercially available.
- 1959: R. Feynman famous talk: "There is plenty of room at the bottom".
- 1961: The first silicon strain gauges were integrated on a thin silicon substrate as diffused resistors by Kulite.
- 1967: Invention of surface micromachining (Nathanson, Resonant Gate Transistor).
- 1970: First silicon accelerometer demonstrated (Kulite).
- 1970: Silicon-glass bonding technology.
- 1977: First capacitive pressure sensor (Stanford).
- 1977: IBM – HP : Micro-machined Ink Jet Nozzle.
- 1978: Silicon Bulk Micromachining: K. Bean.
- 1978: Structure obtained by Micromoulding (LIGA).
- 1982: Famous review paper "Silicon as a Mechanical material" (K. Petersen).

- 1984:   First polysilicon MEMS device (M. Howe).
- 1985:   Assembly of silicon wafers (Si/Si fusion bonding): Lasky, et al.
- 1985:   IC-compatible surface micromachining: Polysilicon comb structures.
- 1988:   Electrostatic micromotor (UC -Berkeley BSAC).
- 1988:   First MEMS conference (1st Transducers conference was held in 1987).
- 1993:   First surface micromachined accelerometer (ADXL50) sold, (Analog Devices).
- 1998:   Technologies standard.
- 2000:   MEMS becomes a growing market: A huge number of MEMS Start-up.
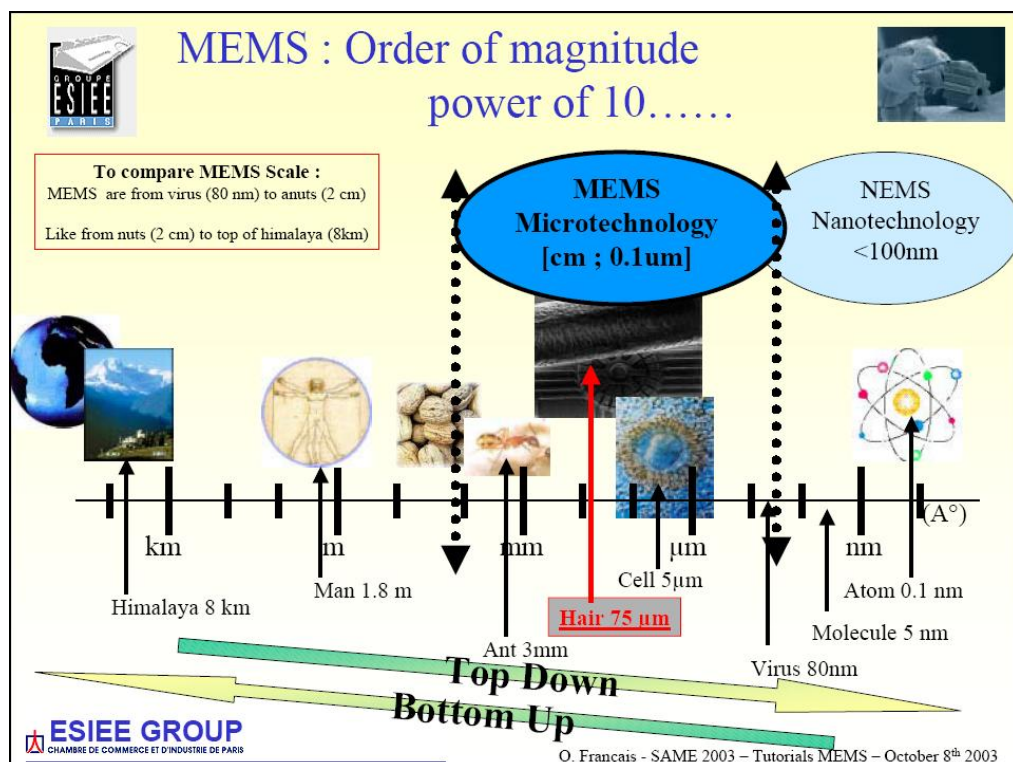
Figure 2.1 The scale of MEMS technology [13].
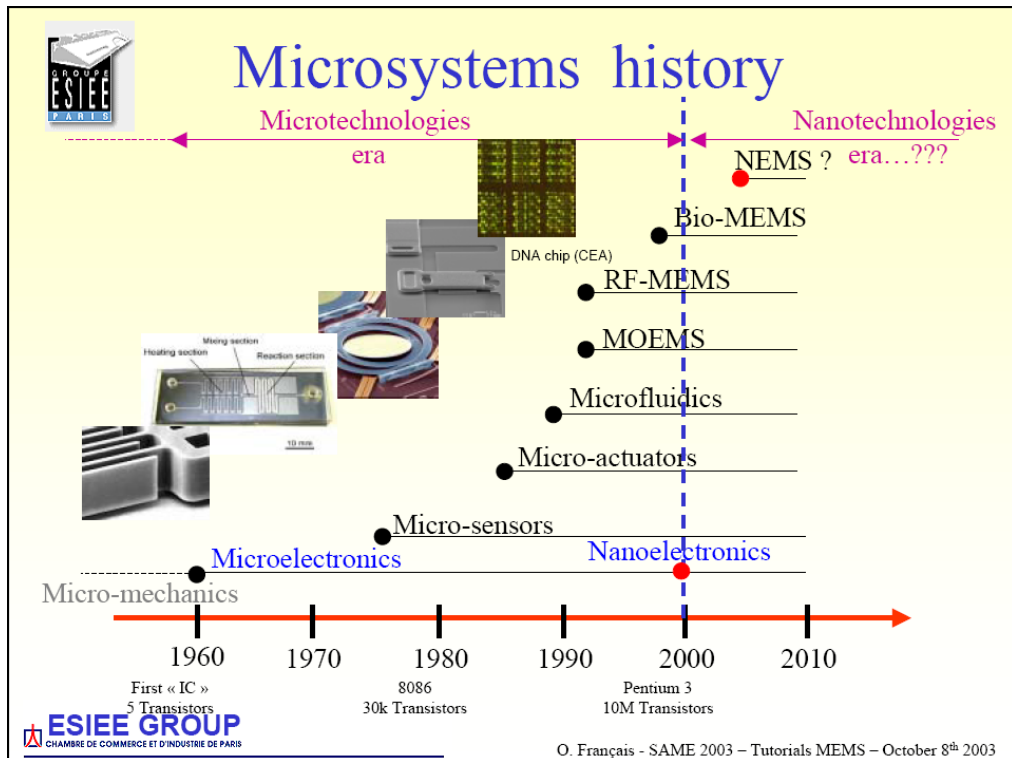
Figure 2.2 The roadmap of MEMS technology [13].

MEMS technology has developed rapidly due to following advantages: high reliability, small scale, multifunctional, light weight, low power consumption, less consumption of natural resources, high-volume and low-cost production, high integration and specialised manufacture. MEMS technology has been commonly regarded as a general strategy of success, not only for electronic components and systems but also for a huge variety of mechanical, optical, acoustic, thermal, fluidic, chemical, and biochemical functional units [16-18]. These "smart sensors" monitor and control the function of critical systems and components in order to ensure safe and efficient operation. They are also playing important roles in prioritising the repair and rehabilitation process and improving the cost-effectiveness of inspection and maintenance of systems, such as in civil infrastructure systems, turbine engines and bearings. The demands for autonomous health monitoring capability depend on the risk associated with system failure and the potential benefit of timely response to faulted or degraded operations [19-23]. Typical MEMS "smart sensors" contain acceleration sensors, pressure sensors, temperature sensors, flow sensors, chemical sensors, biosensors, ink jet printer heads, read write heads, optical network components, nano-tools, micro-relays, micro-pumps, and micro-motors. The MEMS and integrated MEMS devices have already been widely used in the automotive industry, optical interconnection technology, aerospace, information technology, safety and security, process control, machine vision, automation,

environmental monitoring, biotechnology, pharmaceutical industry, water, gas supply, science, and consumer products. high level integration of MEMS devices makes it possible to integrate multi-sensors, functional actuators and control circles together into a single chip or a single package in a real Microsystem [16-23].

MEMS technology is based on the techniques and theories of system-techniques, micro-techniques and materials [24]. The details are shown in Fig. 2.3. Microfabrication is the core of MEMS technologies, which is also one of most active research areas of MEMS technology. The main fabrication processes of MEMS include surface micromachining developed on from microelectronics processing technology, bulk micromachining for silicon fabrication, wafer bonding technology and non-silicon micromachining [25].
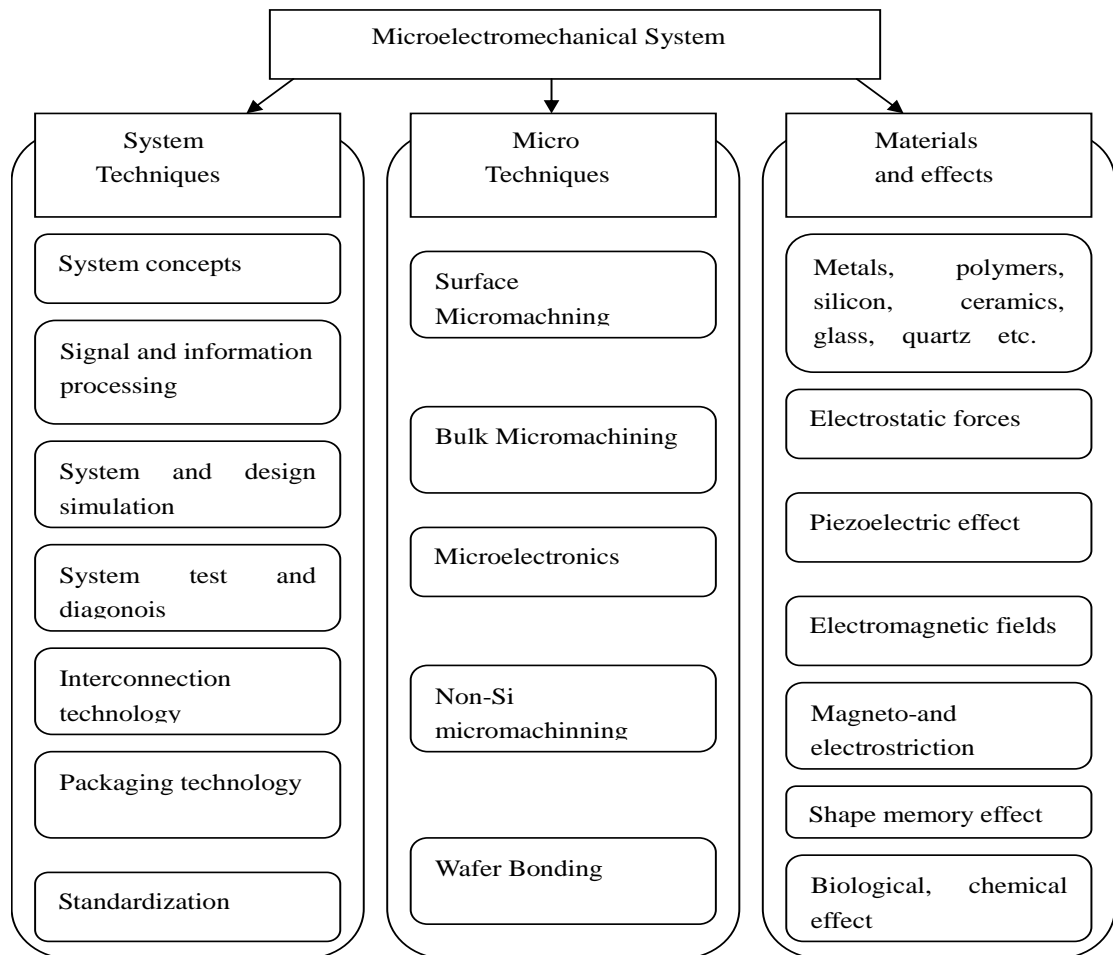
Figure 2.3 The technical and theoretical foundations of MEMS [24].

2.1.1 Surface Micromachining

Surface micromachining is characterised by the fabrication of micromechanical structures by deposition and etching of thin structural and sacrificial films. Originally employed for integrated circuits processes, films composed of materials such as polysilicon, silicon nitride and silicon dioxides can be sequentially deposited and selectively removed to build or "machine" three-dimensional structures [26]. Thus, simple microstructures like beams or membranes as well as complex structures like linkages or encapsulated resonators can be fabricated on top of a substrate. A processing sequence using polysilicon as micro-structural material and silicon dioxide as sacrificial layer is shown in Fig. 2.4. The main features of the surface micro-machining technology are the small microstructure dimensions and the opportunity to integrate micromechanics and microelectronics on the same chip. There are three key challenges in fabrication of microstructures using surface micromachining [27],

- Control of stress and stress gradients in the structural layer to avoid bending or buckling of the released microstructure.

- High selectivity of the sacrificial layer etchant to functional layers.

- Avoidance of sticking of the released microstructure to the substrate
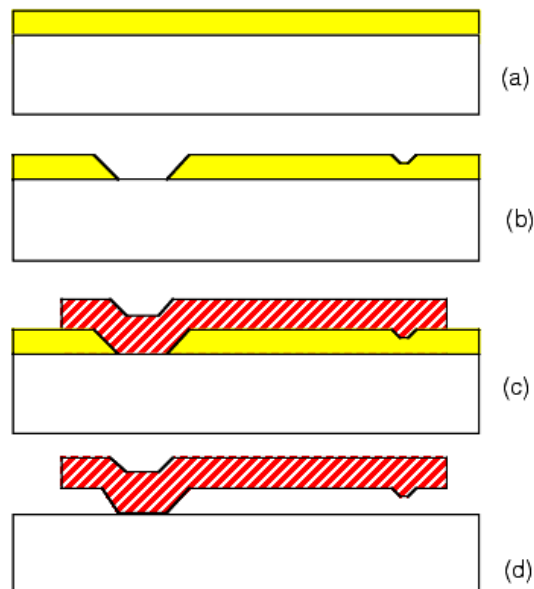
Figure 2.4 Cross-sectional schematic demonstration of surface micromachining [27]
(a) Sacrificial layer deposition; (b) definition of the anchor and bushing regions;
(c) structural layer patterning; and (d) free-standing microstructure after release.

2.1.2 Bulk Micromachining

Silicon bulk micromachining, which is based on a silicon etching and glass-silicon anodic bonding, plays an important role in microfabrication. Three-dimensional

microfabrication is important to develop high performance microactuators and microscale energy sources. A comparison of bulk silicon etchants is shown in Table 2.1. The available etching methods fall into three categories in terms of the state of the etchants: wet, vapor, and plasma processes. Dry etching method is compatible to complementary metal–oxide–semiconductors (CMOS) processing and is being developed for its popularity. Wet etching with alkaline liquid solvents, such as potassium hydroxide (KOH) or tetramethylammonium hydroxide (TMAH), is a relatively simple and inexpensive fabrication technology, and is well suited for applications which do not require much complexity, and which are price sensitive [28-30].

Table 2.1 Comparison of bulk silicon etchants [28].

	HNA (HF+HNO$_3$ +Acetic Acid)	Alkali-OH	EDP (ethylene diamine pyrochat-echol)	TMAH (tetramethyl-ammonium hydroxide)	XeF$_2$	SF$_6$ Plasma	DRIE (Deep Reactive Ion Etch)
Etch Type	wet	wet	wet	wet	dry [1]	dry	dry
Anisotropic?	no	yes	yes	yes	no	varies	yes
Availability	common	common	moderate	moderate	limited	common	limited
Si Etch Rate μm/min	1 to 3	1 to 2	0.02 to 1	≈ 1	1 to 3	≈ 1	> 1
Si Roughness	low	low	low	variable [2]	high [3]	variable	low
Nitride Etch	low	low	low	1 to 10 nm/min	?	low	low
Oxide Etch	10 to 30 nm/min	1 to 10 nm/min	1 to 80 nm/min	≈ 1 nm/min	low	low	low
Al Selective	no	no	no [4]	yes [5]	yes	yes	yes
Au Selective	likely	yes	yes	yes	yes	yes	yes
p++ Etch Stop?	no (n slows)	yes	yes	yes	no	no (some dopant effects)	no
Electrochemical Stop?	?	yes	yes	yes	no	no	no
CMOS Compatible? [6]	no	no	yes	yes	yes	yes	yes
Cost [7]	low	low	moderate	moderate	moderate	high	high
Disposal	low	easy	difficult	moderate	N/A	N/A	N/A
Safety	moderate	moderate	low	high	moderate?	high	high

1 Sublimation from solid source.
2 Varies with wt% TMAH, can be controlled to yield very low roughness.
3 Addition of Xe to vary stoichiometry in F or Br etch systems can yield optically smooth surfaces.
4 Some formulations do not attack Al, but are not common.
5 With added Si, polysilicic acid or pH control.
6 Defined as 1) allowing wafer to be immersed directly with no special measures and 2) no alkali ions.
7 Includes cost of equipment.

2.1.3 *Wafer Bonding*

Wafer bonding technology, developed for manufacture of MEMS devices, has rapidly become an important technology in semiconductor manufacturing today. Wafer bonding has already been widely used in microsystems such as accelerometers, micromirrors and gyroscopes that require a microcavity to protect the device from the environment and to improve the performance, e.g. the significant sensitivity improvement using hermetic packaging of the accelerometers and gyroscopes. Manufacture of infrared (IR) detectors and resonant devices also requires wafer bonding technology for vacuum-sealed packages. The classification of wafer bonding technology is shown in Fig. 2.5 [31, 32]. The choice of bonding methods largely depends on the initial substrate, tolerance to temperature and the final applications. Typically temperature, force and/or an intermediate layer are used to facilitate bonding. Silicon direct, anodic, eutectic and thermocompression bonding are commonly used in fabrication. Silicon direct bonding, also called fusion bonding, applies high temperature and pressure to join two silicon substrates. Companies are now also using plasma processing to activate wafer surface in order to reduce the annealing temperature. Anodic bonding joins a silicon wafer with a glass wafer using a high concentration of alkali metal oxides. With the bonding machines, at elevated temperature, a high-voltage electric field is applied, which dissociates the oxides and drives the metal ions into the glass. Eutectic bonds are used when a hermetic or vacuum seal is required. They use an intermediate bonding material that forms a eutectic alloy at a specific temperature, such as gold-silicon, gold-tin, or lead-silicon. Solder bonding can be classified as hard solder bonding, based on gold alloys (eutectic bonding), or soft solder bonding, based on lead or tin alloys. Lead based soft solders are plastic enough to accommodate thermal expansion but susceptible to metal fatigue after repeated temperature cycles. Adhesive bonding uses photoresists, spin-on glasses or polymers to deposit a planar material between two wafers. Such materials can be annealed at low temperature to provide a low-stress wafer stack. Either the temporal bond or permanent bond could be achieved with the variable bonding conditions. Glass frit bonding uses glass beads suspended in a carrier paste and deposited onto a substrate either in a blanket form or patterned using screen printing, before the application of heat and pressure to make a hermetic seal [33-36].
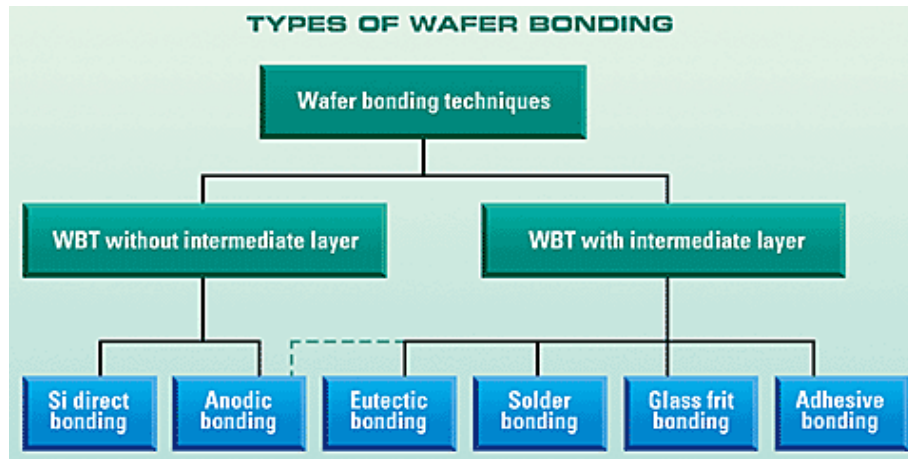
Figure 2.5 Classification of wafer bonding technology [32].

2.1.4 Non-silicon Micromachining

Non-silicon micromachining includes:

- LIGA technology, which is a German acronym for Lithographie, Galvanoformung, and Abformung (Lithography, Electroplating, and Molding) and describes a fabrication technology used to create high-aspect-ratio microstructures;

- laser microengineering, which is used for drilling, cutting, micromachining, annealing, cleaning, lithography, surface structuring, with different kinds of laser systems, such as Nd:YAG, CO_2, and Excimer;

- plasma etching technology, which has been used to pattern the metal, glass, and Lead Zirconate Titanate (PZT), mostly based on the physical bombardment effect;

- ultraviolet (UV) thick photoresist technology, etc., which are based on X-ray and UV photolithograph technologies.

All of these technologies have been used more in the fabrication of non-silicon semiconductor, micro-optical devices and bio-MEMS devices driven by the development of the RF-, optical- and bio-MEMS markets [37].

After several decades of development, MEMS technology has created a huge number of possibilities in a number of areas of research and industry. The main advantages of MEMS technology are: diversified fabrication processes; miniaturised devices; reproducibility and high level integration of multi-functions, which make it a hot research subject and attract the attention of industry. With the progress in microfabrication technology, MEMS moves towards Nano-electro-mechanical systems

(NEMS) technology. MEMS technology still faces many challenges including lack of advanced simulation and modelling tools for design, non-standardized packaging of devices and systems, and lack of quality control for fabrication standards. Future applications of MEMS technology would be driven by processes enabling greater functionality through higher levels of multi-functional electronic-mechanical integration, which would meet the growing markets, e.g. the market of consumer electronics [38-40]. The forecast of the market related to MEMS technology by futurist David Smith of Technology Futures Inc. is shown in Fig. 2.6.

The worldwide market for MEMS ICs will nearly double by 2010 according to internationally known futurist David Smith of Technology Futures Inc. Much of this growth is in mainstream mass-market applications.
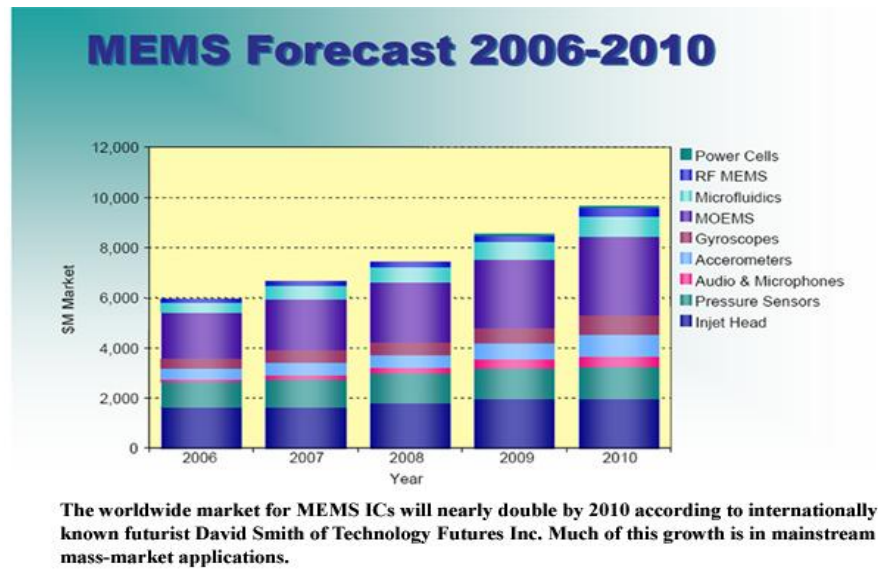
Figure 2.6 Forecast of the market related to MEMS technology.
(Source: Technology Futures Inc.)

2.2   MCM Concept and SiP Technology

2.2.1   MCM Concept

Multi-chip modules (MCMs) allow high-density integration of a number of unpackaged and/or packaged multiple integrated circuits (ICs), semiconductor dies or other modules in such a way as to facilitate their use as a "single IC". The MCM itself will often be referred to as a "chip" in designs, thus illustrating its integrated nature. Multi-chip module packaging is an important facet of modern electronic miniaturisation and micro-electronic systems. An example of an MCM structure is show in Fig. 2.7 [41]. The relationships between architectural components and the corresponding technologies are shown in Table 2.2 [42, 43].
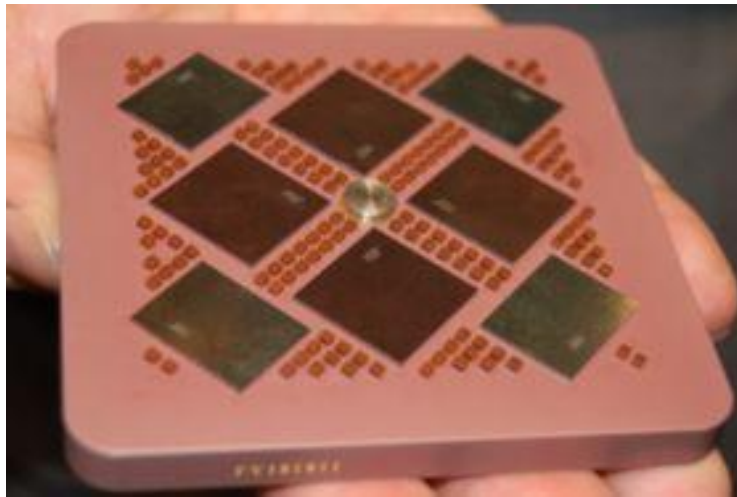
Figure 2.7 Example of MCM with four processors and cache modules [41].

Table 2.2 Relationships between components and technologies of MCM [42, 43].

LEVEL	FUNCTIONS	TECHNOLOGIES
Chips	Digital	Si: CMOS, bipolar
	Analog	GaAs, Complementary GaAs (CGaAs)
	Mixed Analog-Digital	
1st level interconnections	Conductor connection	Peripheral: Wire bond,
	from chips to common	Tape Automated Bonding (TAB), flip TAB
	circuit base	Area: flip chip,
		solder bump, area TAB
Common circuit bases	Signal interconnection	Hybrid circuits
	Power and Ground	MCM-L, MCM-C, MCM-D
	conductors	MCM-D/C
MCM Seals	Hermeticity	Peripheral Conductors
	Heat removal	Dual In-line Package (DIP), Quad Flat Package (QFP)
	Physical protection	Area array conductors:
	conductors	Pin Grid Array (PGA)
2nd level connections	Conductor connection	Plated through-hole vias
	to PWB	surface mount

MCMs are classified according to the technology used to create the high density integration substrate:

- MCM-L, laminated MCM. The substrate is a multi-layer laminated printed circuit board (PCB).

- MCM-D, deposited MCM. The modules are deposited on the base substrate using thin film technology.

- MCM-C, ceramic substrate MCMs, such as low temperature co-fired ceramic (LTCC).

The benefits of this modular approach are cost, high speed, and the portability of a 'plug-and-play' system that can be plugged straight into the motherboard. A key advantage is the elimination of non-value-added packaging and interconnection of bare die, which can add a factor of as much as $100\times$ to the size of the actual functional areas of active and passive components. MCM is thus a commercial technology in achieving smaller and smaller electronic devices [44-46].

2.2.2 System in Package

"System in Package is characterised by any combination of more than one active electronic component of different functionality plus optionally passives and other devices like MEMS or optical components, assembled into a single standard package that provides multiple functions associated with a system or sub-system." said by Robert C. Pfahl [47]. It is an extension of the multi-chip module (MCM) concept to respond to demands for higher levels of integration and functionality including RF and non-electrical functions. To achieve this, SiP supports both the concept of chip stacking (3D integration) and uses substrates that include passives, electrical and non-electrical interconnects and in the future active devices. To date, silicon is the leading technology but other materials such as ceramics, especially Low Temperature Co-Fired Ceramics (LTCC) are gaining interest, especially for harsh environments, RF and high-frequency applications, because of its characteristics of multi-layer process and ceramics reliability. SiP provides more integration flexibility, faster time to market, lower research and development cost, and lower product cost.

Consistent challenge in SiP manufacturing lies in the assembly process itself. Regarded as the next-level MCM assembly technology, it requires the ability to assemble and

interconnect several dies not only horizontally (where die are placed side by side), but also vertical (where several die are placed on top of each other). Mounting die on top of each other and interconnecting them is known as die stacking, a new technology that is harnessed extensively in state-of-the-art SiP manufacturing. This extensive use of stacked die configurations is the reason why SiP is also known as 3-D packaging. The three key approaches to SiP building are die stacking, package stacking and module stacking, which are shown in Fig. 2.8 [1, 48-50].
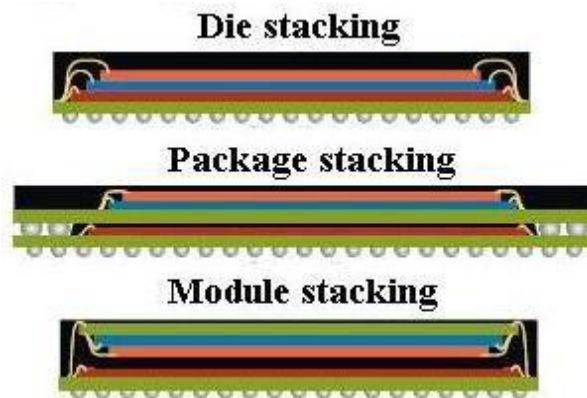
Figure 2.8 The key approaches to SiP technology [50].

The SiP design allows manufacturers to bring together many packages assemblies and IC test technologies to create highly integrated products with optimised cost, size, and performance. Recently, much progress has been made using SiP technology to reduce cost, improve time-to-market, reduce form factor, and reduce power requirement. The overall SiP markets for 2003 and 2007 are shown in Fig. 2.9 [51, 52].
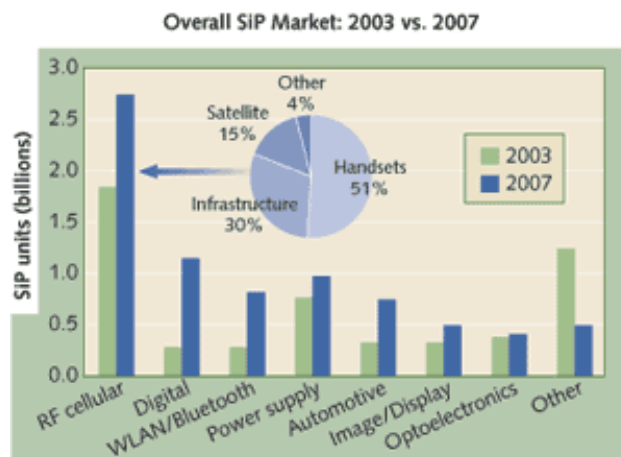
Figure 2.9 Overall SiP Market: 2003 vs 2007 [52].

2.3   System Health Monitoring and Typical Sensors

Advanced sensors and monitoring technologies are playing important roles in prioritising the repair and rehabilitation process and improving the cost-effectiveness of inspection and maintenance of electronic systems. Embedded Microsystems health monitoring has been used in civil infrastructure systems, such as bridges, highways, buildings, pipelines, and many mechanical structures, including aerospace vehicles or heavy mining equipment. The failure of these can cause large economic loss, and even the loss of lives. In using an array of sensors to continuously monitor such structures, embeddable microsystems health monitoring sensors can provide an early indication of problems such as damage to the structure from fatigue, corrosion or impact, and this information can be used to undertake corrective action before the damage develops to a stage where catastrophic failures occur [53-58].

With the widely used Microsystems and the development of integration technologies such as MCM and SiP, the requirements of monitoring the key parameters and reliabilities of functional Microsystems are becoming more and more important. Also the self monitoring and self repairing of the sensors and functional Microsystems also increase their sensitivities and reliabilities, e.g. the temperature and humidity monitoring and feedback correction of piezoresistive devices e.g. the piezoresistive accelerometers. The embeddable health monitoring sensors could also be used for real-time online monitoring and testing of assembly and packaging processes, such as stress monitoring in flip chip and wire bonding, and temperature monitoring for laser assisted packaging [59-64].

Intelligent process monitoring (IPM) methods are also important for process control for yield improvement and cycle time reduction in manufacturing processes [65, 66]. Several methods have been developed for monitoring and control of key processes in the semiconductor and electronic manufacturing industries. A mass spectrometric technique has been developed for monitoring of chemical vapour deposition (CVD) process for producing copper layers [67]. Accelerometers have been used as means to monitor chemical mechanical polishing (CMP) processes [68]. In electronic manufacturing, self-sensing piezoelectric transducers have been applied to the monitoring of wire bonding processes [69]. Temperature sensors have been used for monitoring of ultrasonic chemical and wire bonding processes [70, 71], while recently a

photovoltaic-reflectometer has been developed for process monitoring and control of silicon solar cell manufacture in the rapidly developing photovoltaic industry [72].

Temperature and humidity are two of the most important parameters for the reliability of the sensors and Microsystems. With the environmental test chambers, the temperature, humidity, thermal shock, and rapid temp change stress test are commonly used for investigating the reliability of the sensors and Microsystems. The pressure/stress is also an important parameter for the system reliability, especially for the Microsystems applied to a harsh environment and under dynamic execution.

2.3.1   Temperature Sensor

Temperature is a physical property of a system that underlies the common notions of hot and cold, which is one of the principal parameters of thermodynamics, defined as simply the average energy of microscopic motions of a single particle in the system per degree of freedom. Temperature plays an important role in almost all fields of science including physics, chemistry and biology. Many physical properties of materials, including the phase (solid, liquid, gaseous or plasma), density, solubility, vapour pressure and electrical conductivity, and many principles of sensing effects depend on the temperature, so temperature monitoring is important in many processes and systems as excessive temperature change can result in detrimental effects and failure of operation [73].

Temperature measurement using modern scientific thermometers and temperature scales goes back at least as far as the early 18th century, when Gabriel Fahrenheit adapted a thermometer (switching to mercury) and a scale both developed by Ole Christensen Rømer. Fahrenheit's scale is still in use, alongside the Celsius scale and the Kelvin scale [74]. Temperature sensors based on MEMS technology can be categorized as thermocouples, resistance temperature detectors (RTDs), infrared measurement devices, and fibre-optic measurement system [75, 76].

2.3.1.1 Thermocouples

Thermocouples are among the easiest temperature sensors to use and obtain and are widely used in science and industry, because they are inexpensive, rugged, reliable, and could be used over a wide temperature range ($-250^{o}C \sim 3000^{o}C$) [76, 77]. Thermocouple

temperature monitor is based on the Seebeck effect. A junction, formed from two dissimilar metals, causes a voltage to be developed when a temperature difference appears. A Simple structure of thermocouple is shown in Fig. 2.10, which consists of a sensing junction, at temperature T_a, and a reference junction, at temperature T_b. The voltage developed by the thermocouple is measured with a high resistance voltmeter.
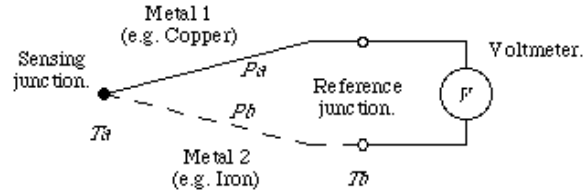

Figure 2.10 Simple structure of thermocouple [76, 77]

The open circuit voltage is related to the temperature difference ($T_a - T_b$), and the difference in the Seebeck coefficients of the two materials ($P_a - P_b$):

$$V = (P_a - P_b)(T_a - T_b) \qquad (2.1)$$

V will typically be of the order of millivolts, or tens of millivolts. Semiconductor materials often exhibit a better thermoelectric effect than metals. It is also possible to integrate many semiconductor thermocouples in series, to make a thermopile, which has a larger output voltage than a single thermocouple on its own [78-81].

2.3.1.2 Resistance Temperature Detectors (RTDs)

Resistance temperature detectors (RTDs) or thermistors, a contraction of "thermal" and "resistor" named by Bell Telephone Laboratories [82], are wire wound and thin film devices that measure temperature because of the physical principle of the positive temperature coefficient of resistance (TCR) of metals. The hotter they become, the higher the value of their electrical resistance. The advantages of RTDs include good long term stability, ease of recalibration, accurate readings over relatively narrow temperature spans and easy for fabrication and integration. But they have a smaller overall temperature range (-200°C~1000°C), higher initial cost and are less rugged in high vibration environments compared to the thermocouples [83]. Above -200°C, the resistivity varies almost linearly with the change of temperature. In this approximately

linear region, the variation of resistivity (R) with temperature (T) can be adequately described by a quadratic equation:

$$R(T) = R_0 \left[1 + \alpha \cdot (T - T_0) \right] \qquad (2.2)$$

where R_0 is the resistivity of the material at a reference temperature (T_0), and α is constant specific to the metal being used [79]. The change of RTDs' electrical resistivity due to a corresponding temperature change has no relationship whether the RTDs' body temperature is changed as a result of conduction or radiation from environment or "self-heating" caused by power dissipation from the device [84, 85]. The resistivity and temperature coefficient of common metals are shown in Table 2.3 [86-89].

Table 2.3 The resistivity and temperature coefficient of common metals [86-89].

Material	Resistivity, $\rho(10^{-8}$ohm m at $20^oC)$	Temperature Coefficient of Resistivity (TCR), $\alpha(10^{-4}/^oC)$
Aluminium	2.65	42.9
Cobalt	6.64	60.4
Copper	1.67	39.0
Gold	2.44	34.0
Indium	9.00	47.0
Iridium	5.3	39.2
Iron	9.71	65.1
Nickel	6.84	68.1
Palladium	10.8	37.7
Platinum	10.6	39.2
Rhodium	4.70	45.7
silver	1.59	38.0
Tungsten	5.60	45.0
Zinc	5.196	41.9

Platinum is often used in RTDs as its resistance variation is particularly linear with temperature. The characteristics of the platinum RTD are shown in Fig. 2.11 [90]. All RTDs used in precise temperature measurements are made of platinum because its TCR is nearly linear, which makes the temperature measurements with precision of ±0.1 ℃ readily achievable. The American Society for Testing and Materials (ASTM) Specification E1137 "Standards Specification for Industrial Platinum Resistance Thermometers" gives many details and specifications over the range from -200 ℃ to 650 ℃, which defines two RTD grades, A and B with a resistance-temperature relationship that has the following tolerances:

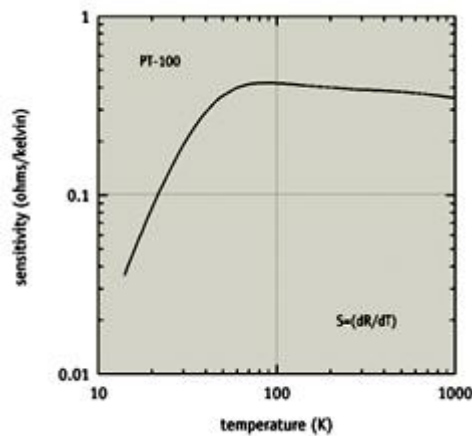$$Grade\ A\ tolerance\ =\ ±[0.13\ +0.0017|t|]\ ℃ \tag{2.3}$$
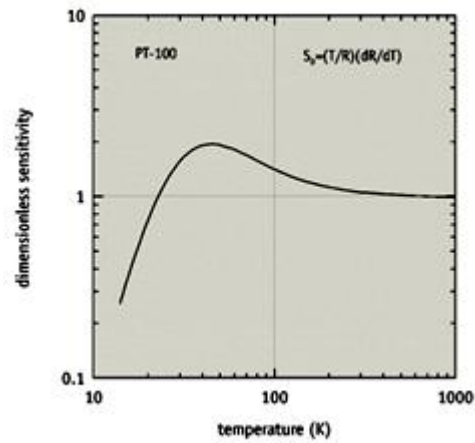
$$Grade\ B\ tolerance\ =\ ±[0.25\ +0.0042|t|]\ ℃ \tag{2.4}$$

where |t| is the absolute value of the RTD's temperature in ℃ [83].
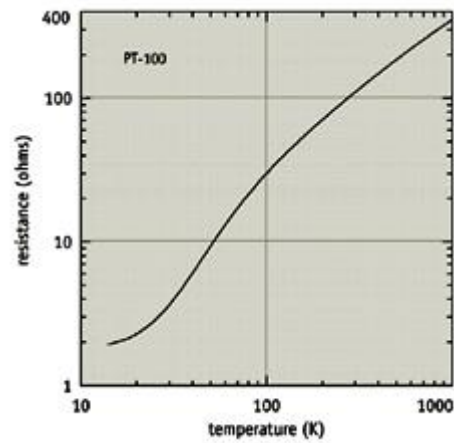
(a)

(b)

(c)

Figure 2.11 The characteristics of platinum RTD [90]

(a) Typical Platinum Resistance Values;

(b) Typical Platinum Sensitivity Values;

(c) Typical Platinum Dimensionless Sensitivity Values.

RTDs can also be made cheaply in copper, nickel and other materials, but there are wire oxidation problems in the case of copper, and restricted ranges because of the non-linear TCR of nickel.

2.3.1.3 Infrared (IR) Measurement Devices

Infrared measurement devices are kinds of non-contact thermometers, which measure temperature using blackbody radiation (generally infrared) emitted from objects. The basic design usually consists of a lens to focus the infrared energy on to a detector, which converts the energy to an electrical signal that can be displayed in units of temperature after being compensated for ambient temperature variation. The infrared thermometer is useful for measuring temperature under circumstances where thermocouples or other probe type sensors cannot be used or do not produce accurate data for a variety of reasons. Some typical circumstances are where the object to be measured is moving; where the object is surrounded by an electromagnetic field, as in induction heating; where the object is contained in a vacuum or other controlled atmosphere; or in applications where a fast response is required [91].
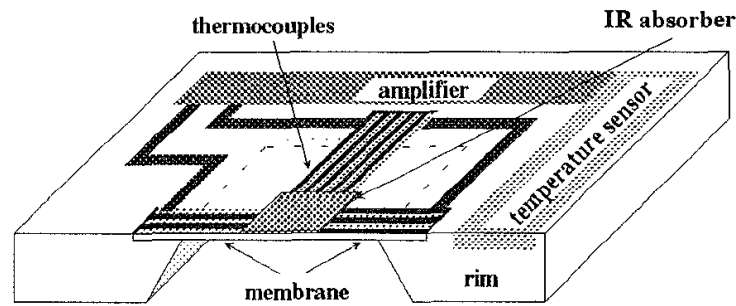
Figure 2.12 Principle of the IR sensor system [92].

Infrared thermometers can be used to serve a wide variety of temperature monitoring functions. There are many varieties of infrared temperature sensing devices available today, including configurations designed for flexible and portable handheld use, as well as many designed for mounting in a fixed position to serve a dedicated purpose for long periods. A principle of the IR sensor system is shown in Fig. 2.12 [92], which is used, for instance, in contactless temperature measurements, IR gas analysis and for passive intrusion alarm sensors. Incoming IR radiation is converted into heat by an IR absorber. The resulting temperature difference between the absorber area and the membrane rim acting as heat sink is measured by thermocouples connected in series. With different materials, some test results of typical IR thermocouples are shown in Table 2.4 [92-94].

Table 2.4 Test results of IR thermocouples [92].

thermocouple	p-Si / n-Poly-Si	p-Si / Al	n-Si / Al
responsivity [V/W]	209	121	59
resistance [kOhms]	518	351	117
time constant [ms]	25	23	25
D^* [cm · $Hz^{1/2}$/W]	$1.3 \cdot 10^8$	$9.5 \cdot 10^7$	$8.0 \cdot 10^7$

2.3.1.4 Fibre-optic Measurement System

An optical fibre is a glass or plastic fibre designed to guide light along its length. Optical fibres are widely used in optical communication, which permits transmission over longer distances and at higher data rates than metal wires, because signals propagate along optical fibres with low loss and immunity to electromagnetic

interference. Optical fibres also have huge applications in sensors areas, and in a variety of other applications such as in bio-medical research [95].

There are several characteristics of optical fibres that allow them to be used for sensors. These include micro-bending, interferometric effects, refractive index change, polarization change, fibre length change, fibre diffraction grating effects, and the Sagnac effect. For temperature measurement, fibre-optic sensors can be classified as:

1. Radiation fibre-optic temperature sensor, which is based on blackbody radiation absorption of the fibre core layer within the fibre itself as a temperature blackbody cavity [96].

2. Raman based fibre-optic temperature sensor, which is based on the Raman nonlinear scattering effect caused by the interaction of fibre materials. The wavelength of Stokes scattering and anti-Stokes scattering are different from the two light transferring directions in the fibre, and the ratio of their intensities is a function of thermodynamic temperature. At 17m/3K (spatial/temperature) resolution, a total sensing range of 37 km was obtained using conventional single-mode transmission fibres and low-power laser diode [97].

3. Fluorescence fibre-optic temperature sensor, which is based on the temperature dependence of the fluorescence intensity or decay rate of fluorescence intensity [98].

4. MEMS based fibre-optic temperature sensors, which are fabricated with many microstructures such as side-polished fibres [99, 100], polarization-maintaining optical fibres [101], fibre bragg gratings structures [102-104], photonic crystal fibres [105], micro Fabry–Pérot resonator [106].

Fibre optic temperature measurement technologies are the new technologies. With decades of development, it is now reaching commercial application gradually and have shown advantages in applications in strong electromagnetic fields; high-voltage electrical facilities; the manufacture process of combustible products; and high temperature measurements.

2.3.1.5 P-N junction temperature sensors

A P-N junction device is usually made of a crystal of semiconductor, such as silicon. The P-N junction is created at the boundary within the crystal between two regions, while one region contains positive charge carriers (holes) as the p-type semiconductor,

25

and the other contains negative charge carriers (electrons) as the n-type semiconductor. A P-N junction can be used as a simple temperature sensor. According to the diode equation [107, 108]

$$I_D = I_s (e^{\frac{qV}{NkT}} - 1)$$

(2.5)

where,

I_D ... diode current

Is ... saturation current

e .... Euler's constant (2.71828...)

q .... charge of electron (1.6×10-19 As)

V .... voltage across the diode

N .... "non-ideality" coefficient (typically between 1 and 2)

k .... Boltzmann's constant (1.38×10-23)

T .... junction temperature in Kelvin

the current through the junction depends on the voltage applied and its temperature. The diode law gives the I–V characteristic of an ideal P-N junction in either forward bias, reverse bias, or no bias), which is derived with the assumption that the only processes giving rise to the current in the junction are drift (due to electrical field), diffusion, and thermal recombination-generation. It also assumes that the recombination-generation current in the depletion region is insignificant. A P-N junction can be used as a temperature sensor, since the forward voltage affects by the temperature change. Assuming a constant current of 10 mA and "non-ideality" coefficient N=1 are applied to a silicon based P-N junction device, the calculation result shows that the voltage across a forward biased junction decreases by a temperature coefficient of about 2 mV/K at room temperature [107, 108].

The linearity response of the P-N junction device is quite limited. Better transducer linearity could be achieved using two different currents across the two junctions as a measure of temperature. Thus, the two P-N junctions are assumed to be identical and should be maintained at the same temperature. These conditions are difficult to achieve theoretically, although each device may get very close matching using integrated circuit

technology [109, 110]. To achieve a P-N junction temperature sensor operated at high temperatures (above 250 °C) is possible, while a low leakage Silicon on Insulator (SOI) based P-N junction is required. It was also reported that performance of the devices would deteriorate beyond these high temperature levels, due to a rapid increase in the diode saturation current [111]. One of the best ways to enhance the sensitivity of p-n junction temperature sensors is to improve the carrier lifetime. By diffusing gold, platinum or cobalt atoms deeper to the junctions, carrier lifetime can be improved while reducing series resistance. The sensitivity is improved because of the dominance of the diffusion current in the leakage current, while reducing the generation current could be achieved by increasing carrier lifetime [112].

2.3.2 *Humidity Sensor*

Humidity is the amount of water vapor in a sample of air compared to the maximum amount of water vapor the air can hold at any specific temperature. Absolute humidity, relative humidity and specific humidity are different ways to express the water content in a parcel of air [113]. Relative humidity (RH) is most frequently used, which is defined as the ratio of the partial pressure of water vapor in a gaseous mixture of air and water vapor to the saturated vapor pressure of water at a given temperature. Relative humidity is expressed as a percentage and calculated in the following manner:

$$RH = \frac{P_{(H_2O)}}{P_{(H_2O)}^*} \times 100\% \tag{2.6}$$

Where $P_{(H_2O)}$ is the partial pressure of water vapor in the gas mixture; $P_{(H_2O)}^*$ is the saturation vapor pressure of water at the temperature of the gas mixture; and RH is the relative humidity of the gas mixture being considered [114].

Humidity sensors can be classified as types of moisture absorption and non-moisture absorption. The veracity of the sensor should reach ±2% ~ ±5% RH, which would usually be measured at $20\,^oC \pm 10\,^oC$ in the clean air. But there are oil, dust and other gases in the air, which will decrease the long term stability of the sensor. The temperature sensitivity usually is 0.2~0.8% RH/^oC and the sensors usually have a different temperature sensitivity based on the different RH [115]. There are four kinds of moisture absorption sensors with the different sensing materials [115-117]:

1. Based on dielectric materials, such as lithium chloride. This kind of sensor has a small hysteresis effect and would not be affected by the speed of wind of the environment, but the sensitivity would reduce after repeated absorption and desorption in long term and high relative humidity will make the materials deliquescent.

2. Based on polymer materials, such as polyimide, fluoropolyol (FPOL), polyvinyl-alcohol (PVA), and benzocyclobutene (BCB). This kind of sensor has a small hysteresis and short response time, but cannot be used in the environment either with organic menstruum or at high temperature.

3. Based on metal oxide films, such as Al_2O_3, Fe_3O_4, and tantalum oxides. This kind of sensor has the advantages of a short response time in the low relative humidity range, small hysteresis and low cost of fabrication.

4. Based on metal oxide ceramics, such as $MgCr_2O_4$-TiO_2 ceramic. This type of sensor has good long term stability and could be effective in the temperature range of $0\sim160^oC$, but oil and dust in the air can contaminate the sensor.

The non-moisture absorption sensors include [115-117]:

1. Sensors based on the thermistor effect which have good reliability and stability. However, these sensors would not be accurate if the air pressure changed, and the oil and dust of the air can contaminate the sensor in the long term.

2. Sensors based on the absorption of infrared rays with 1370 nm and 1250 nm wavelengths which are absorbed by the water vapour.

3. Other kinds of non-moisture absorption sensors, such as optical devices.

Using polymer moisture absorbing layers, capacitance humidity sensors are currently a hot research topic because of the high sensitivity and easy integration. The operating characteristics of a typical sensor, SH1100 of Humirel (the humidity sensor business unit of Measurement Specialties) are shown in Table 2.5 [117].

Table 2.5 Characteristics of the SH1100 (Humirel) humidity sensor [117].

Effective range	（1%～99%）RH
Capacitance at 55%RH	180pF
Capacitance in 0～100%RH	163pF～202pF
Temperature sensitivity	0.04pF/^{o}C
Response time	5s
Hysteresis	1.5%

Polyimide has been used for capacitive humidity sensors based on MEMS and micro-fabrication technologies because of its high moisture absorption and easy fabrication and integration. A typical polyimide-based sensor is shown in Fig. 2.13, with the sensitivity 0.86 pF/%RH (120 nm polyimide) and 3.4pF/%RH (30 nm polyimide). Measurements show an offset drift of less than 1% RH at 50% RH and 37°C, and a hysteresis of ~ 2% RH over a range of 30-70% RH for a 120 nm thick polyimide film sensor [118].
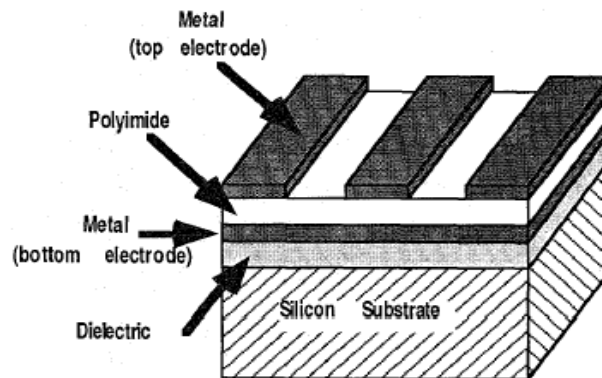

Figure 2.13 A typical polyimide-based capacitive humidity sensor [118].

A heater has also been integrated with the polyimide-based humidity sensor to shorten the response time as a thermal reset. A high-sensitivity polyimide-based humidity sensor is shown in Fig. 2.14, integrated on a polysilicon heater with response time of 1.0 second and a sensitivity of 30.0 fF/%RH. The polyimide sensor has been used to measure relative humidity levels of up to 80% RH. An accuracy of 3% RH has been

obtained using this method, with measurement errors of $0.5^{\circ}C$ and 2% RH in temperature and relative humidity, respectively [119].
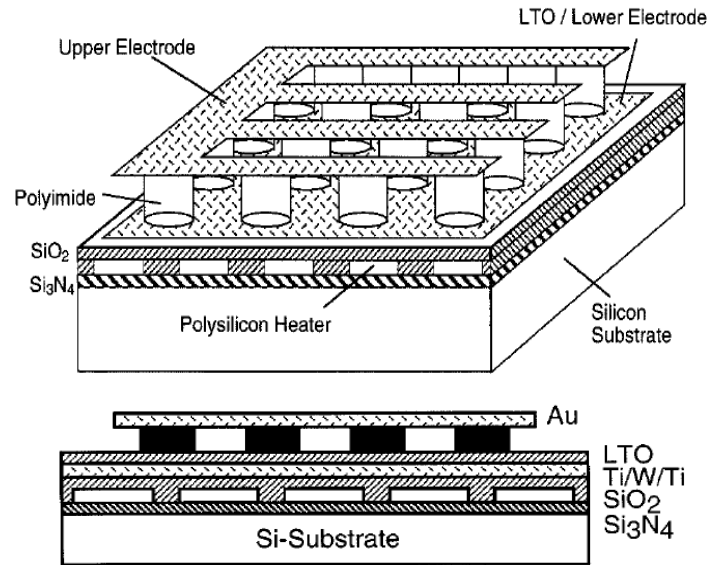

Figure 2.14 A polyimide-based humidity sensor integrated on a polysilicon heater [119].

A new material, called divinyl siloxane benzocyclobutene (DVS-BCB or Photo-BCB), has been used to produce a humidity sensor because of the improvement of sensitivity and response time. A typical sensor with Photo-BCB as the sensitive material is shown in Fig. 2.15, in which the sensitivity was increased to 0.19 pF/%RH, and the response time was decreased to 0.275 second with the sensitive film in thickness of 3.5 μm. In particular, the performance of the device shows that the sensitivity is better under high humidity, which is even more relevant for medical applications. The performance of the sensor could be further enhanced by decreasing the thickness of the film. For a 1.5 μm thick film instead of 3.5 μm, simulation with a dedicated model predicts a sensitivity of 0.39 pF/%RH and a response time of 62 ms [120-122].
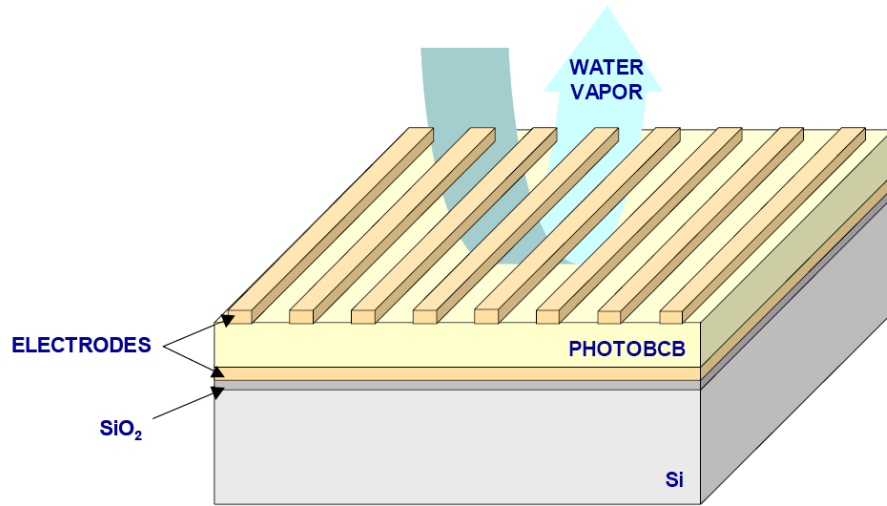
Figure 2.15 A humidity sensor with PhotoBCB material [120-122].

2.3.3   Pressure/Stress Sensor

Pressure is the force per unit area applied on a surface in a direction perpendicular to that surface. Stress is also force/area which is applied in different ways without translation or rotation of the material sample. Stress includes tensile stress which is the stress state leading to expansion, compressive stress which is the stress applied to materials resulting in their compaction (decrease of volume), and shear stress which is a stress state where the stress is parallel or tangential to a surface or interface of the materials [123-125].

The development of measurement of pressure/stress based on micro-fabrication technologies began with the discovery of the metal strain gauge. The pressure/stress sensors could be classified as:

1. strain gauge force sensors;
2. pressure/stress sensors based on piezoresistive effects of materials such as polysilicon and doped silicon;
3. pressure/stress sensors based on capacity tune detection;
4. pressure/stress sensors based on piezoelectric materials;
5. pressure/stress sensors based on surface acoustic wave (SAW) devices;
6. pressure/stress sensors based on optical detection.

The former three kinds of sensors are easier for integration with other sensors to build up a multi sensor system.
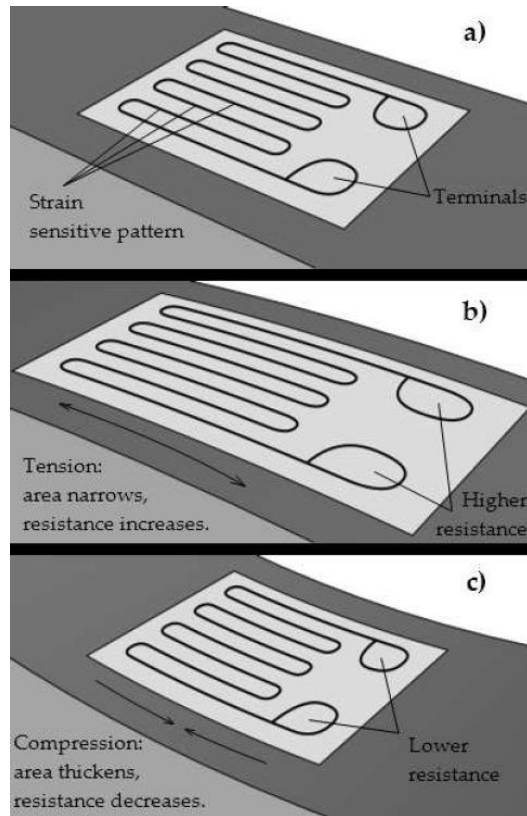
Figure 2.16 Visualization of the working concept behind the strain gauge on a beam under exaggerated bending [126].

2.3.3.1 Strain Gauge Force Sensors

The strain gauge, invented by Edward E. Simmons and Arthur C. Ruge in 1938, is a device used to measure deformation (strain) of an object, which is still used in mechanical transducers. The most common type of strain gauge consists of an insulating flexible backing which supports a metallic foil pattern. The gauge, shown in Fig. 2.16, is attached to the object by a suitable adhesive. As the object is deformed, the foil is deformed, causing its electrical resistance to change. This resistance change is usually measured with a Wheatstone bridge circuit [126].

Consider a metal filament with a circular cross section. The relative change in resistance caused by the force is

$$\frac{\Delta R}{R} = \frac{\Delta l}{l} - \frac{\Delta r}{r} + \frac{\Delta \rho}{\rho} \tag{2.7}$$

where $R = \dfrac{\rho \cdot l}{\pi \cdot r^2}$ is the resistance of the filament, l is the length of the filament, r is the radius of the cross section and ρ is the resistivity of the metal. If the filament is stretched by an external force F, the stress in the filament is $T = \dfrac{F}{\pi \cdot r^2}$ and the strain (the relative elongation) in the filament is $\varepsilon \equiv \dfrac{\Delta l}{l} = \dfrac{T}{E}$, where E is the Young's Modulus of the material.

As well known in mechanics, the longitudinal stretch of a filament is always accompanied with it a lateral contraction, i.e. $\dfrac{\Delta r}{r} = -v \dfrac{\Delta l}{l}$, where v is the Poisson ratio of the material. So

$$\frac{\Delta R}{R} = (1 + 2v)\varepsilon + \frac{\Delta \rho}{\rho} \tag{2.8}$$

The relative change of resistivity, $\dfrac{\Delta \rho}{\rho}$, is a function of stress/strain and is expressed as $\pi T = \pi E \varepsilon$, where π is the piezoresistive coefficient of the material. Therefore, the relative change of resistance is,

$$\frac{\Delta R}{R} = (1 + 2v + \pi E)\varepsilon \equiv G\varepsilon \tag{2.9}$$

where G, the relative change in resistance per unit strain, is referred to as the gauge factor, or G factor of the filament. As π is negligible for metal materials, the gauge factor is just a little larger than unity. Because the maximum strain of the gauge is in the order of 10^{-3}, the relative change of the resistance is also in the order of 10^{-3} [127].

2.3.3.2 Pressure/Stress Sensors Based on Piezoresistive Effect

Single crystal silicon has a face-centred cubic crystal structure, which has anisotropic electrical properties because of the anisotropic structure of the energy band. Ohm's law for anisotropic silicon materials can be expressed as

$$
\begin{bmatrix} E_x \\ E_y \\ E_z \end{bmatrix} = \begin{bmatrix} \rho_1 & \rho_6 & \rho_5 \\ \rho_6 & \rho_2 & \rho_4 \\ \rho_5 & \rho_4 & \rho_3 \end{bmatrix} \begin{bmatrix} J_x \\ J_y \\ J_z \end{bmatrix} \tag{2.10}
$$

where E, ρ and J stand for the intensity of electric field, resistivity and current density respectively. The piezoresistive effect refers to the resistance changes when stress loaded, which could be displayed as following for single crystal silicon:

$$
\begin{bmatrix} \Delta_1 \\ \Delta_2 \\ \Delta_3 \\ \Delta_4 \\ \Delta_5 \\ \Delta_6 \end{bmatrix} = \begin{bmatrix} \pi_{11} & \pi_{12} & \pi_{12} & 0 & 0 & 0 \\ \pi_{12} & \pi_{11} & \pi_{12} & 0 & 0 & 0 \\ \pi_{12} & \pi_{12} & \pi_{11} & 0 & 0 & 0 \\ 0 & 0 & 0 & \pi_{44} & 0 & 0 \\ 0 & 0 & 0 & 0 & \pi_{44} & 0 \\ 0 & 0 & 0 & 0 & 0 & \pi_{44} \end{bmatrix} \begin{bmatrix} T_1 \\ T_2 \\ T_3 \\ T_4 \\ T_5 \\ T_6 \end{bmatrix} \tag{2.11}
$$

where $\Delta = \dfrac{\rho' - \rho}{\rho}$ is the rate of the resistivity change, Π is the piezoresistive coefficient and T is loaded stress. In the 32 symmetric parade, just three independent components are enough for identifying the piezoresistive coefficient which depends on the doping type, doping concentration and temperature. The piezoresistive coefficients of silicon at temperature of 300K are shown in Table 2.6 [128, 129].

Table 2.6 Piezoresistive coefficients of silicon at 300K [128, 129].

Si	π_{11} (10^{-11}/Pa)	π_{12} (10^{-11}/Pa)	π_{44} (10^{-11}/Pa)
P type（7.8Ω.cm）	6.6	-1.1	138.1
N type（11.7Ω.cm）	-102.2	53.4	-13.6

Heavily doped P^+ silicon is usually used for piezoresistive pressure/stress sensors because of the larger piezoresistive coefficient. In addition, silicon sensors can be fabricated using both surface fabrication and common MEMS processes. Both the time

for diffusion and the energy for implantation can be easily controlled. However, the resistivity of the P$^+$ silicon has a significant dependence on temperature, which may affect the sensitivity and the resolution of the sensors.

Polycrystalline silicon (polysilicon) is another kind of piezoresistive material with considerable enhancement when a phosphorus diffusion source is used instead of boron dopants for realising piezoresistors. Polysilicon is used as a piezoresistive material also because of the advantage that the temperature coefficient of resistivity (TCR) can be made zero by suitably adjusting the doping concentration. However, the sensitivity of the polysilicon piezoresistor is always lower compared to the monocrystalline piezoresistor because of the lower gauge factor of polysilicon than that of the monocrystalline silicon [130]. The gauge factors of different materials are shown in Table 2.7 [131].

Table 2.7 Gauge factors of different materials [131].

Material	Gauge Factor
Metal Foil	1 to 5
Thin film metal	~2
Diffused Semiconductor	80-200
Doped Polysilicon	15-27

The membrane based pressure sensor, shown in Fig. 2.17, is usually fabricated with a Wheatstone bridge structure, shown in Fig. 2.18, for increasing the sensitivity of the sensors. The output voltage is related to the change of resistances caused by the pressure/stress with a positive coefficient for the tensile stress and a negative coefficient for the compressible stress [132, 133].
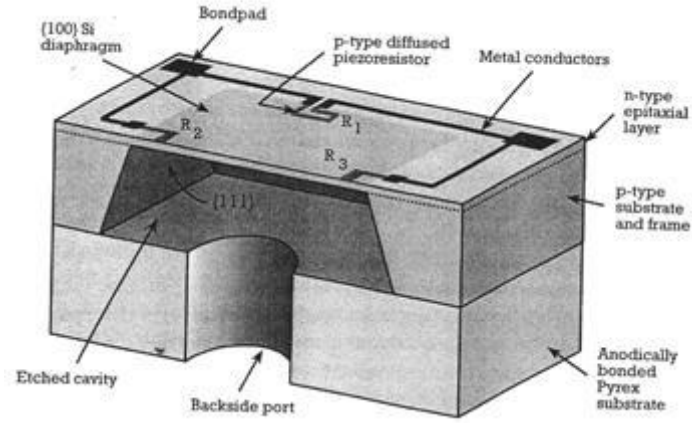
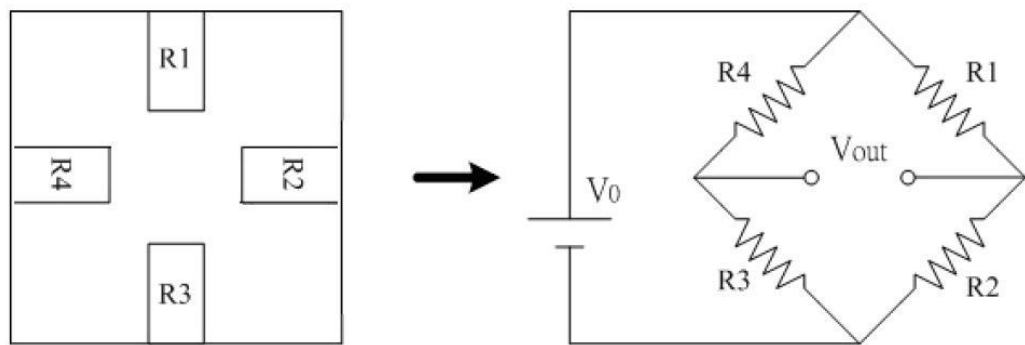Figure 2.17 Structure of membrane pressure sensor [132].

Figure 2.18 Wheatstone bridges for piezoresistive pressure sensor [133].

2.3.3.3 Pressure/Stress Sensors Based on Capacitive Detection

In addition to many successful applications in conventional transducers in industry, capacitive sensing also has many attractive features for MEMS applications. Minimal additional processes are required using most machining technologies for capacitive sensors. Capacitors can operate as both sensors and actuators. Excellent sensitivity has been demonstrated, the transduction mechanism is intrinsically insensitive to temperature, and the sensitivity of the sensor remains constant with the scaled-down geometry of the structure.

The theory governing capacitive sensing is the well-established electrostatics. However, special considerations have to be made for its applications:

- As the capacitance of MEMS capacitors is usually small in value, the effects of stray capacitance and parasitic capacitance are relatively large. Therefore, special attention has to be paid to these effects in the design of the sensing structure and circuitry.

- As micro-mechanical capacitors operate both as sensors and actuators, the electrical excitation signal for capacitance sensing changes the capacitance being measured. The effect interferes with the measurement and reduces the signal that could lead to failure of the capacitance sensors.

The structure of a typical pressure/stress sensor based on capacitance detection is shown in Fig. 2.19, which has a similar "sandwich" structure to the pressure/stress sensors that are based on piezoresistive effect [134].
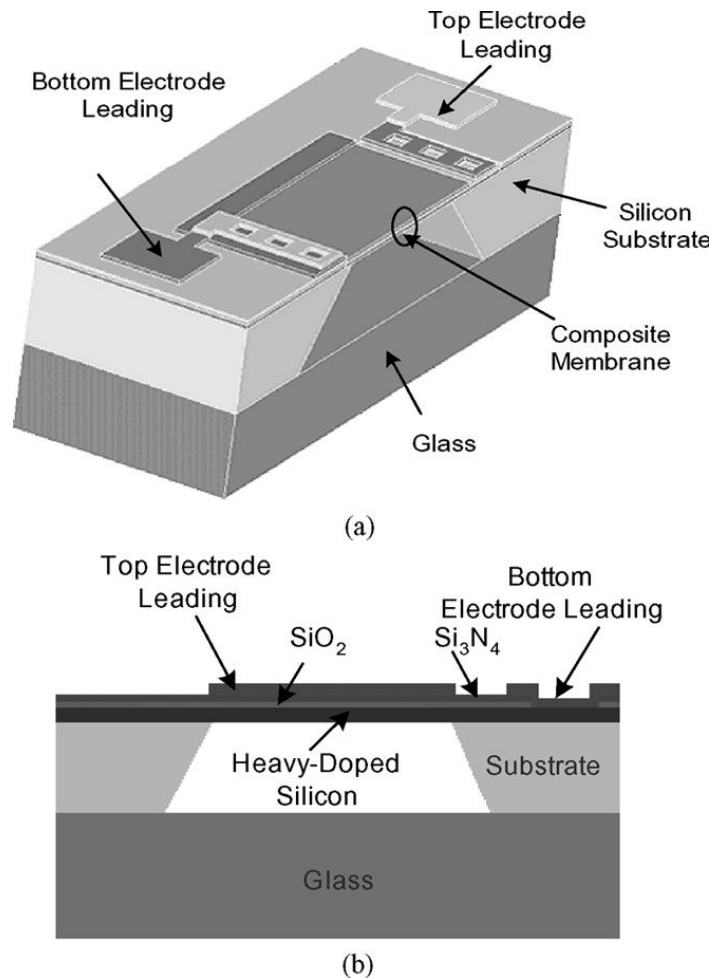

Figure 2.19 Simplified structure of composite-membrane capacitive pressure sensor[134]

(a) Side view of the sensor structure and (b) cross section of the structure.

The relative capacitance change of the flexible parallel-plate solid-state capacitor involves the area change of the electrodes and a change in the thickness and relative dielectric constant of the dielectrics. It can be shown that

$$\frac{\Delta C}{C} = -\frac{\Delta h}{h} + \frac{\Delta A}{A} + \frac{\Delta \varepsilon}{\varepsilon} \qquad (2.12)$$

where h, A and ε are the thickness, area and dielectric constant of the dielectric layer, respectively. The area change of the electrodes, ΔA, is determined by the bending shape of the sandwich structure under uniform pressure load. $\frac{\Delta A}{A}$ and $\frac{\Delta h}{h}$ define the geometry variation of the structure, while $\frac{\Delta \varepsilon}{\varepsilon}$ shows the composite physical effect of the elastic dielectric layers, which extends the conventional principles of the capacitive pressure sensor based on the sandwich structure. A fabricated device with sensitivity of 0.2 pF/kPa was reported [134,135].

2.4 Summary

The MEMS market has grown rapidly with the development of the advanced integration technologies, including MCM, SiP, and SoC. While most of the component technologies required for heterogeneous integration exist, the integration and associated manufacture of these systems places major challenges on test and reliability validation processes. Investigations into the embeddable Microsystems health monitoring solutions is required far prioritising the repair and rehabilitation process, improving the cost-effectiveness of inspection and maintenance, and ultimately enhancing the lifetime and safety of the Microsystems. These Microsystems are used in monitoring the safety of the civil infrastructure systems, such as bridges, highways, buildings, pipelines, and many mechanical structures, including aerospace vehicles or heavy mining equipment.

After a general review of MEMS technology based on the techniques and theories of micro-techniques, system-techniques and materials effects, the concepts of MCM and SiP technologies were summarised. These technologies are the most advanced 3-D packaging technologies with three key approaches including die stacking, package stacking and module stacking. One of the most important application of MCM and SiP is sensors for embedded system health monitoring. Three kinds of sensors, including temperature, humidity and pressure/stress sensors, have been reviewed, which could be used for the integrated microsystem health monitoring, environmental and intelligent process monitoring. Temperature sensors were studied in categorised on thermocouples, resistance temperature detectors (RTDs), infrared measurement devices, fibre-optic

measurement systems and p-n junction temperature sensors. Polymer based humidity sensors were selected as the focus of the relative humidity (RH) detectors. A summary of the pressure/stress sensors has been also carried out based on the different sensing effects, including strain gauge effect, piezoresistive effect, capacity detection, piezoelectric effect and optical detection.

Chapter 3   Design and Fabrication of Thin Film Temperature Sensors

Temperature monitoring is important in many processes and systems as excessive temperature change can result in detrimental effects and catastrophic failure of processes and systems. Effective process monitoring methods have been demonstrated for ultrasonic chemical processes [70] and for wire bonding in electronic manufacturing [71]. Thin film sensors with small foot print are required for embedded system health monitoring application, with sensors or sensor arrays being embedded into packages of SiP based Microsystems. Thin film resistance sensors are ideal for this work, because they are low cost and are easy to fabricate using thin film deposition and wet or dry etching methods. Both platinum and nickel based thin film temperature sensors were studied. Platinum based sensor is mainly used for precise sensing, because it is relatively expensive and has better linearity of temperature coefficient of resistivity. Nickel is a relatively cost effective option but offers nonlinear response at higher temperature. Temperature sensors were studied in range between room temperature (20 ℃) and 375 ℃ for the applications of both the integrated health monitoring in microsystems and the process monitoring in laser assisted bonding, where the temperature above 350 ℃ would be expected.

3.1   Design and Theoretical Calculation

The meander structure of a metal thin film resistance sensor is shown in Fig. 3.1. The sensor was designed for high sensitivity within a small effective area. The total resistance at temperature, T, is given by

$$R(T) = R_0\left[1 + \alpha \cdot (T - T_0)\right] = \rho \cdot \frac{n(L + 0.5w)}{w \cdot h}\left[1 + \alpha \cdot (T - T_0)\right] \qquad (3.1)$$
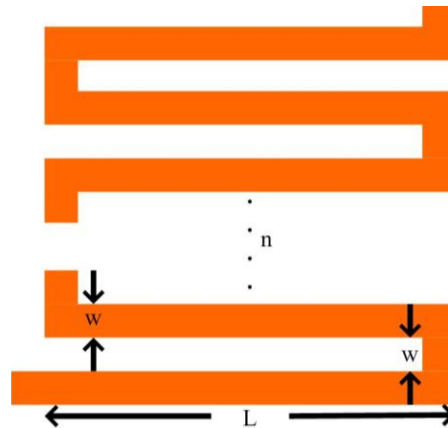

Figure 3.1 Meander structure of thin film resistance temperature sensor.

where R_0 is the resistance of the material at a reference temperature (T_0), ρ is the resistivity of the metal being used, L and w are the dimensions of the meander structure, h is the thickness of the film, and α is the temperature coefficient of resistance (TCR), a constant specific to the metal's physical properties [136, 137].

The physical properties of platinum and nickel are shown in Table 3.1. The resistance of the meander platinum thin film device at 293K for length of $10\,mm$, width of $5\,\mu m$ and thickness of $100\,nm$ is

$$R_0 = \rho \cdot \frac{l}{w \cdot h} = 10.6 \times 10^{-8} \cdot \frac{10^4 \times 10^{-6}}{5 \times 10^{-6} \times 100 \times 10^{-9}} = 2.12 \times 10^3 \, \Omega \qquad (3.2)$$

Then, the temperature dependent response of the resistor is

$$R(T) = R_0 + R_0 \cdot \alpha \cdot (T - 293) = 2.12 \times 10^3 \left[1 + 0.00392 \cdot (T - 293)\right] \qquad (3.3)$$

Fig. 3.2 shows the change of resistance as a function of temperature.

Table 3.1 The physical properties of platinum and nickel.

(Source from Comsol 3.3)

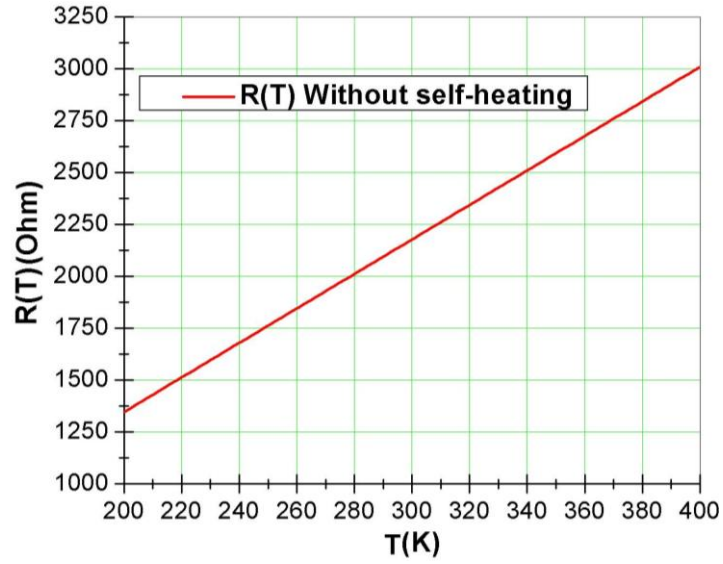|	Platinum	Nickel
Density	$21.45 \times 10^3 \, kg/m^3$	$8.90 \times 10^3 \, kg/m^3$
Young's modulus	$1.68 \times 10^{11} \, Pa$	$2.19 \times 10^{11} \, Pa$
Poission's ratio	0.38	0.31
Resistivity	$10.6 \times 10^{-8} \, \Omega \cdot m$	$6.84 \times 10^{-8} \, \Omega \cdot m$
Heat capacity	$133 \, J/(kg \cdot K)$	$445 \, J/(kg \cdot K)$
Thermal conductivity	$71.6 \, W/(m \cdot K)$	$90.7 \, W/(m \cdot K)$
Thermal expansion coeff.	$8.80 \times 10^{-6}/K$	$13.4 \times 10^{-6}/K$
Temperature resistivity coeff.	$39.2 \times 10^{-4}/K$	$68.1 \times 10^{-4}/K$

Figure 3.2 Calculated response of resistance R(T) as a function of temperature T.

The sensitivity of the temperature sensor under the constant current conditions should be

$$\eta = \frac{U(T_1) - U(T_2)}{T_1 - T_2} = \frac{I_0 \cdot [R(T_1) - R(T_2)]}{T_1 - T_2} = \frac{I_0 \cdot R_0 \cdot \alpha \cdot (T_1 - T_2)}{T_1 - T_2} = \alpha \cdot I_0 \cdot R_0 \qquad (3.4)$$

where

$I_0 = 0.7mA$,

$R_0 = 2120\Omega$,

$\alpha = 0.00392$ (Platinum).

Then the sensitivity is

$$\eta \approx 5.82mV / K.$$

The output voltage is

$$U(T) = I_0 \cdot R(T) = I_0 \cdot R_0 [1 + \alpha \cdot (T - 293)] \qquad (3.5)$$

$$U(T = 300K) = 1.525V.$$

42

Fig. 3.3 shows the dependence of the output voltage on temperature.
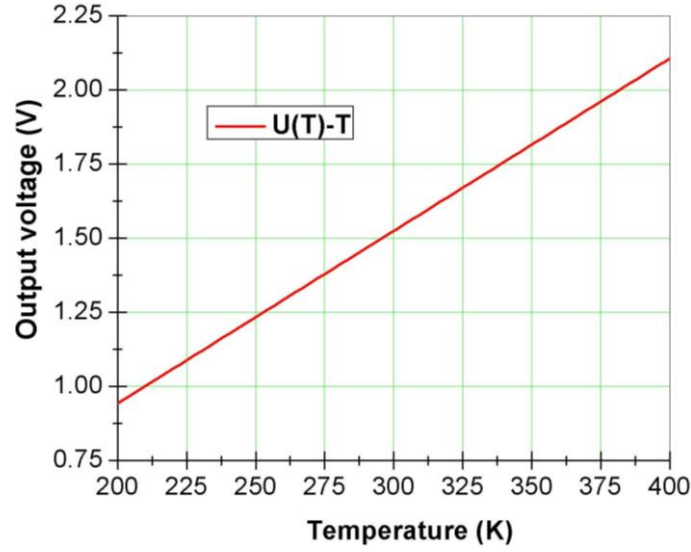

Figure 3.3 Output voltage versus temperature for a constant current of 0.7mA.

Known as the self-heating effect, heat will be generated and raise the temperature of the resistor when a current flows through it, which would make the temperature of the resistor above that of its environment and may introduce an error if a correction is not made. The power of self-heating is

$$P(T) = I_0^2 \cdot R(T) = I_0^2 \cdot R_0 \left[1 + \alpha \cdot (T - 293)\right] \tag{3.6}$$

$$P(T = 300K) = 1.067 mW .$$

The sensitivity under constant voltage conditions should be

$$\eta = \frac{I(T_2) \cdot R_{con} - I(T_1) \cdot R_{con}}{T_1 - T_2} = \frac{\left[\dfrac{U_0}{R_0 \left[1 + \alpha \cdot (T_2 - 293)\right] + R_{con}} - \dfrac{U_0}{R_0 \left[1 + \alpha \cdot (T_1 - 293)\right] + R_{con}}\right] \cdot R_{con}}{T_1 - T_2} \tag{3.7}$$

where R_{con} is a constant resistance for an output signal of voltage shown in Fig. 3.4. Both temperature and R_{con} play important parts in the output sensitivity of the temperature sensor. While $T = 300\ K$ ($T_1 = 300.1\ K$, $T_2 = 299.9\ K$) and $U_0 = 2.1\ V$, the

relationship between η and R_{con} in Fig. 3.5 shows that we can get the best sensitivity when the following condition is satisfied

$$R_{con}(300\text{K}) = R(T = 300\text{K}) = R_0\left[1 + \alpha \cdot (300 - 293)\right] = 2178\Omega$$
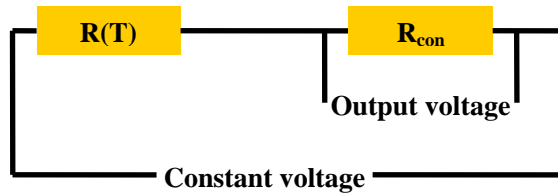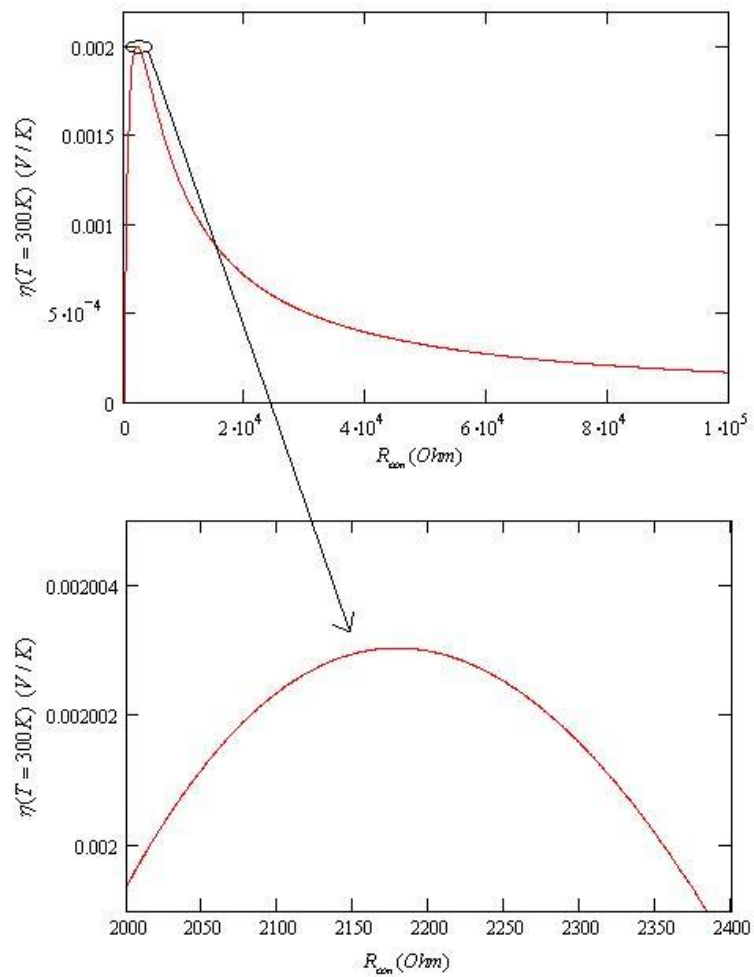

Figure 3.4 Test circuit for constant voltage.

Figure 3.5 Relation between sensitivity and readout resistance.

When

$T = 300K$,

$U_0 = 2.1V$,

$R_{con} = 2178\Omega$,

the sensitivity of the temperature sensor is

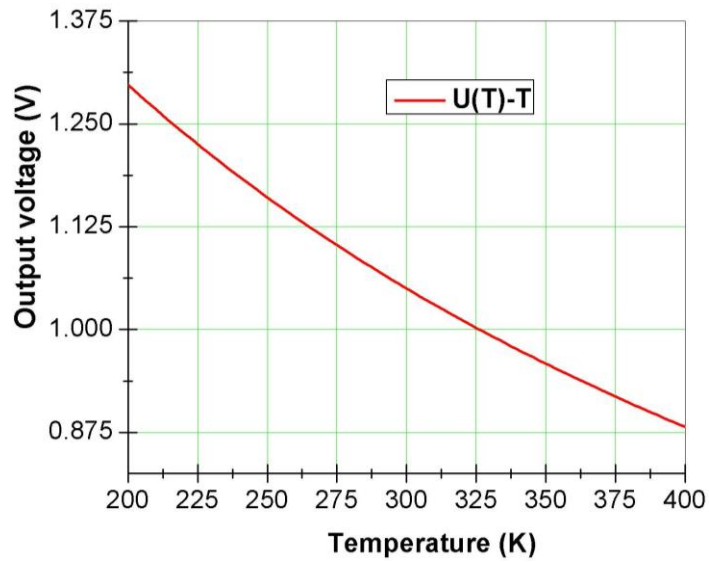$$\eta \approx 2.00mV / K .$$

The output voltage is shown in Fig. 3.6.

Figure 3.6 Output voltages versus temperature with a 2.1 V constant voltage.

The power of self-heating is

$$P(T) = \frac{U_0^2}{R_0\left[1+\alpha \cdot (T-293)\right]+R_{con}} \tag{3.8}$$

$$P(T = 300K) = 1.012mW .$$

According to these theoretical calculations, a larger resistance of the metal thin film would offer higher sensitivity for temperature sensors. The output voltage would be linear for a constant current input but non-linear for a constant voltage input.

3.2 Simulation with Finite Element Method

The finite element method (FEM) is a numerical method for finding approximate solutions of partial differential equations (PDE) and integrals. The method is based either on eliminating the differential equations completely (steady state problems), or rendering the PDE into an equivalent ordinary differential equation, which is then solved using the standard techniques such as finite differences [138].

Making these approximations enables us to solve complex problems with commonly available computational effect (on a PC). ANSYS is a general-purpose finite element analysis software, with self contained analysis tools incorporating pre-processing (geometry creation, meshing), solver and post processing modules in a unified graphical user interface. ANSYS can be used to solve a wide variety of mechanical problems including static/dynamic structural analysis, heat transfer and fluid problems, as well as acoustic and electro-magnetic problems. ANSYS Mechanical incorporates both structural and material non-linearities. ANSYS Multiphysics includes solvers for thermal, structural, Computational fluid dynamics (CFD), electromagnetics, acoustics and can couple these separate physics modules together for multi-disciplinary applications [139].

Simulations based on ANSYS software have been performed to assist the design of the metal thin film temperature sensors. The results of simulations are shown in Fig. 3.7 using a 5V of constant voltage. The dimensions of a single unit of platinum thin film are 100 μm×5 μm ×1 μm. The sensing temperature and the environment temperatures are assumed to be 350K and 293K respectively.

- According to the simulation, the inside corners of the meander devices exhibit the maximum temperature. Here the resistance is lower compared with the outside corners. Rounded corners have the advantage of reducing the temperature gradient but are more difficult to fabricate at the microscale because of the photolithography process for small feature (<5 μm).
- According to Fig. 3.7 (a,b) and (c,e), the average temperatures of 4 units and 12 units of the meander sensor structures are 383.6K and 351.03K, respectively, without air convection, which shows that the self-heating effect is more significant in a sensor with a lower resistance, because the lower resistance resulted in a higher self heating power with the 5V of constant voltage.

- According to Fig. 3.7 (c,e,g) and (d,f,h), the average temperatures of the 12-unit meander sensor with and without air convection condition are the same as 351.03K, which shows that the effect of air convection can be ignored for a sensor with more meanders.

- According to Fig. 3.7 (c,d) (e,f) and (g,h), the average temperatures at 1ms, 1s and 10s after operation are the same, 351.03 K, which shows that the metal thin film temperature sensor has a quick response time.
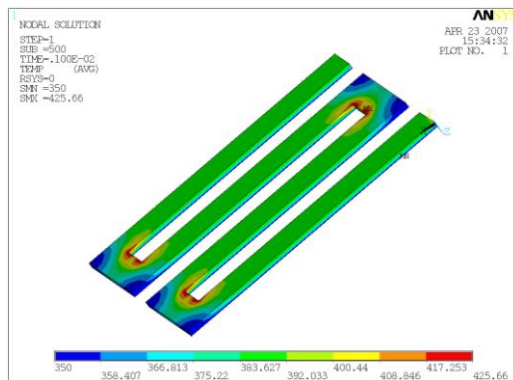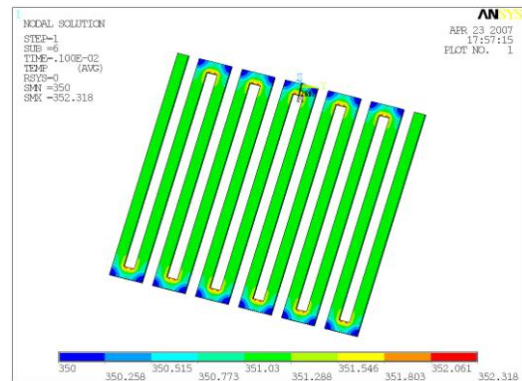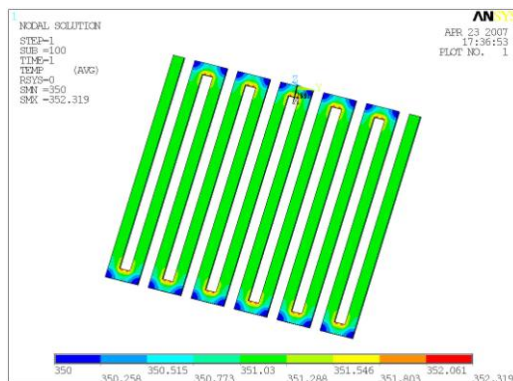

(a)Time=0.001s, without air convection
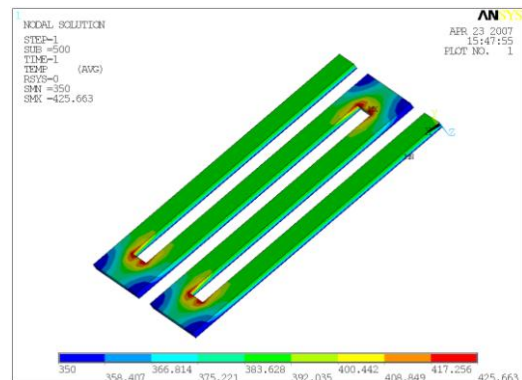
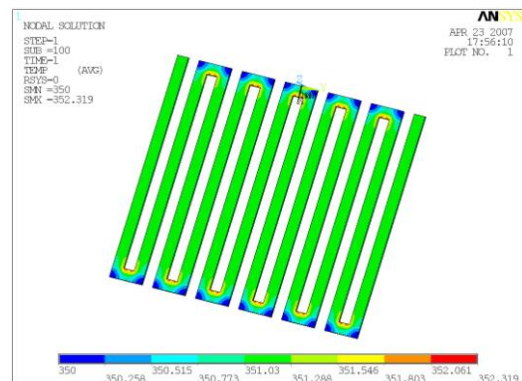(b) Time=1s, without air convection
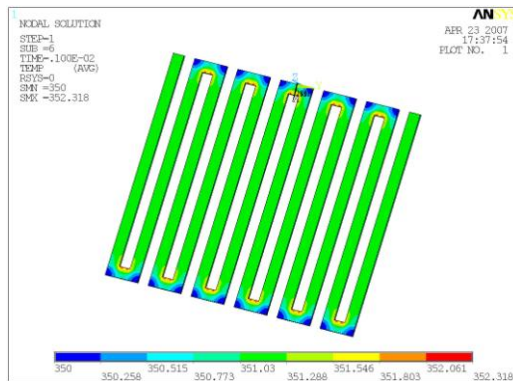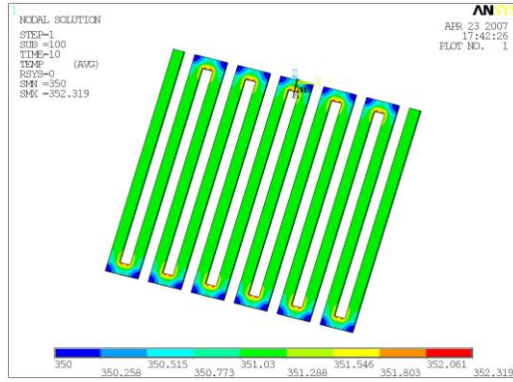

(c) Time=0.001s, without air convection

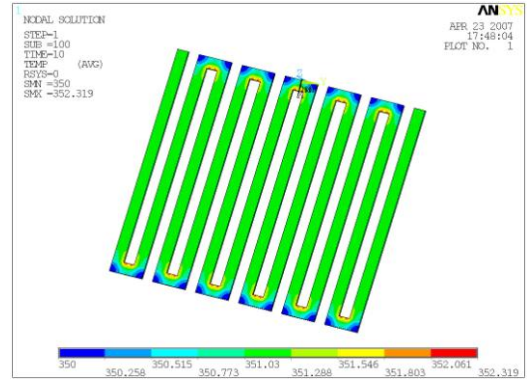(d) Time=0.001s, with air convection

(e) Time=1s, without air convection

(f) Time=1s, with air convection

(g) Time=10s, without air convection   (h) Time=10s, with air convection

Figure 3.7 FEM simulation of temperature sensor based on ANSYS.

(Blue scale represents low temperature and red scale represents high temperature)

According to the results of the FEM simulations, a metal thin film resistor with a resistance of the order of kΩ would be better for both requirements of higher sensitivity and smaller scale. The self-heating effect should be corrected with calibration curves or a differential compensation signal. Based on both guidance from analytical calculations and FEM simulations, the designed dimensions of the meander structures for metal thin film temperature sensor are shown in Table 3.2, which were selected in order to achieve a footprint as small as possible. The sensitivities were calculated based on the 0.7mA of constant current.

Table 3.2 Dimensions design and theoretical sensitivities of temperature sensor

No.	Dimensions of the meander structures	Footprint of single device	Resistance of Ni film (100nm)	Sensitivity of Ni film (0.7mA)	Resistance of Pt film (100nm)	Sensitivity of Pt film (0.7mA)
01	$3\mu m \times 251.5\mu m \times 40$	$250\,\mu m \times 240\,\mu m$	$2294\,\Omega$	$11\,mV/K$	$3555\,\Omega$	$9.8\,mV/K$
02	$5\mu m \times 302.5\mu m \times 34$	$300\,\mu m \times 340\,\mu m$	$1407\,\Omega$	$6.7\,mV/K$	$2180\,\Omega$	$6.0\,mV/K$
03	$7\mu m \times 303.5\mu m \times 34$	$300\,\mu m \times 476\,\mu m$	$1008\,\Omega$	$4.8\,mV/K$	$1563\,\Omega$	$4.3\,mV/K$
04A	$10\mu m \times 305\mu m \times 50$	$300\,\mu m \times 1000\,\mu m$	$1043\,\Omega$	$5.0\,mV/K$	$1617\,\Omega$	$4.4\,mV/K$
04B	$10\mu m \times 700\mu m \times 36$	$700\,\mu m \times 700\,\mu m$	$1736\,\Omega$	$8.3\,mV/K$	$2690\,\Omega$	$7.4\,mV/K$
05	$20\mu m \times 3100\mu m \times 60$	$300\,\mu m \times 2400\,\mu m$	$636\,\Omega$	$3.0\,mV/K$	$986\,\Omega$	$2.7\,mV/K$

48

3.3 Photomask Design and Manufacturing

A 5-inch photomask was designed using the design software L-Edit (Tanner Research, Inc.). L-Edit MEMS Design provides unsurpassed capabilities for the design of MEMS, including all-angle polygon support, complete layer visualization, all-angle design rule check (DRC), robust algorithm for curved objects, high resolution Encapsulated PostScript (EPS) output, and full AutoCAD Drawing eXchange Format (DXF) input/output compatibility. The mask design was manufactured using high quality chrome film based soda lime glass photomask by Delta Mask, Netherlands. The layout of the mask, exported from the L-Edit file, is shown in Fig. 3.8. There are 5 kinds of temperature sensor arrays included in this design, which are shown in Table 3.3. The photographs of the fabricated sensors from the chrome film based soda lime glass photomask, taken using an Olympus SZX10 advanced routine stereo zoom microscope, are shown in Fig. 3.9.
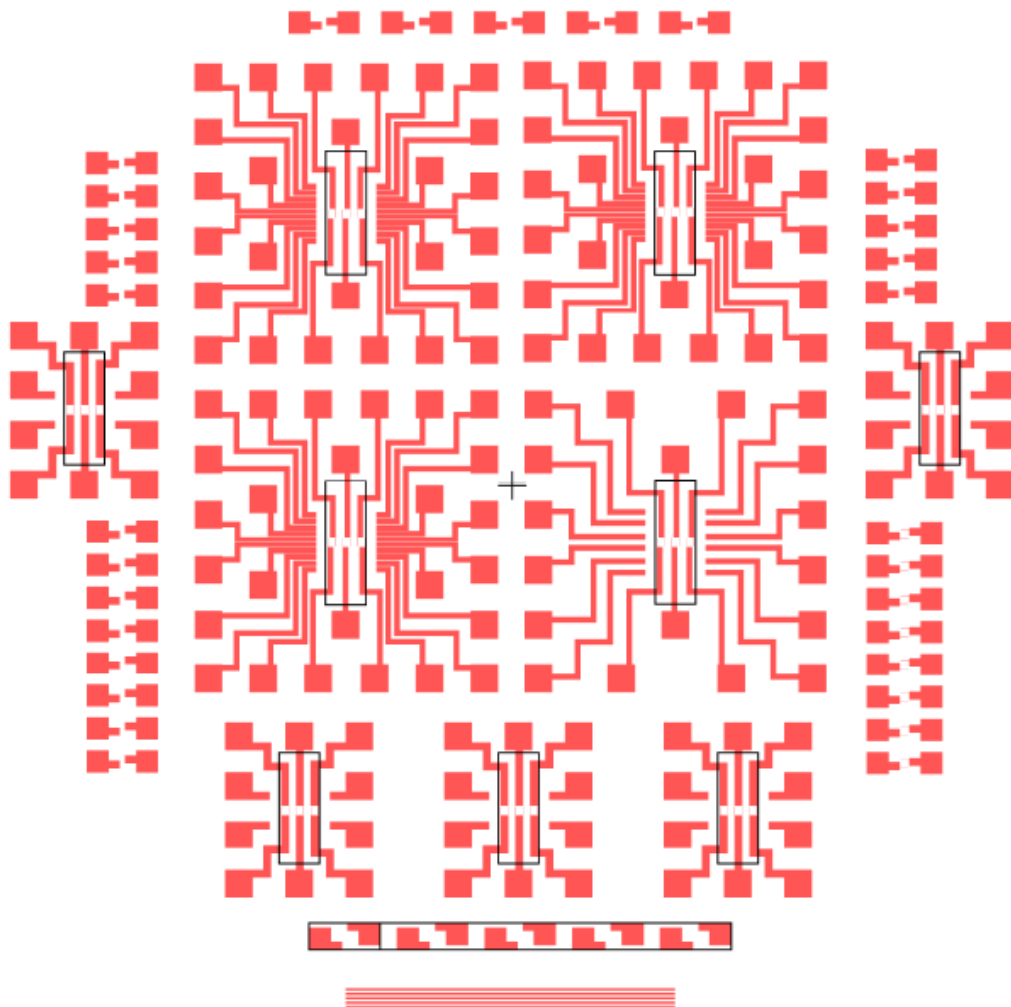

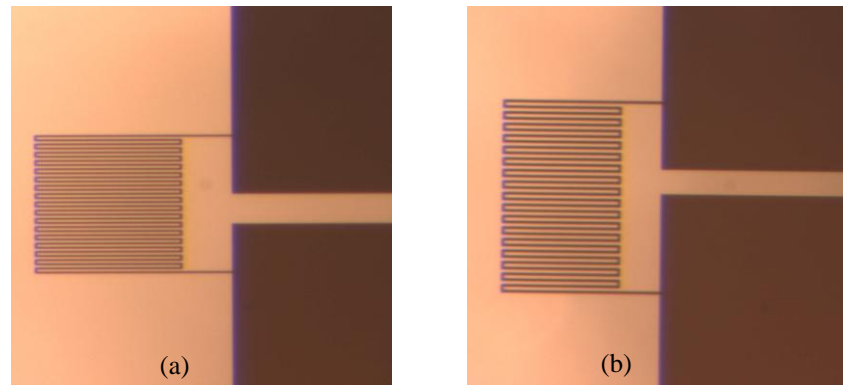Figure 3.8 Layout of the designed photomask from L-Edit file.

Figure 3.9 Photographs of sensor mask

(a) Sensor with track width of 3 μm (b) Sensor with track width of 10 μm.

Table 3.3 Design information of the photomask.

Layout of the photomask			
	Single sensor 01 (5×)		
Single sensor 02 (5×)	Multi-Sensor A	Multi-Sensor B	Single sensor 03 (5×)
Multi-Sensor E	Multi-Sensor C	Multi-Sensor D	Multi-Sensor E
Single sensor 04A (8×)			Single sensor 04B (8×)
	Multi-Sensor E (3×)		
	Single sensor 05 (5×)		
	Alignment for KOH/ RIE Silicon (X-axis)		
Design information of the individual sensors			
Single-Sensor	Length(μm)	Width(μm)	Step for dicing
01	10060	3	8450 μm -X
02	10285	5	3000 μm -Y
03	10319	7	3000 μm -Y

04A	15250	10	3000 μm -Y
04B	25380	10	3000 μm -Y
05	18600	20	8000 μm -X

Design information of the multi-sensor arrays		
Multi-Sensor	Detail of Sensors	Dimension of contact
A	Sensor01 (10×) at border with Sensor04B (3×) central	500 μm width except border central 400 μm
B	Sensor02 (10×) at border with Sensor04B (3×) central	500 μm width except border central 400 μm
C	Sensor03 (10×) at border with Sensor04B (3×) central	500 μm width except border central 400 μm
D	Sensor04A (6×) at border with Sensor04B (3×) central	500 μm width
E	Sensor05 (2×) at border with Sensor04B (3×) central	700 μm width

Design information of the contact pads	
Pads for Single-Sensor	2mm ×2mm
Pads for Multi-Sensor	2.5mm×2.5mm

3.4 Fabrication and Testing of Nickel Based Temperature Sensors

Nickel was used firstly as the thin film material for the temperature sensors because of its low cost and high TCR. The sensors with meander structures were fabricated using the process shown in Fig. 3.10. The nickel thin films were deposited by E-beam evaporation at 50 mA of electron gun current for 80 seconds. The wafers were cleaned with DI water and Decon90 liquid before deposition. After spin coating with a 6.5 μm of AZ9260 photoresist (6000 rpm for 60 seconds) and baking at 80°C for 4 minutes, UV photolithography was carried out using the chrome film based soda lime glass photomask on a mask aligner (Tamarack Model 152R), the exposure dose of which was 370 J/cm^2. The nickel etchant, shown in Table 3.4 for detail, was used for nickel etching.
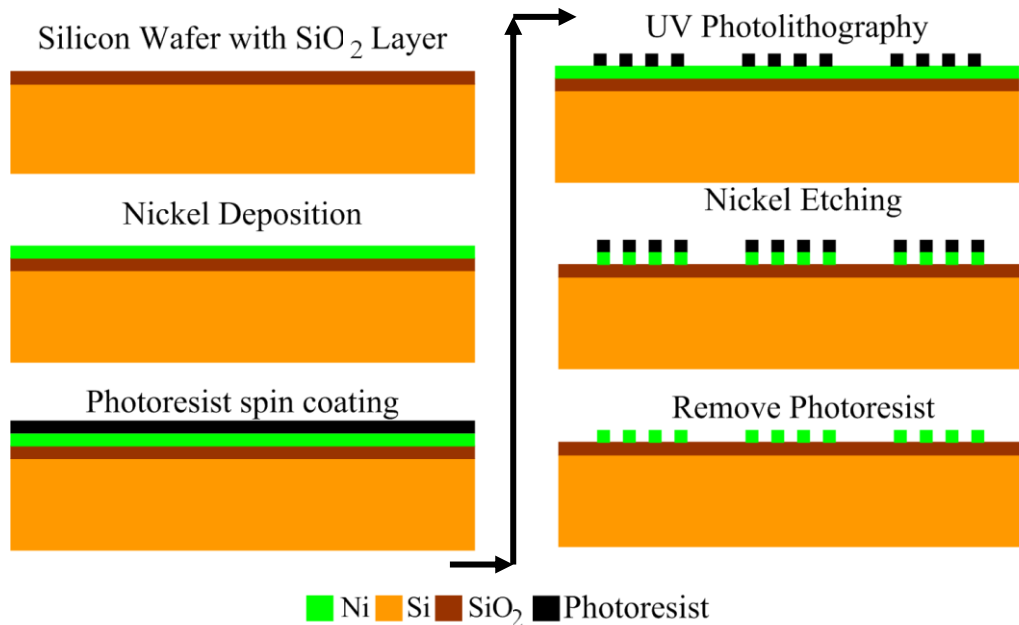

Figure 3.10 Fabrication process of Ni based temperature sensors.

Table 3.4 Composition of nickel etchant.

Acetic acid	9.375g
Nitric acid	9.375g
Sulfuric acid	3g
DI-water	127.5g

The photographs of the fabricated sensors, taken using an Olympus SZX10 advanced routine stereo zoom microscope, are shown in Fig. 3.11. Sensors in different dimensions were tested with a multimeter while the sensors were placed on a controlled hotplate and the temperatures were recorded using a temperature probe. The test results are shown in Fig. 3.12.

(a) Sensor with 5 μm track width

(b) Sensor with 10 μm track width

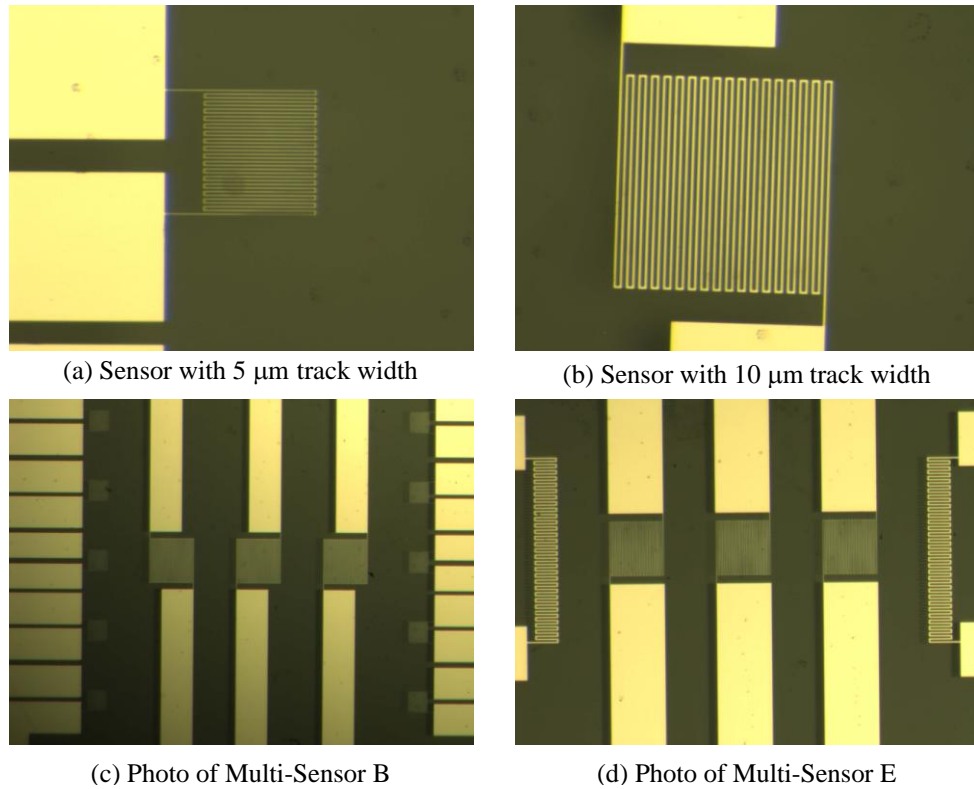(c) Photo of Multi-Sensor B

(d) Photo of Multi-Sensor E

Figure 3.11 Photos of the fabricated Ni temperature sensors.
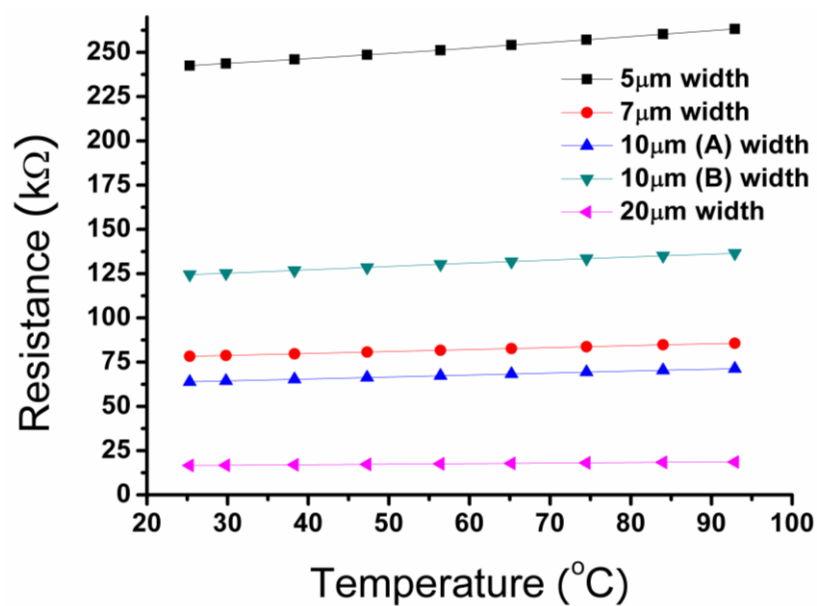

Figure 3.12 Test results of nickel thin film temperature sensors.

The behaviour of a sensor with 5 μm of track width is shown in Fig. 3.13, the sensitivity of which is about 32.25 mV/K of 0.1 mA with constant current. This is higher than that of the original design because large initial resistance was obtained while the nickel film was deposited thinner (<20nm) with the electron beam evaporation process.

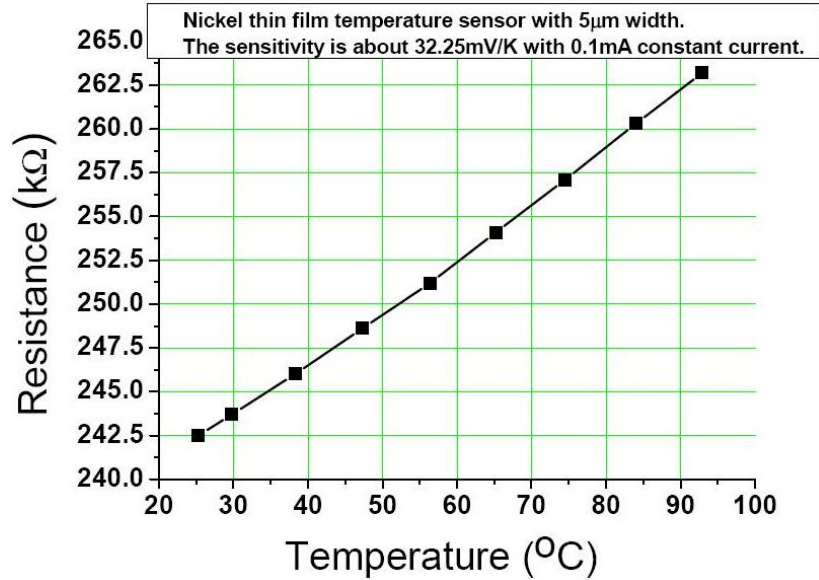Figure 3.13 The resistance response of a sensor with 5μm track width.

3.5   Fabrication and Testing of Platinum Based Temperature Sensor Arrays

Fig. 3.14 (a) shows a schematic layout of a thin film microsensor array, which was designed and fabricated for the embedded accurate temperature monitoring in laser assisted polymer bonding for MEMS packaging. The layout of the peripheral sensors was designed to be aligned within the polymer bonding track for monitoring the bonding temperature. The square polymer ring is illustrated by the track between the dotted lines. Inside the bonding ring, three sensors are used to monitor the temperature inside the cavity, providing useful information about the temperature distribution along with the peripheral sensors placed within the cavity. A lower temperature at the centre of the cavity is desirable for packaging of temperature sensitive devices. The internal dimensions of the polymer ring are 4.8 mm × 4.8 mm and the track width is 400 μm. The thin film resistance temperature sensor arrays are based on meander designs in order to minimize the sensor size required for this work. Sputtered platinum films on glass and silicon wafers were used to fabricate the sensor arrays. Table 3.5 shows the design parameters of the sensors. The track width is the same for all of the peripheral sensors in an array.   Track widths of 3 μm and 5 μm were used for the peripheral sensors and the width is the same for all of the peripheral sensors in an individual array.

For the sensors with track width of 3 μm, the resultant footprint is only 250 μm × 240 μm. The width of the peripheral sensors is less than the width of 400 μm of the BCB rings to ensure that the sensors are completely embedded underneath the BCB polymer track. The track width of all of the inner sensors was designed to be 10 μm.
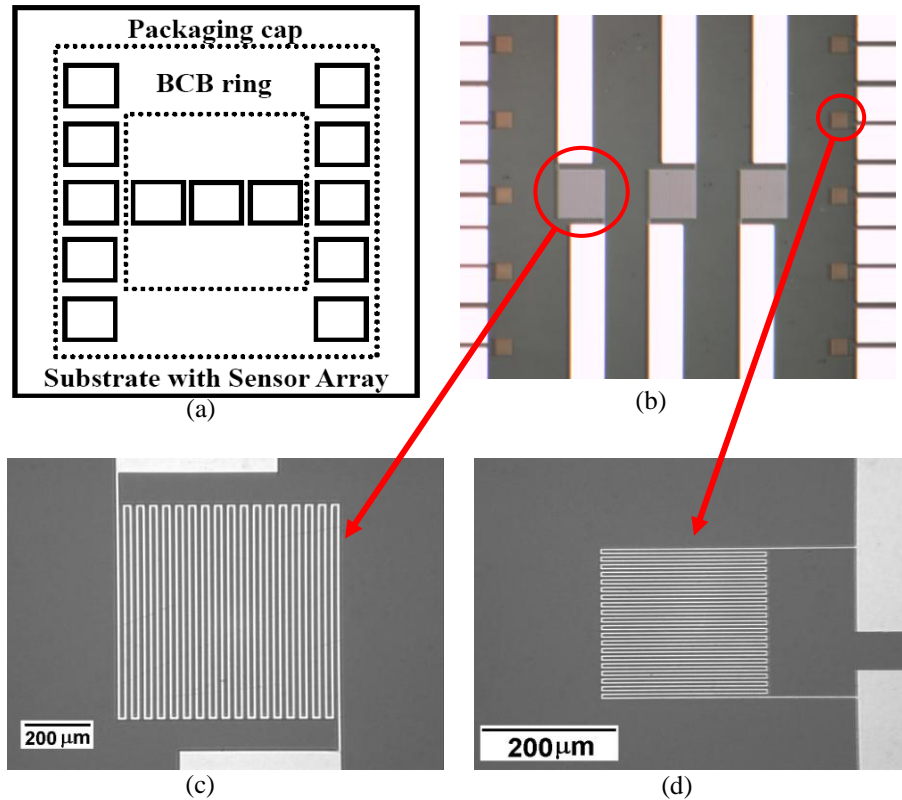

Figure 3.14 (a) Schematic layout of a sensor array; (b) Picture of a platinum based microsensor array; (c) Picture of a central sensor with a track width of 10 μm; (d) Picture of a peripheral sensor with a track width of 3 μm.

The thin film resistive temperature sensors were fabricated using sputtered platinum films on silicon wafers and Pyrex glass wafers, the process flow of which is shown in Fig. 3.15. The silicon wafers have a pre-deposited layer of silicon dioxide of 1 μm of thickness. The thickness of the platinum films was about 100 nm. A layer of titanium of ~10 nm was used as the adhesion layer between the platinum film and the wafer surface. After the deposition of the platinum film on a wafer, the photoresist was spin coated and patterned by the photolithography process. With the photoresist as the mask, the platinum films were patterned using an ion beam etching method to produce the sensor arrays. The fabrication process of Pyrex glass wafers is the same as that of the silicon wafers. Fig. 3.14 (b) shows an optical picture of a fabricated platinum sensor array. The pictures of a central sensor and a peripheral sensor are shown in Fig. 3.14 (c)

and (d) respectively. It can be seen that microsensors with the track width as narrow as 3 μm have been obtained successfully.

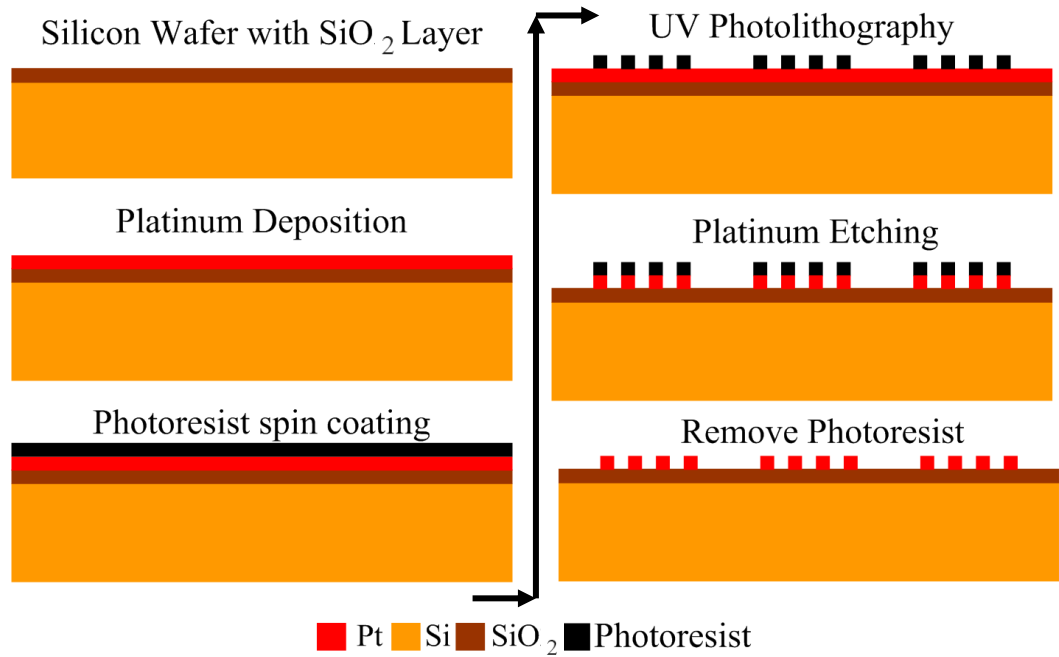Figure 3.15 Fabrication process of Pt based temperature sensors.

Table 3.5 Design Parameters for the Temperature Sensors.

Width (μm)	Length (μm)	Number of periods	Area of a single sensor (μm^2)
3	250	40	250×240
5	300	34	300×340
10	700	36	700×700

The temperature dependence of the resistance of the sensors was determined using a hotplate and a digital multimeter. The initial measurements showed a drift of resistance by about 7% after the first cycle of measurement between 25 ℃ and 300 ℃. For process monitoring, a stable resistance is required to obtain a reliable value of temperature for each incident laser power and temperature above 300 ℃ commonly stabilized the contacts. Therefore, an annealing process was conducted on the sensors to determine if the drift effect of the resistance could be eliminated. It was found that after annealing for 5 hours at 350 ℃, the resistance of the sensors at each temperature is stable in the

subsequent temperature cycles of the measurement. Fig. 3.16 shows the linear behaviour of the thermal responses of the platinum sensors after annealing of sensors with track width of 3, 5 and 10 μm respectively. The corresponding temperature coefficients of resistance (TCR) were determined to be from $1.78 \times 10^{-3} / ℃$ to $2.26 \times 10^{-3} / ℃$ at $20 ℃$.
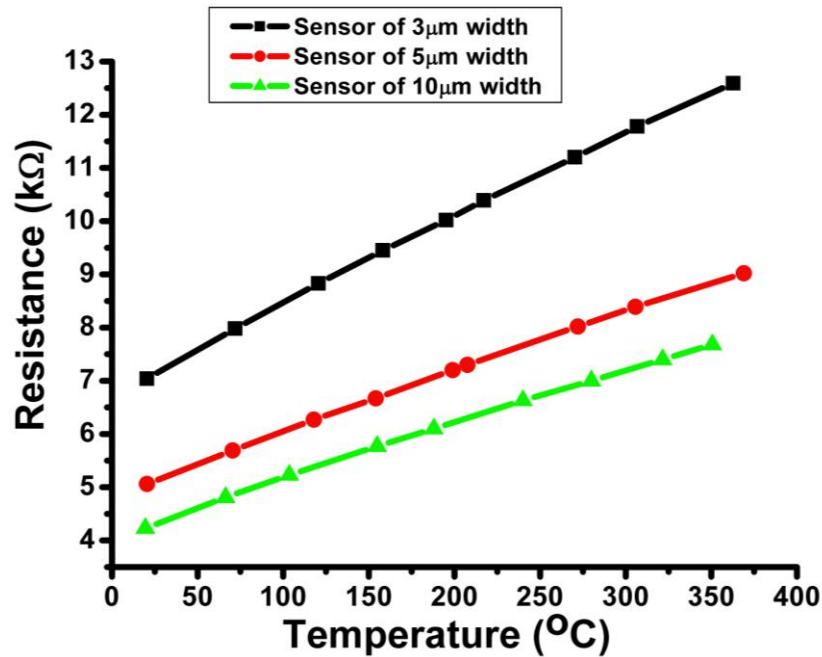

Figure 3.16 Thermal response of platinum sensors.

3.6   Summary

Theoretical studies have been conducted to investigate metal thin film based temperature sensors. Meander suspended sensors have been designed and modelled using a commercial FEM simulation software package, ANSYS. The sensor structures, the effect of self heating and air convection, were extracted from the simulated solutions. The results show that the inside corners of the meander structures had the higher temperature, where the resistance is lower compared with the outside corners. The self-heating effect was less significant in a sensor with a larger resistance. Effect of air convection could be ignored for a sensor with large resistance.

After the theoretical calculations and the FEM simulations, a 5-inch chrome film based soda lime glass photomask has been designed and manufactured for the sensor fabrication. Nickel based sensors were fabricated using electron beam evaporation and wet etching methods, and platinum based sensors were produced via sputtered

deposition and ion beam etching methods. The sensors with meander tracks with widths of 3 μm have been obtained successfully, resulting in a sensor footprint of 250 μm × 240 μm. The behaviour of a nickel based sensor with 5 μm of track width shows a temperature sensitivity of 32.25mV/K with 0.1mA of constant current. After annealing at 350 °C to stabilise the metal films and produce reliable and repeatable measurements, the corresponding temperature coefficients of resistance (TCR) of the platinum based sensors were determined to be between $1.78 \times 10^{-3}/°C$ and $2.26 \times 10^{-3}/°C$ at 20 °C.

Chapter 4   Accurate Temperature Monitoring Using an Embedded Microsensor Array for Laser Bonding

Temperature monitoring is important in many processes and systems as excessive temperature change can result in detrimental effects and catastrophic failure of processes and systems. Effective process monitoring methods have been demonstrated previously for multi-processes [70, 71]. Recently polymer based bonding methods have become attractive for MEMS packaging since polymer materials such as benzocyclobutene (BCB) have many desirable properties for packaging applications including thermosetting, low temperature processing at 250 ℃ ~ 350 ℃, low moisture uptake, excellent electrical dielectric properties, and good chemical and thermal stabilities [139-143]. Extensive studies of BCB bonding for MEMS packaging have been carried out using conventional heating methods based on heated chucks on a device or wafer bonder [144-149].

At Heriot-Watt University, a fast laser bonding method using the BCB polymer for MEMS packaging applications has been demonstrated [150]. Reliable substrate bonding was achieved in seconds using this method. The laser based approach can reduce/eliminate the potential damage of devices using rapid, localized heating effects [150, 151]. However, due to the localized nature of the temperature change, it is difficult to monitor the precise temperature change within the substrate assembly during the bonding process. Secondly the thermal response of the substrate assembly under bonding depends on several factors such as laser power, beam profile, the structures of the package assembly as well as the design of the bonding setup. Thirdly, precise temperature monitoring is important for polymers such as BCB as the curing time is highly dependent on the curing temperature. For BCB, a curing time of several minutes is required at ~250 ℃ while it is seconds at around 300 ℃. In the previous work, conventional methods based on infrared detection [150] and thermo-sensitive paints [152] were used for temperature monitoring. But these methods could not provide the precise information about the temperature change within the polymer bonding track and the temperature distribution within the packaging assembly.

Based on fabricated platinum based temperature sensor arrays, we present the experimental studies of a temperature monitoring method using an embedded

microsensor array in the packaging assembly, for accurate temperature monitoring of the laser assisted polymer bonding process for MEMS packaging. A diode laser system with a fibre-coupled output was used in the temperature monitoring experiments. Custom designed beam shaping optical elements were used to transform the laser beam into top-hat and frame-shaped beam profiles for energy efficient laser bonding and investigation of the effect of beam profiles on the resultant temperature change and distribution.

4.1   The Laser Bonding System

A high power diode laser system with a fibre-coupled output at 970 nm was used as an energy efficient laser source in the study of the temperature monitoring method using an embedded microsensor array. Fig. 4.1 shows a schematic of the experimental setup. The substrate assembly to be bonded using a BCB polymer ring was placed on the bonding platform. A 0.9 mm thick ceramic plate was used to investigate the effect of thermal isolation between the bottom substrate and the stainless steel bonding platform.
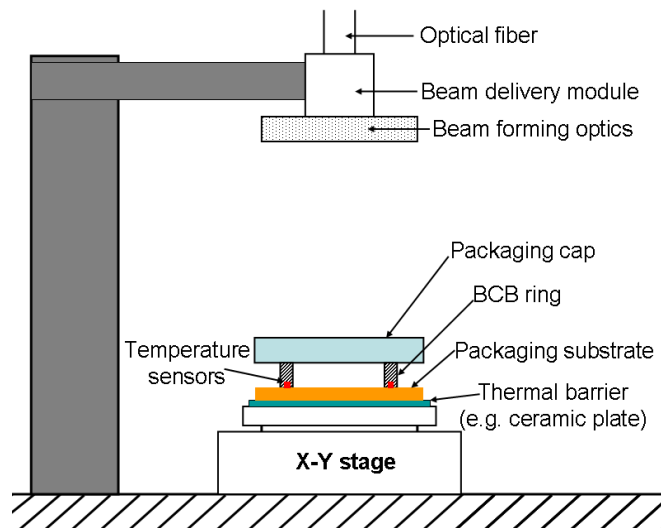

Figure 4.1 Schematic setup of the bench top laser bonding system.

For energy efficient bonding and investigation of the effect of the beam profile on the amplitude and distribution of temperature, top-hat and frame-shaped beam profiles were used in these experiments. The beam profiles were generated using custom designed planar beam forming optical elements. The beam forming optical element was mounted in front of the beam delivery module that was coupled to the optical fibre cable from the laser system. The beam delivery module consists of collimation optics followed by a focusing lens with a focal length of 20 cm. Fig. 4.2 (a) and (b) show the schematic

60

illustration of the laser beam profiles used in the experiments. It should be noted that when the capping substrate is transparent the bottom substrate was used to absorb the laser radiation. Fig. 4.2 (c)-(f) show the images and typical intensity distributions of the two beam profiles. The dimensions of the top-hat beam for bonding were 6 mm $\times$ 6 mm. The outer dimensions of the frame-shaped beam were also 6 mm $\times$ 6 mm, most of the optical power was concentrated in the area of the 1 mm wide ring. It should be noted that for the frame-shaped beam profile, the beam intensity inside the frame was about 12%~17% of the peak intensity around the frame.
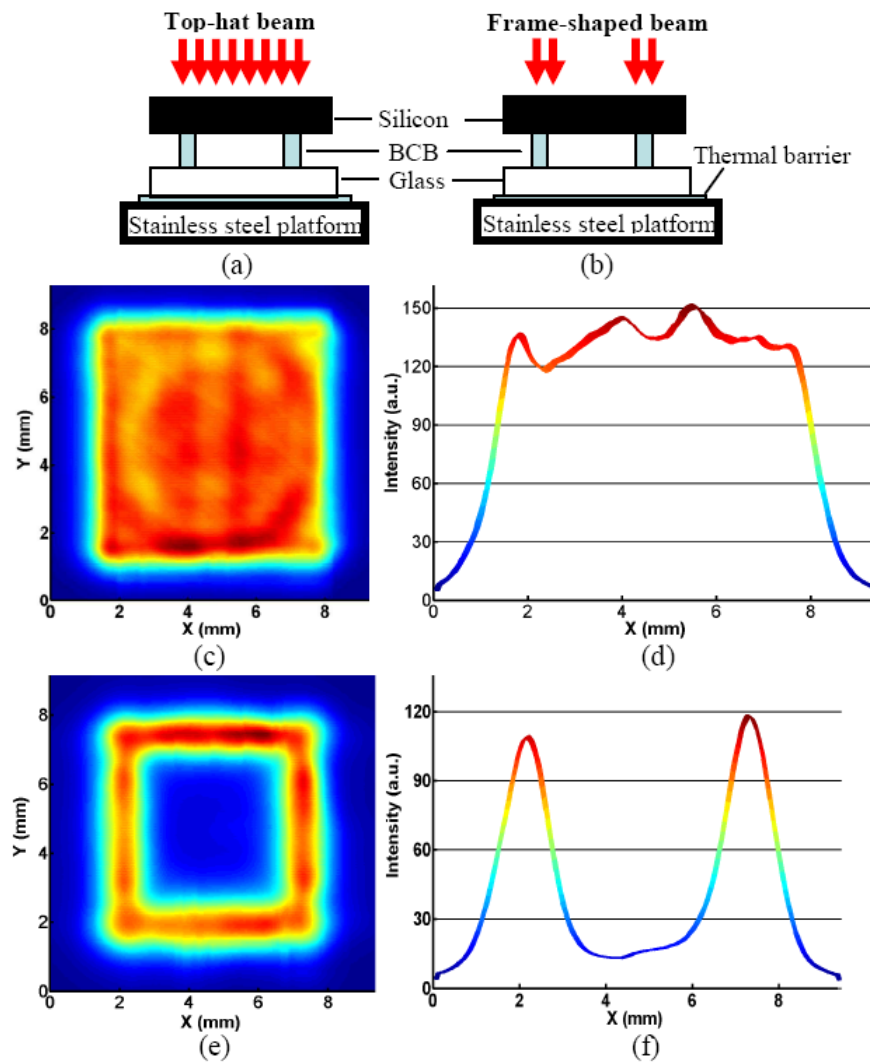

Figure 4.2 (a) Schematic diagram of laser assisted polymer bonding using top-hat beam, (b) the corresponding schematic diagram using frame-shaped beam, (c) an optical image of the top-hat beam, (d) typical intensity distribution of the top-hat beam, (e) an optical image of the frame-shaped beam, and (f) typical intensity distribution of the frame-shaped laser beam.

The frame-shaped beam allows delivery of the laser power to the area of interest for bonding and, in principle, it is possible to reduce the temperature rise at the centre of the cavity and therefore reduce the thermal load to the MEMS device to be packaged. Optical spectroscopic measurements showed the optical transmission of the 500 μm thick silicon substrate at the laser wavelength of 970 nm is negligible. Therefore all of the laser beam entering the silicon substrate was absorbed and converted to a thermal effect. The scattering loss of the unpolished backside of the silicon was approximately 20%. The laser power levels stated are values before correction for scattering loss.

4.2   Fabrication of BCB Ring and Pre-alignment of Sensor Array

The polymer sealing rings were fabricated using a photosensitive BCB polymer (CYCLOTENE 4026-46, Dow Chemical). BCB material can produce a strong and reliable bond between substrates and has been studied widely for MEMS packaging applications. A unique characteristic of the BCB polymer is that fast curing can be realized within a few seconds at temperature of ~300 ℃ instead of minutes at ~250 ℃ [142, 143]. This fast curing behaviour is ideal for the laser assisted bonding process in which a rapid temperature rise can be achieved. The BCB sealing rings were produced on silicon and glass wafers using UV photolithography. Details of the fabrication process were described previously by our group in Heriot-Watt University [151]. After fabrication, the wafer was diced into square chips each containing a BCB ring. An optical picture of a square BCB ring on a glass capping substrate is shown in Fig. 4.3. The outer dimensions of the BCB ring were 5.2 mm $\times$ 5.2 mm and the track width was 400 μm. The thickness of the BCB ring was measured on a ZYGO white light interferometer and was determined to be ~10 μm.
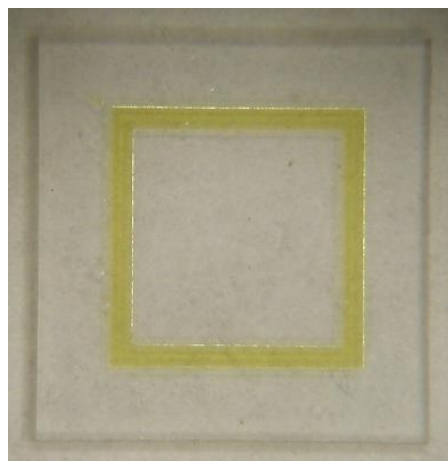

Figure 4.3 Optical picture of a fabricated BCB ring on a glass cap.

In order to obtain good alignment between the BCB polymer ring and the sensor array for temperature monitoring, the packaging cap was attached to the sensor substrate on a flip chip bonder in a pre-bonding step prior to laser assisted bonding. The pre-bonding process was carried out at 100 ℃ for 5 minutes. An optical picture of the pre-bonded glass-silicon assembly is shown in Fig. 4.4. The substrate assembly consists of a silicon cap attached to a glass substrate with a sensor array. It can be seen that all of the peripheral sensors were well placed under the BCB track. Electrical leads were then attached to the contact pads of the sensors for in-situ temperature monitoring during the laser assisted bonding experiments.
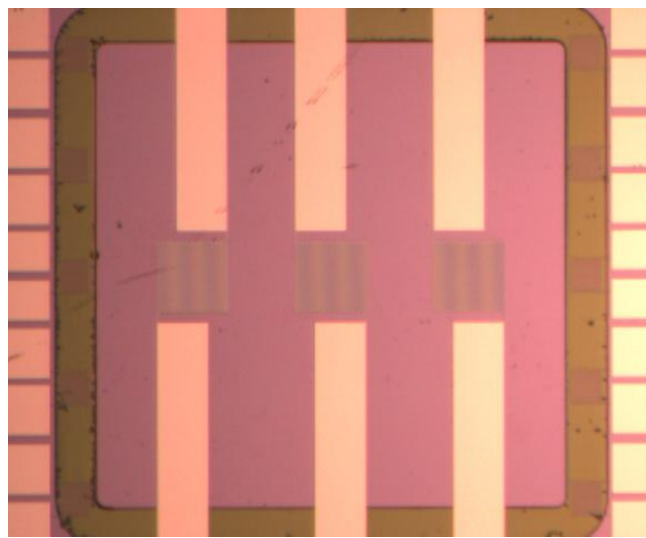

(a)
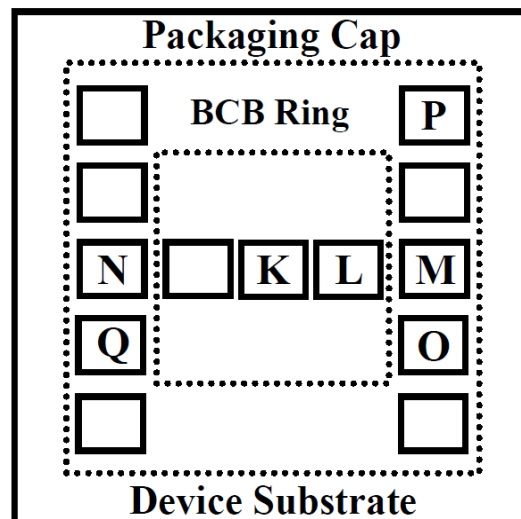
(b)

Figure 4.4 (a) Picture of a glass-silicon assembly after pre-bonding

(b) The location of sensors monitored by the data acquisition device.

## 4.3   Embedded Temperature Monitoring of Laser Assisted Bonding

In the temperature monitoring experiments, the top-hat laser beam or frame-shaped beam generated using the beam forming optical elements was aligned to the polymer bonding ring. In bonding of glass and silicon substrates the silicon substrate absorbs the laser radiation and produces the required temperature change to cure the BCB polymer. In silicon to silicon bonding the capping (top) substrate absorbs the laser radiation. The sensor array was on the surface of the bottom substrate in all of the experiments. The resistance change of each sensor as a result of the temperature change was monitored using a custom designed circuit. The resultant voltage signals from the sensor array were recorded and displayed on a computer using a data acquisition device (NI-DAQ-6008, National Instruments).

4.3.1   *Bonding Glass Cap to Silicon Substrate*

Silicon is one of the most commonly used substrate materials for MEMS fabrication. The silicon substrates can absorb laser radiation to produce the required temperature rise for BCB curing when a glass cap is used. In this case the thin film sensor array was fabricated on the silicon chip and used for in-situ temperature monitoring. The laser heating was absorbed by the bottom substrates. To improve thermal efficiency, a 0.9 mm thick ceramic plate was placed between the silicon substrate and stainless steel platform. Fig. 4.5 shows the temporal profiles of the laser induced temperature monitored by the sensor array. Fig. 4.5 (a) shows the traces of temperature for different laser powers for both of the top-hat and frame-shaped laser beams. A laser power of 50 W was sufficient to raise the temperature to 300 ℃ within 50 seconds to cure the BCB ring, producing a strong bond between the substrates to form a microcavity. Fig. 4.5 (b) shows the comparison of the temperature between a peripheral sensor and the sensor at the centre of the array. There is no noticeable difference between the signals for the top-hat beam indicating that the temperature experienced by MEMS device would be the same as the bonding temperature. However, as will be shown in the following, the frame-shaped beam profile can produce a lower temperature at the centre of the silicon substrate by ~50 ℃ than the bonding temperature when bonding a silicon cap to a glass substrate. This is a desirable effect for packaging of temperature sensitive devices.
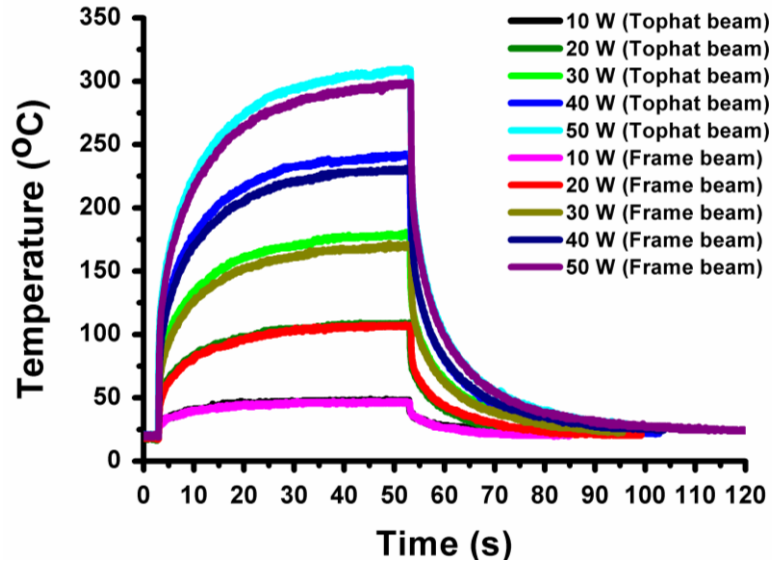
(a)
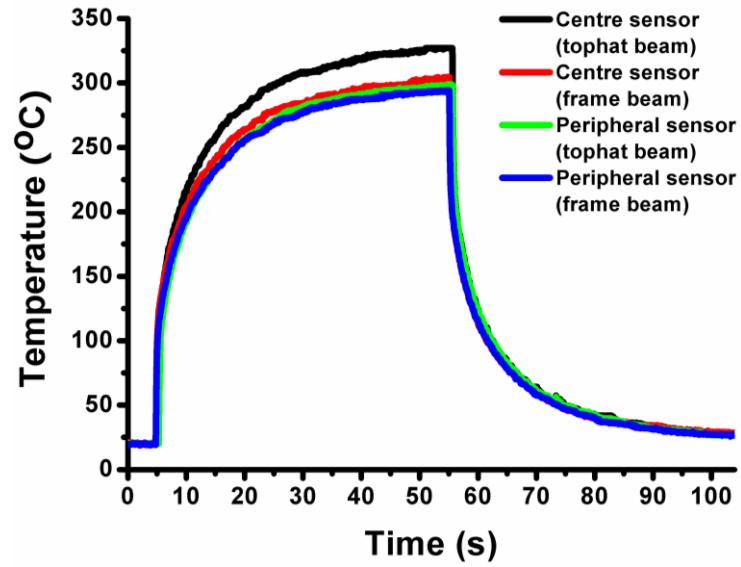
(b)

Figure 4.5 (a) Temperature profiles of laser bonding between glass cap and silicon substrate monitored by a peripheral sensor (P), (b) comparison of temperature characteristics at a laser power of 50 W monitored by a centre sensor (K) and a peripheral sensor (P).
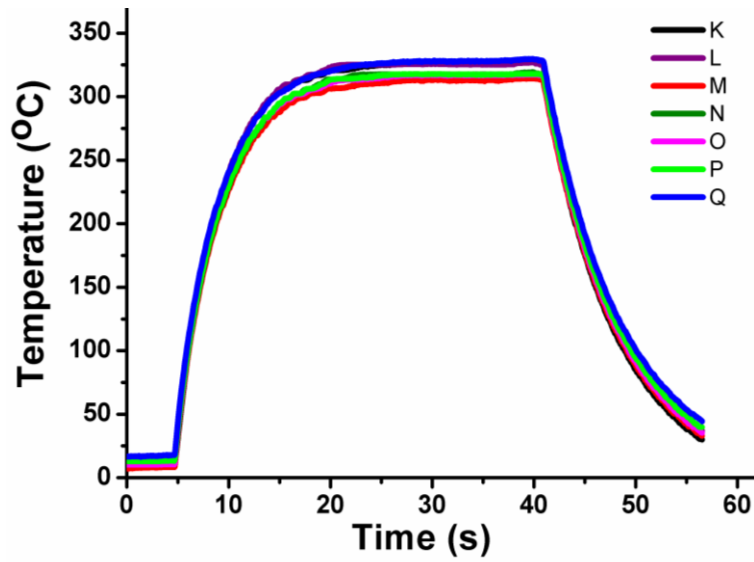
4.3.2 Bonding Silicon Cap to Glass Substrate

In this case the silicon cap absorbs the laser power to generate the required temperature for BCB curing. The microsensor array was fabricated on the glass substrate (Pyrex 7740). The bonding arrangement was the same as in the above experiment. Fig. 4.6 shows the measured results of the temperature profiles from the sensors in the array for the top-hat beam at optical power of 10 W and 20 W respectively. The measured temperature characteristics were the same for all of the sensors for the top-hat beam.

But a temperature difference of about 50 ℃ between that of a peripheral sensor and the sensor at the centre of the array (P and K in Fig. 4.4 (b) respectively) was seen for the frame-shaped beam as shown in Fig. 4.7.
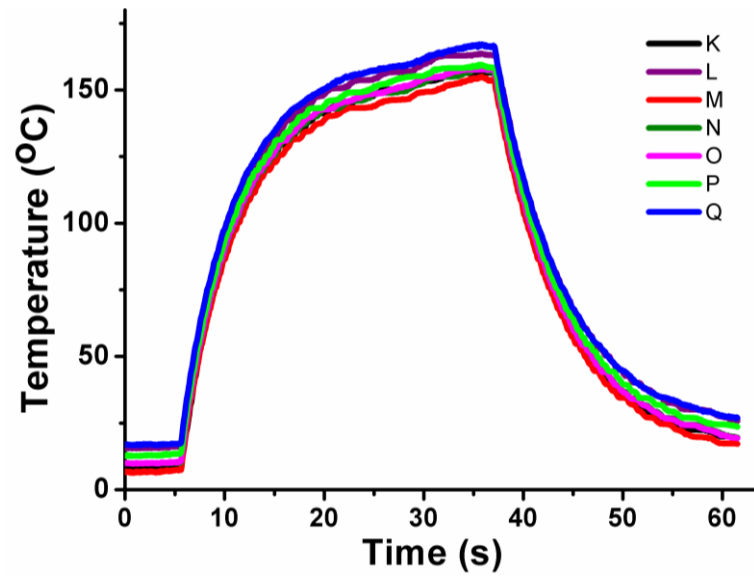
(a)

(b)

Figure 4.6 Temperature profiles monitored by the sensors for the top-hat beam at the laser power of (a) 10 W and (b) 20 W.
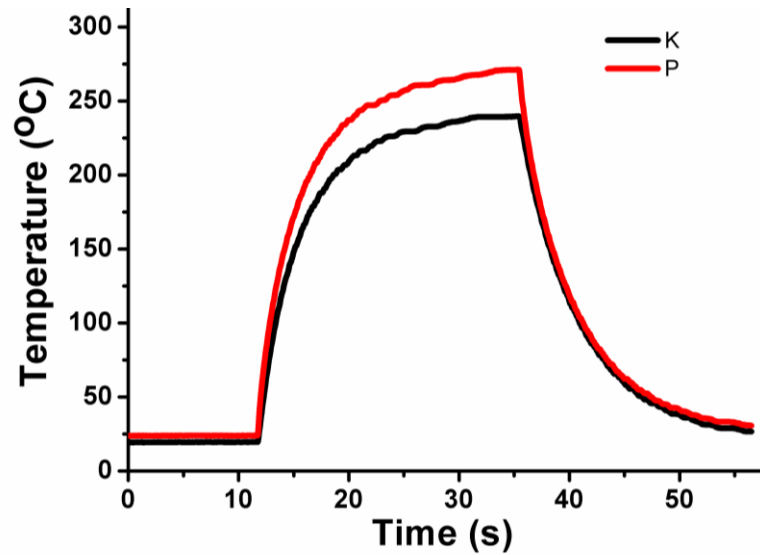
Figure 4.7 Temperature profiles of bonding silicon cap to glass substrate at a laser power of 20 W using the frame-shaped beam.

In this bonding configuration the thermal efficiency is much higher than having the silicon chip as the bottom substrate. An optical power of 20 W was sufficient to produce a temperature of ~300 ℃ as compared to a required laser power of 50 W when bonding the glass cap to the silicon substrate, described previously. This is due to the thermal conductivity of the Pyrex glass being two orders of amplitude lower than that of silicon so the heat dissipation to the bonding platform is much faster in bonding the glass cap to the silicon substrate. The thermal conductivities of the substrate materials, the ceramic plate and the stainless steel platform are given in Table 4.1. The silicon substrates lose the heat more quickly than the glass substrates.

Table 4.1 Thermal Conductivities of Materials.

Materials	Thermal conductivity (W/(m K))
Silicon	130
Glass (Pyrex 7740)	1.1
Ceramic (Al_2O_3)	35
Stainless steel	237

### 4.3.3 Bonding Silicon Cap to Silicon Substrate

Silicon to silicon bonding is desirable in many applications where optical transparency through the cap is not a requirement. Silicon to silicon bonding has no thermal

mismatch between the substrates and therefore eliminates the CTE (coefficient of temperature expansion) induced stress, thus improving the thermal-mechanical reliability of the package. In bonding the silicon cap to the silicon substrate, the laser radiation is absorbed by the top (capping) silicon substrate. This is the same as for bonding of the silicon cap to the glass substrate described previously.
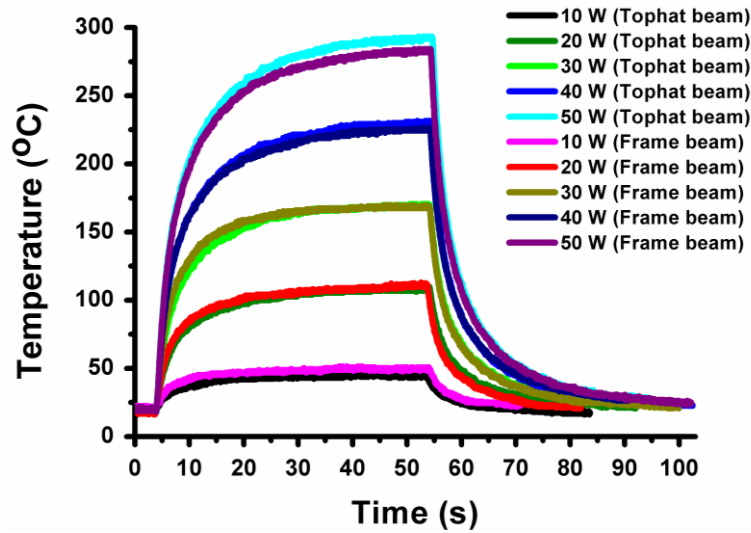
(a)
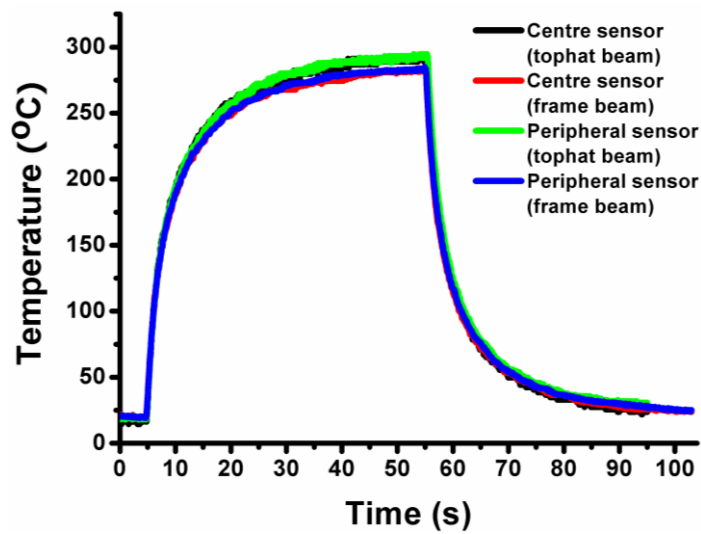
(b)

Figure 4.8 (a) Temperature profiles of silicon to silicon bonding monitored by a peripheral sensor (P), (b) comparison of temperature from a centre sensor (K) and a peripheral sensor (P) for a laser power of 50 W.

Fig. 4.8 shows the results of temperature monitoring in the laser bonding process. It is interesting to see that there is little difference between the results for the top-hat and frame-shaped beam profiles for the same laser power. This is a result of the rapid

diffusion of the laser generated thermal energy within the silicon substrates due to the high thermal conductivity of silicon. The thermal efficiency for the same laser power is similar to that of bonding a glass cap to a silicon substrate. The result shows that it requires a laser power of ~ 50 W to produce a temperature rise of ~ 300 ℃.

4.4 Study of Heat Dissipation Under Substrate Assembly

The effect of thermal dissipation under the bottom substrate was investigated using the top-hat beam profile for bonding of a silicon cap and a glass substrate at 20 W of laser power. Three different thermal configurations were used between the bottom substrate and the bonding platform, including

    (1)   A 0.9 mm thick ceramic plate,

    (2)   A 0.5 mm thick silicon wafer and

    (3)   Without an intermediate thermal barrier between the bottom substrate and the stainless steel platform.
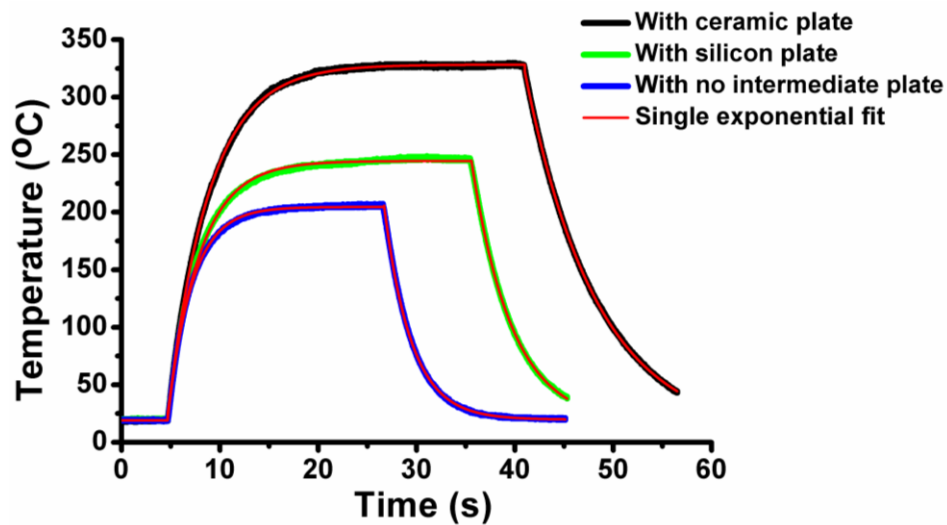

Figure 4.9 Temperature profiles for different thermal configurations at a laser power of 20 W using the top-hat beam monitored by a peripheral sensor (P).

The results are shown in Fig. 4.9. As expected, it can be seen that the maximum temperature decreases as the heat dissipation under the sensor substrate increases. This shows it is useful to add a thermal barrier between the substrate and the bonding platform in order to improve the efficiency of the laser heating effect. It has been found that the temperature responses can be described using a single exponential function that is discussed in the next section. Fig. 4.10 and 4.11 show the corresponding results for bonding of a glass cap to a silicon substrate and a silicon cap to a silicon substrate

bonding respectively. The laser power was 50 W in both cases. Without an intermediate thermal barrier between the silicon substrate and the bonding platform, a fast rise and fall of the temperature can be achieved. This thermal behaviour demonstrates the potential of the bonding method for high speed bonding applications.
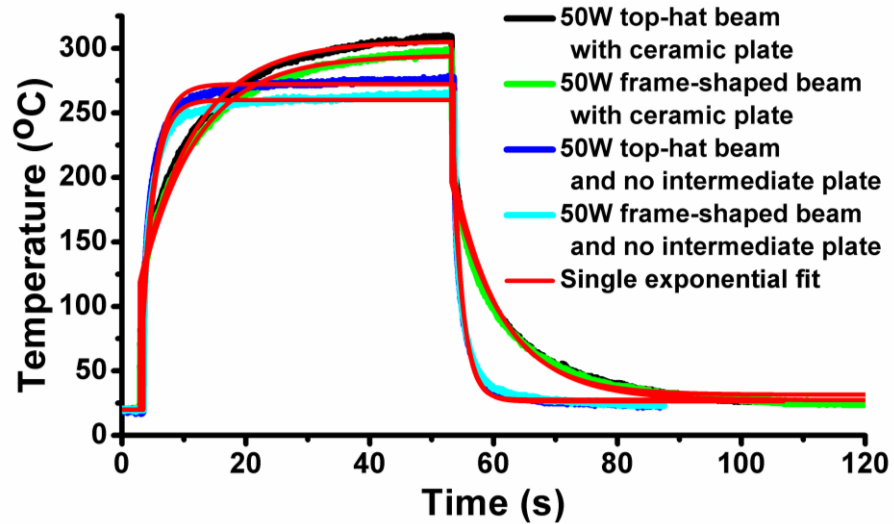

Figure 4.10 The effect of heat dissipation under silicon substrate measured by a peripheral sensor (P) with track width of 3 μm on laser induced temperature rise when bonding to glass cap at 50 W of laser power.

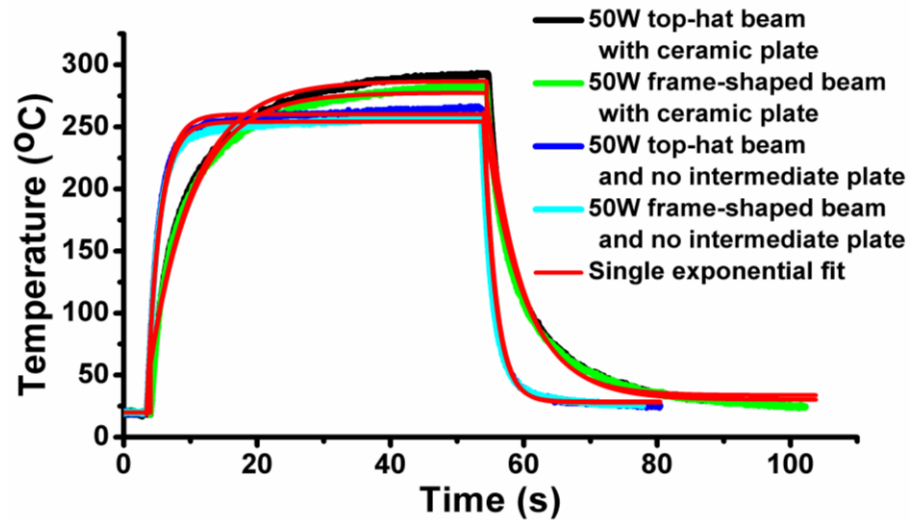

Figure 4.11 The effect of heat dissipation under silicon substrate measured by a peripheral sensor (P) with track width of 3 μm on laser induced temperature rise when bonding to silicon cap at 50 W of laser power.

It has been found that the experimental results of the temperature characteristics can be described accurately using the following single exponential function shown in Equation

70

(4.1), where t_1 and t_2 are the onset and termination time of the laser power, T_0 is the ambient temperature, T_s is the steady state temperature for the given laser power, T_i is the temperature at the termination time of the laser power, and τ_1 and τ_2 are the rise time and fall time of the laser induced temperature respectively.

$$
T(t) = \begin{cases} T_0, & t < t_1 \\[2ex] T_0 + \left(T_s - T_0\right)\left(1 - e^{-\frac{t - t_1}{\tau_1}}\right), & t_1 \leq t \leq t_2 \\[2ex] T_0 + \left(T_i - T_0\right)e^{-\frac{t - t_2}{\tau_2}}, & t > t_2 \end{cases} \qquad (4.1)
$$

By fitting the experimental results presented in Fig. 4.5 – 4.11 using Equation (4.1), the thermal constants τ_1 and τ_2 have been obtained for different substrate assemblies and heat dissipation configurations. The results are summarized in Table 4.2. The thermal constants are largely independent of the beam profile, by comparison studying of tests 4&5, 6&7, 8&9, 10&11. The results of test 3&6 and 7&11 show that the thermal constants are also less dependent on the cap and substrate materials (glass or silicon) when the bonding process is carried out without the intermediate thermal barrier. However, the thermal constants are larger for a silicon cap to a silicon substrate bonding with the ceramic plate between the substrate assembly and the bonding platform, which are shown in results of test 4&5.

Table 4.2 Thermal Constants for Different Bonding Configurations.

Test No.	Material			Beam Profile	Thermal Constant	
	Cap	Substrate	Thermal barrier		τ_1 (s)	τ_2 (s)
1	Silicon	Glass	Ceramic	Top-hat	4.15	7.30
2	Silicon	Glass	Silicon	Top-hat	3.28	4.12
3	Silicon	Glass	None	Top-hat	2.44	2.76
4	Silicon	Silicon	Ceramic	Top-hat	9.05	7.59
5	Silicon	Silicon	Ceramic	Frame beam	9.03	8.53
6	Silicon	Silicon	None	Top-hat	2.13	1.73
7	Silicon	Silicon	None	Frame beam	1.93	1.54
8	Glass	Silicon	Ceramic	Top-hat	6.69	5.30
9	Glass	Silicon	Ceramic	Frame beam	6.48	5.97
10	Glass	Silicon	None	Top-hat	1.94	1.84
11	Glass	Silicon	None	Frame beam	1.93	1.82

4.5 Summary

Accurate temperature monitoring using an embedded microsensor array has been demonstrated successfully in laser assisted bonding for MEMS packaging applications. It has been shown that the amplitude and characteristic of the laser generated temperature change, not only depends on the laser power but also depends on the package assembly to be bonded and the configuration of thermal materials in the bonding setup. Therefore it is necessary to monitor the laser induced temperature for better process control in a manufacturing environment. The effect of beam profile on the resultant temperature change and distribution has been investigated using top-hat and frame-shaped beam profiles. It was found that it is possible to produce a lower temperature at the centre of the bottom substrate by ~50 ℃ using the frame-shaped laser beam profile. This effect is highly beneficial for packaging of temperature sensitive devices. With better thermal design for heat dissipation from the substrate, it is possible to achieve a larger temperature difference between the bonding temperature for

packaging and the temperature experienced by the device being packaged. It was found that the temperatures characteristics can be described using a single exponential function. The thermal constants are largely independent of the beam profiles but highly dependent on the thermal arrangement of the materials underneath the bottom substrate. An intermediate ceramic plate between the substrate and the stainless steel bonding platform can improve the thermal efficiency of the bonding laser power significantly.

Chapter 5   BCB Film Based SAW Humidity Sensor

Surface acoustic wave (SAW) devices are attractive for use in humidity sensors because of their small size, low cost, high stability, short response time, high sensitivity, good reliability, good reproducibility and capability of compatibility with the integrated circuit process. Moreover, the fabrication of SAW humidity sensors is much simpler and easier than the capacitive or resistive humidity sensor, using only one step photolithography instead of producing the parallel plate capacitors or the expensive ion implantation/diffusion processes. A SAW based humidity sensor has been proposed to be integrated as one of the multi-sensors for embedded health monitoring in SiP based Microsystems. Instead of the conventional polymer based moisture absorbing layer, such as polyimide, fluoropolyol (FPOL), and polyvinyl-alcohol (PVA), the benzocyclobutene (BCB) polymer has been investigated as the sensing film for absorbing moisture [120-122]. Using changes in mass loading due to the uptake of moisture by the polymer, changes in relative humidity (RH) levels resulting in the shift of both centre frequency and amplitude of the SAW resonators have been measured. The SAW resonators have been fabricated with metal interdigital transducer (IDT) fingers based on piezoelectric substrates [120-122, 153-156].

5.1   BCB and Moisture Capture

CYCLOTENE, a series of advanced electronics resins from the Dow Chemical Company (USA), are high-purity polymer solutions that have been developed for microelectronics applications, which include wafer-level chip-scale packaging, dielectric isolation for multilayer interconnects, strong and void-free bonds for MEMS and 3D integration, printed circuit board technology, integrated passives/radio frequency (RF) components, active matrix liquid crystal displays, passivation/stress buffer, etc.. The resins are derived from B-staged bisbenzocyclobutene-based (BCB) monomers and are formulated as high-solids, low-viscosity solutions. The chemical formula of BCB and chemical equation of polymerization reaction are shown in Fig. 5.1 [142, 143].

The BCB based humidity sensing technology has already been studied and applied in monitoring the humidity level of human breath as well as in a pulmonary function diagnosis Microsystem [157-159]. For the convenience of using UV photolithography

processes as well as the resource availability, CYCLOTENE 4026-46 has been selected from the CYCLOTENE 4000 series advanced electronic resins. These resins come as I-line (365 nm), G-line (436 nm), and broad band-sensitive photopolymers. The electrical and thermal properties of Photo-BCB (CYCLOTENE 4000 resin series) are shown in Table 5.1, while the mechanical properties of photo-BCB are shown in Table 5.2 [142, 160]. The polymer resins have been used in the fabrication of a SAW based humidity sensor.
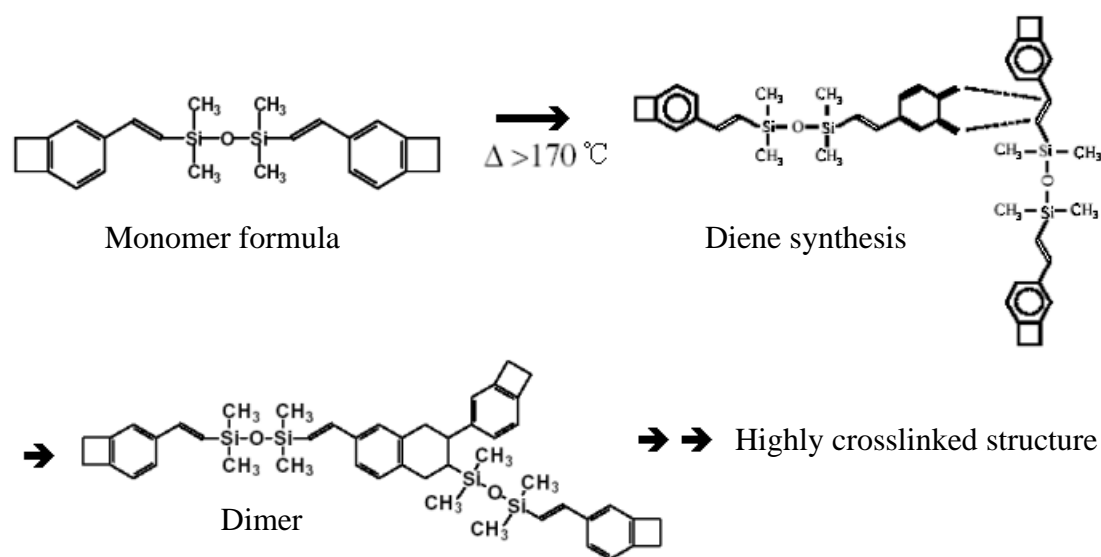

Figure 5.1 BCB formula and chemical crosslink equation.

Table 5.1 Electrical and thermal properties of Photo-BCB [142, 160].

Property	Value
Dielectric constant (1kHz – 20GHz)	2.65
Dissipation factor	0.0008
Breakdown voltage	5.3 MV/cm
Leakage current	4.7×10^{-10} A/cm^2 at 1.0 MV/cm
Volume resistivity	1×10^{19} Ω-cm
Thermal conductivity	0.29 W/mK at 24 °C
Thermal stability	1.7% weight loss per hour at 350 °C

Table 5.2 Mechanical properties of Photo-BCB [142, 160].

Property	Value
Coefficient of thermal expansion	42 ppm/°C at 25 °C
Glass transition temperature	>350 °C
Tensile modulus	2.9 ±0.2 GPa
Tensile strength	87 ±9 MPa
Elongation at break	8 ±2.5%
Poisson ratio	0.34
Stress on Si at 25 °C	28 ±2 MPa

Table 5.3 Recommended storage temperatures and times [142, 160].

Storage need	Temperature	Shelf Life
Long term	Freezer (-15 °C)	1 year from date of manufacture
Medium term	Refrigerator (4 °C)	1-2 months
Short term	Clean room (20 °C)	5 days

As photosensitive CYCLOTENE resin ages, the spun-on thickness will gradually increase as the resin becomes more viscous due to solvent evaporation. The lifetime is based on the criterion of less than 5% change in thickness. Resins should be allowed to equilibrate to room temperature before use. Recommended storage conditions and times are shown in Table 5.3. Several process options are available for CYCLOTENE 4000 series, and two of the typical process flows are shown in Fig. 5.2. Process A uses a hot plate soft bake and includes a develop end point monitor, and process B uses a hot plate soft bake and a pre-develop bake to stabilize the develop end point, while an oven soft bake is also possible. A spin coating was used for coating the BCB polymer onto the substrates. By increasing the spinning speed, the desired pre-exposure thickness could be achieved, the details of which are shown in Table 5.4 [142, 160].
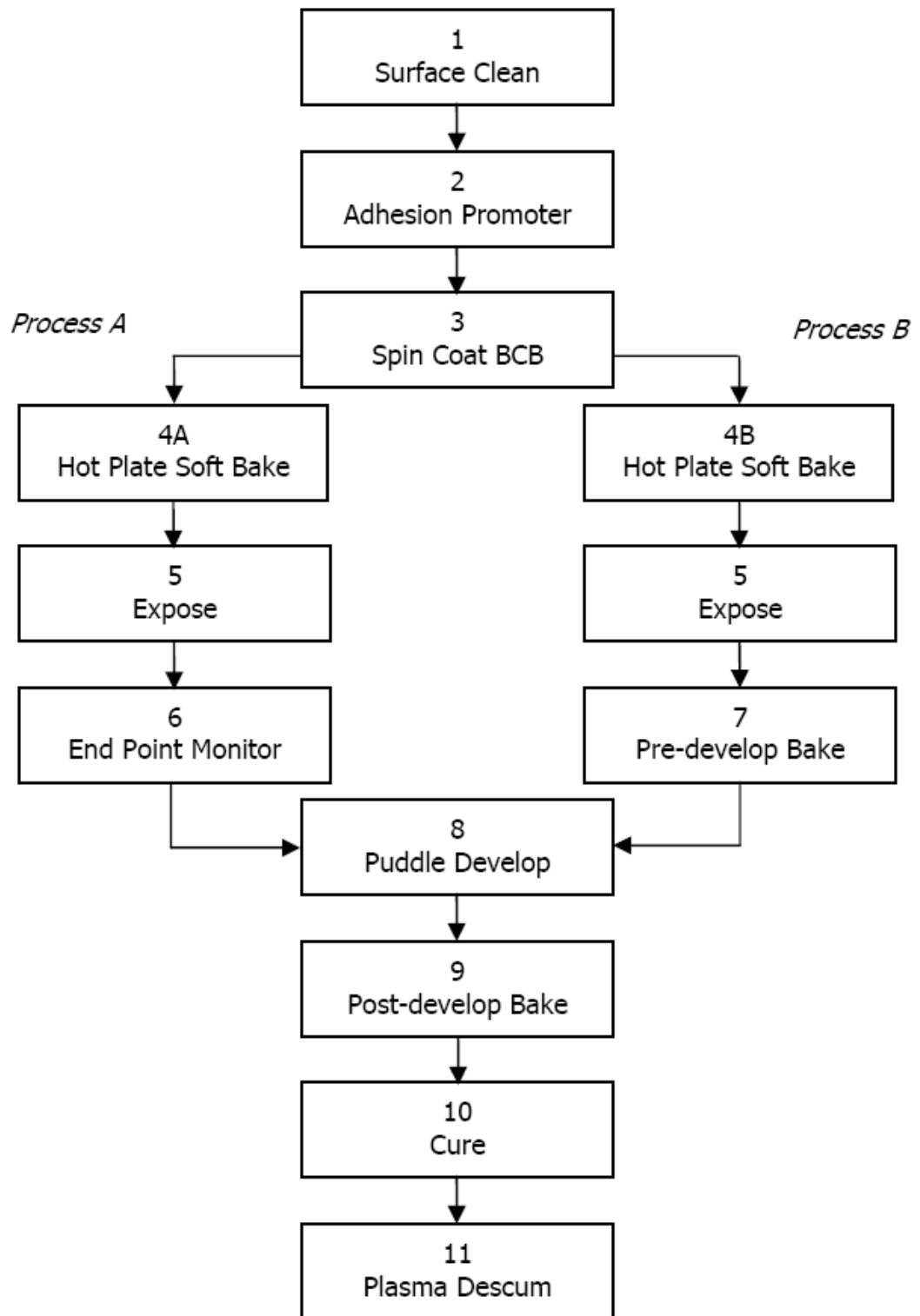
Figure 5.2 Process Flows for CYCLOTENE 4000 Series Resins [142, 160].

Table 5.4 Typical thickness of CYCLOTENE 4000 series polymers (4022-35, 4024-40 and 4026-46) after spin coating [142, 160].

Spin speed (rpm)	4022-35 thickness (μm)		4024-40 thickness (μm)		4026-46 thickness (μm)	
	After soft bake	Final thickness (hard bake)	After soft bake	Final thickness (hard bake)	After soft bake	Final thickness (hard bake)
1500	6.9	5.2	10.2	7.2	18.5	14.2
2000	5.8	4.3	8.4	5.9	15.2	11.6
2500	5.2	3.8	7.4	5.2	13.3	10.2
3000	4.7	3.4	6.7	4.8	12.2	9.4
3500	4.4	3.1	6.2	4.4	11.3	8.7
4000	4.1	2.9	5.8	4.1	10.6	8.1
5000	3.7	2.6	5.2	3.7	9.4	7.3

Table 5.5 Equilibrium wt % water in Photo-BCB at various RH at 23 °C [142, 160].

CYCLOTENE resin	Film thickness (μm)	Relative Humidity (%)		
		30	54	84
4024-40	5	0.061	0.075	0.14
4026-46	10	0.058	0.077	0.14
4026-46	20	0.050	0.082	0.14

Compared to epoxy resins, polyamides and other microelectronic polymers, BCB is well accepted because of its excellent properties such as water absorption (0.12% at 80% RH), planarization (e.g. > 90% for CYCLOTENE 3022), dielectric constant (2.5 at 1-10 GHz), dielectric loss at high frequency (e.g. 0.002 at 1-10 GHz), rapid curing (e.g. one minute on a hot plate under nitrogen), and copper compatibility [162]. The moisture absorbing abilities, water weight percentage based on the total weight of the Photo-BCB polymer films, are shown in Table 5.5 [142, 160].

According to the reported studies of BCB based capacitive humidity sensing, soft cured aqueous developable PhotoBCB offered an increase of 17.1% for the moisture solubility, and gave the highest sensitivity of the humidity sensors. Hard cured BCB gave an increase of 40.3% for moisture diffusivity, while giving the fastest sensing response of the humidity sensors. All the comparisons were made based on the reference of hard cured Cyclotene 4024 resin [156]. Both moisture solubility and diffusivity should be considered for the performance of the humidity sensors, which can be compared in terms of their sensitivity as well as their response time. Cyclotene 4024-40 has the advantages of linear moisture sorption isotherms and the large diffusion coefficient for water ($4.5 \pm 0.5 \mu m^2 s^{-1}$ at 23 ℃). Both the physical and behavioural models of transient responses of the capacitive humidity sensors have also been presented, which were supported by finite element method (FEM) simulation as well as experimental validation [120, 121]. A full film oxidation process has also been used. Both the sensitivity and the response time have been improved significantly by complete bulk oxidation of the DVS-BCB / Photo-BCB sensitive film. The device with a film thickness of 3.5 μm successfully showed a sensitivity of 0.19 pF/%RH and a response time of 0.275 second, while simulation results of the sensor with 1.5 μm thick film showed an enhanced sensitivity of 0.39 pF/%RH and a response time of 0.062 second [120].

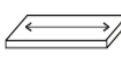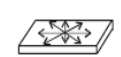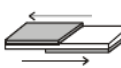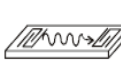## 5.2   Piezoelectric Effect and Lithium Niobate Substrates

A surface acoustic wave (SAW), first explained by Lord Rayleigh in 1885, is a kind of acoustic wave traveling along the surface of a material exhibiting elasticity, whose amplitude typically decays exponentially with depth into the substrate. By using the piezoelectric materials, the transduction from electric energy to mechanical energy is easily accomplished, e.g. piezoelectric materials will be deformed when a voltage is applied [163].

5.2.1   Piezoelectric Effect

The piezoelectric effect, first directly demonstrated by brothers Pierre Curie and Jacques Curie in 1880, is the ability of a material to produce electricity when it is subjected to mechanical stress. This effect also works in reverse, as materials can be deformed slightly when subjected to an applied voltage [164]. Based on the piezoelectric effect, crystal structures of piezoelectric materials bend in different ways, which result in different vibration modes with different vibration frequencies in the range of KHz to

GHz. Table 5.6 shows the vibration modes and the frequencies, which are widely used for sensing applications [165].

Table 5.6 Various vibration modes of different piezoelectric materials [165].

Vibration Mode		Frequency (Hz) 1K 10K 100K 1M 10M 100M 1G	Application
Flexure Vibration		▓▓▓ (1K–100K)	Piezo Buzzer
Lengthwise Vibration		▓ (100K–1M)	KHz Filter
Area Vibration		▓ (1M–10M)	KHz Resonator
Radius Vibration		▓ (1M–10M)	
Thickness Shear Vibration		▓ (10M)	MHz Filter
Thickness Trapped Vibration		▓ (10M–100M)	MHz Resonator
Surface Acoustic Wave		▓ (100M–1G)	SAW Filter SAW Resonator
BGS Wave		▓ (100M–1G)	SH Trap SH Resonator SH Filter

Piezoelectricity is the combined effect of the material's electrical and mechanical behaviour:

$$D = \varepsilon E \qquad (5.1)$$

where D is the electric charge density displacement, ε is permittivity and E is electric field strength.

Meanwhile, according to the Hooke's Law:

$$S = sT \qquad (5.2)$$

where S is strain, s is compliance and T is stress.

Equation (5.1) and (5.2) may be combined into the strain-charge equations:

$$\{S\} = [s^E]\{T\} + [d^t]\{E\} \tag{5.3}$$

$$\{D\} = [d]\{T\} + [\varepsilon^T]\{E\} \tag{5.4}$$

where $[d]$ is the matrix for the direct piezoelectric effect and $[d^t]$ is the matrix for the converse piezoelectric effect. The superscript E indicates a zero or constant electric field, the superscript T indicates a zero or constant stress field, and the superscript t stands for transposition of a matrix.

The strain-charge equations for materials in tetragonal crystal structures or Hexagonal crystal structures may also be written as:

$$\begin{bmatrix} S_1 \\ S_2 \\ S_3 \\ S_4 \\ S_5 \\ S_6 \end{bmatrix} = \begin{bmatrix} s_{11}^E & s_{12}^E & s_{13}^E & 0 & 0 & 0 \\ s_{21}^E & s_{22}^E & s_{23}^E & 0 & 0 & 0 \\ s_{31}^E & s_{32}^E & s_{33}^E & 0 & 0 & 0 \\ 0 & 0 & 0 & s_{44}^E & 0 & 0 \\ 0 & 0 & 0 & 0 & s_{55}^E & 0 \\ 0 & 0 & 0 & 0 & 0 & s_{66}^E = 2(s_{11}^E - s_{12}^E) \end{bmatrix} \begin{bmatrix} T_1 \\ T_2 \\ T_3 \\ T_4 \\ T_5 \\ T_6 \end{bmatrix} + \begin{bmatrix} 0 & 0 & d_{31} \\ 0 & 0 & d_{32} \\ 0 & 0 & d_{33} \\ 0 & d_{24} & 0 \\ d_{15} & 0 & 0 \\ 0 & 0 & 0 \end{bmatrix} \begin{bmatrix} E_1 \\ E_2 \\ E_3 \end{bmatrix} \tag{5.5}$$

$$\begin{bmatrix} D_1 \\ D_2 \\ D_3 \end{bmatrix} = \begin{bmatrix} 0 & 0 & 0 & 0 & d_{15} & 0 \\ 0 & 0 & 0 & d_{24} & 0 & 0 \\ d_{31} & d_{32} & d_{33} & 0 & 0 & 0 \end{bmatrix} \begin{bmatrix} T_1 \\ T_2 \\ T_3 \\ T_4 \\ T_5 \\ T_6 \end{bmatrix} + \begin{bmatrix} \varepsilon_{11} & 0 & 0 \\ 0 & \varepsilon_{22} & 0 \\ 0 & 0 & \varepsilon_{33} \end{bmatrix} \begin{bmatrix} E_1 \\ E_2 \\ E_3 \end{bmatrix} \tag{5.6}$$

where Equation (5.5) represents the relationship for the converse piezoelectric effect and Equation (5.6) represents the case for the direct piezoelectric effect [164, 166].

5.2.2 *Lithium Niobate Substrates*

Among the family of piezoelectic substrate materials, quartz (SiO_2), lithium tantalate ($LiTaO_3$), and lithium niobate ($LiNbO_3$) are most commonly used for acoustic wave sensors and devices. Table 5.7 lists some relevant specifications for each material, including the most popular cuts and orientations. There are also other kinds of piezoelectric materials with commercial potential, including gallium arsenide (GaAs), silicon carbide (SiC), langasite (LGS), zinc oxide (ZnO), aluminum nitride (AlN), lead zirconium titanate (PZT), polyvinylidene fluoride (PVdF), etc. [167].

Table 5.7 Physical parameters of commonly used piezoelectric materials [167].

Material	Orientation	Velocity of SAW (m/s)	Temperature coefficient (ppm/^{o}C)	Attenuation at 1 GHz (dB/μS)
Quartz	Y, X	3159	-24	2.6
Quartz	ST, X	3158	0	3.1
Lithium Tantalate	Y, X	3230	35	1.14
Lithium Tantalate	167 rotation	3394	64	-
Lithium Niobate	Y, Z	3488	94	1.07
Lithium Niobate	128 rotation	3992	75	-

At a higher wave velocity of 3992 m/s, SAW devices fabricated on Lithium Niobate substrates performed at the higher resonating frequencies than other common commercial piezoelectric materials. This results in a higher sensitivity of the SAW based sensors. As one of the most attractive materials, lithium niobate has desirable properties such as piezoelectric, electro-optic, photoelastic, non-linear optic, good mechanical and chemical stability, and wide transparency spectra range. The main properties of lithium niobate are shown in Table 5.8. $LiNbO_3$ has been widely used as frequency doubling material, for Q-switches, waveguide substrates and surface acoustic wave (SAW) devices [168– 171].

Table 5.8 Main properties of lithium niobate [171].

Property	Value	Notes
Optical index or refraction (o-axis)	2.21	At $\lambda=1.55\mu m$
Optical index or refraction (e-axis)	2.14	At $\lambda=1.55\mu m$
RF dielectric coefficient (o-axis)	42.5	$\approx$ constant from 100MHz to 140 GHz
RF dielectric coefficient (e-axis)	26	$\approx$ constant from 100MHz to 140 GHz
RF refractive index (o-axis)	6.5	$\approx$ constant from 100MHz to 140 GHz
RF refractive index (e-axis)	5.1	$\approx$ constant from 100MHz to 140 GHz
Electrical conductivity	1×10^{-18} /Ωcm	At DC
Thermal conductivity	5.6 W/m^{o}C	
Thermal expansion (o-axis)	14×10^{-6} /^{o}C	
Thermal expansion (e-axis)	4×10^{-6} /^{o}C	
Thermal effect on index (o-axis)	1.8×10^{-6} /^{o}C	$\dfrac{1}{n_o}\cdot\dfrac{dn_o}{dT}$
Thermal effect on index (e-axis)	1.60×10^{-6} /^{o}C	$\dfrac{1}{n_e}\cdot\dfrac{dn_e}{dT}$
Melting point	1253 ^{o}C	
Density	4.635 g/cm^3	
Band gap	4 eV	
Electro-optic coefficient	r_{33}=30.8 pm/V r_{13}=30.8 pm/V r_{22}=30.8 pm/V r_{51}=30.8 pm/V	$r_{ij}=\begin{bmatrix} 0 & -r_{22} & r_{13} \\ 0 & r_{22} & r_{13} \\ 0 & 0 & r_{33} \\ 0 & r_{51} & 0 \\ r_{51} & 0 & 0 \\ -r_{22} & 0 & 0 \end{bmatrix}$
Nonlinear electro-optic coefficient	d_{31}=11.6 d_{33}=86 d_{22}=5.6	
Piezoelectric strain coefficient	d_{15}=69.20 pm/V d_{22}=20.80 pm/V d_{31}=-0.85 pm/V d_{33}=6.00 pm/V	$d_{ij}=\begin{bmatrix} 0 & 0 & 0 & 0 & d_{15} & -d_{22} \\ -d_{22} & d_{22} & 0 & d_{15} & 0 & 0 \\ d_{31} & d_{31} & d_{33} & 0 & 0 & 0 \end{bmatrix}$

Normally, lithium niobate can be specified into three grades based on its different applications, acoustic (SAW) grade, refractive grade, and optical grade. Acoustic grade is the most commonly produced grade for making SAW based devices, and is also the least demanding in terms of impurities and crystalline perfection because of its non-optical applications. The crystals are grown over quite a long time, converting a large fraction of the melt into crystalline material [168, 170].

Regular lithium niobate is strongly pyroelectric. The surface of regular lithium niobate substrates may accumulate electric charge when substrates are heated or cooled during the soft bake and hard bake steps during the UV photolithography process. This may cause spontaneous electrical discharge between dense metalized lines on the substrate, such as the IDTs of SAW devices, as well as electrical discharge between the substrate and the metal plate used for heating or cooling. This discharge effect makes the regular lithium niobate substrates difficult for wafer handling and processing, and may cause the substrate to be damaged. Meanwhile, the wide transparency spectra range of regular lithium niobate may also bring yield effects including multi-reflection and scattering in the UV photolithography process.

Chemical reduction, at elevated temperatures in an environment of nitrogen and hydrogen, produces chemically reduced lithium niobate (black lithium niobate) material which has an increased electric conductivity, of the order of 10^4, and effectively eliminates pyroelectric sparking. At the same time, the optical absorption is increased significantly causing its appearance to become gray to dark black and almost non-transparent, which has a positive impact on the photolithography process. A picture of the black lithium niobate wafers is shown in Fig. 5.3, the advantages of which include:

- Good ability to neutralise electrical charges even if the applied electrical potential occurs instantaneously;
- No difference in piezoelectric properties from regular lithium niobate wafers;
- High uniformity of bulk resistivity in the surface and bulk of wafers.

The typical properties of black lithium niobate wafers are shown in Table 5.9 [172-176].

Table 5.9 Typical properties of lithium niobate wafers [172-176].

	Black lithium niobate	Regular lithium niobate
Bulk Resistivity ($\Omega \cdot$ cm)	2.40E+11	3.80E+14
Bulk Conductivity ($\Omega^{-1} \cdot$cm^{-1})	4.17E-11	2.63E-15
Surface Electric Potential[*] /100mmφ(kV)	<0.05	3.05
Electrical Charge neutralisation (sec)	1.5	∞
Optical Transmission%[#]	<60	73
Colour	Dark Grey	Colourless
Lithium Niobate 127.86 $^\circ$Y-cut		
	Black lithium niobate	Regular lithium niobate
Curie temperature Tc ($^\circ$C)	1132$\pm$2	1132$\pm$2
SAW velocity	Unchanged	3980
Coupling coefficient k^2	Unchanged	5.5

[*] Electrical charges due to temperature rising from room temperature to 95°C at 4-inch wafer
[#] 0.35mm thickness wafer (with both sides mirror polished) measured by 365nm wavelength
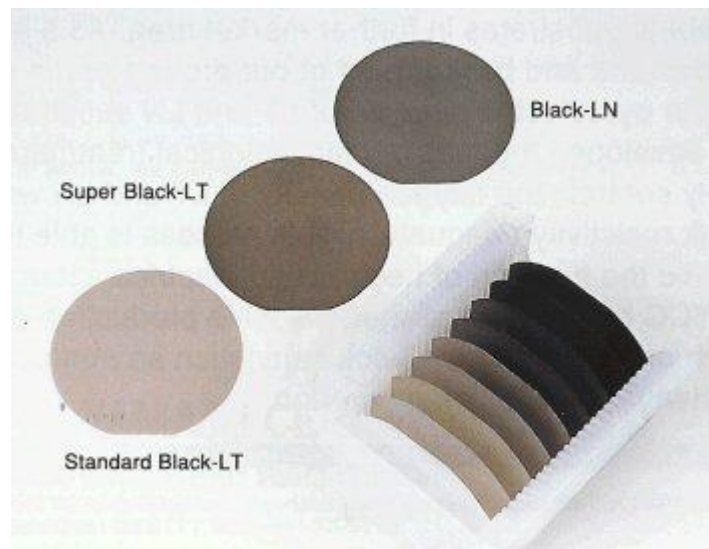
Figure 5.3 Picture of black lithium niobate wafers [176].

5.3 Polymer Assisted SAW Humidity Sensing

A single port SAW device could act as a resonator based on its reflection signal. The simplified equivalent circuit of such a device is shown in Fig. 5.4. L_m and C_m would resonate at the resonance frequency of the SAW device, while the series resistance R_m is related with the losses for the SAW device. L_m, C_m and R_m are dynamic parameters, which are determined by the properties of the fabricated SAW device. C_o is the static capacitance between the end electrodes and is equal to $C_p+C_g/2$, while $C_g=C_{g1}=C_{g2}=0.5pF$ normally. Two port SAW devices normally act as resonators based on their transmission signal, the simplified equivalent circuit of such a device is shown in Fig. 5.5. Here, the definition of L_m, C_m, R_m and C_o are as already defined above for Fig. 5.4 [177].
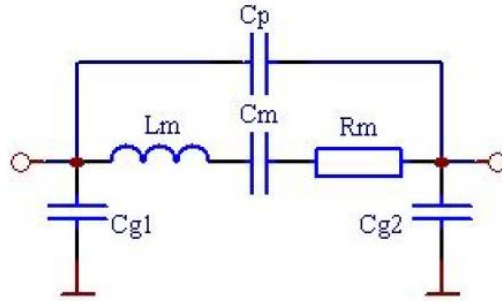
Figure 5.4 Equivalent circuit of single port SAW resonator [177].
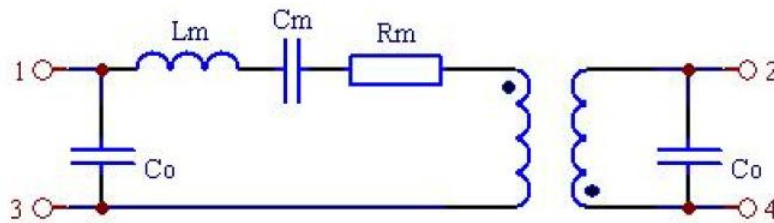
Figure 5.5 Equivalent circuit of two port SAW resonator [177].

Polyimide, fluoropolyol (FPOL), polyvinyl-alcohol (PVA) and benzocyclobutene (BCB) [120-122], all absorb the moisture in the air, which causes an increase in the density, mass, permittivity, and electric conductivity of the polymer films. All these factors tend to decrease the velocity of the SAW [178]. The main mechanism is a change in mass loading, which changes the phase velocity in the SAW device, which results in a frequency shift. Equation (5.7) shows the relationship between the frequency shift (Δf) and the change in mass per unit area (Δm), where C_s is a constant dependent

on the properties of the piezoelectric substrate of the SAW device and f_0 is the resonance frequency of the SAW device [179-181].

$$\Delta f = -C_s f_0^2 \Delta m \qquad (5.7)$$

Meanwhile, the amplitude of the SAW resonant signal would change with the amount of energy dissipated into the medium contacting the device surface. The physical properties of coated polymers which act as the surface contacting medium would also be changed on absorbing moisture, resulting in amplitude changes. These changes are reflected in the insertion loss, which is defined as the ratio of the output signal amplitude to that of the input, in decibels. The total energy loss across the device includes transduction losses, propagation losses (occurring as the waves travel through the piezoelectric material of the device), and additional losses from dissipation of energy in the medium contacting the device surface [179].

The behaviour modelling of the SAW device has already been studied using several methods, including the impulse response method, the conventional matrix approach and the modified matrix approach. As a baseline for modelling the SAW device, the impulse response method is valid only for transducers where at least one of the two IDTs has a constant aperture or finger overlap. This modelling approach includes both mechanical and electrical behaviour of SAW devices, including frequency response, the loss of the system, the admittance, and the parameters for circuit simulators. Constant equal spacing and finger width are normally assumed. The conventional matrix method is based on transmission line theory. The SAW device is modelled as two IDTs with two ports for mechanical waves travelling into and out of the IDT when current and voltage are on the IDTs. The matrix for SAW delay line is simply the multiplication of the matrices for the two IDTs and a matrix for the delay in between. The complete SAW device matrix normally is given by:

$$[SAW(f)] = [T_1(f)D(f)T_2(f)] \qquad (5.8)$$

where f is the frequency, $T_1(f)$ and $T_2(f)$ are the transmission matrices for each IDT which can be cascaded easily, and $D(f)$ stands for the delay matrix [182-184].

Based on both the impulse response method and the conventional matrix approach, the model has been extended by including second order elements. In this approach, The model divides an IDT into half wavelength sections, which are further divided into zones. Two of the zones are un-metalized areas (1/8 of a wavelength) around one zone that is comprised of a metal finger (1/4 of a wavelength). While each zone is modelled by a transmission line matrix, the SAW delay line matrix is simply the multiplication of the matrices for the two IDTs and the delay or space between the IDTs [182, 183].

The power consumption analysis of the SAW sensor system was reported in 2006, modelled using the software of ANSYS and PSPICE [185]. There are several design parameters of the SAW sensor, including the distance between two IDTs, thickness of piezoelectric substrate and finger space of IDT. All of these could significantly affect the power consumption of the full sensing system. The simulated results show that the total power consumption increases as the centre distance between each IDT increases. The reason for this is that more power will be lost during transporting from one IDT to another with increasing the centre distance. The study of the power consumption caused by different thickness of the piezoelectric substrates shows that there is no variation in the transverse direction along the surface and that the particles move both in the direction of wave propagation and perpendicular to the depth of substrate, while the surface waves propagate along the surface and decay into the bulk material within a distance of the order of a wavelength. These simulation results demonstrate that the maximum wave amplitude occurs at $1/4\lambda$ thickness due to the interference from the back surface of the substrate, which corresponds to the maximum power of SAW transportation. The value of the finger space will also affect the total system power consumption, which also determines the resonance frequency of the SAW sensor. The simulation results show that the power consumption decreases as the resonance frequency increases. This also means reducing the distance between two adjacent fingers within the single IDT, the limit of which depends on the resolution of the lithography fabrication process [185-188].

5.4   Design and Fabrication of SAW Based Sensors

To achieve the transduction from electrical energy to mechanical energy, SAW based devices are normally designed and fabricated by patterning metal IDTs on piezoelectric substrates in arrays of single or pair of IDTs. SAW devices have been in commercial use for more than 60 years for applications in filters, oscillators, transformers, as well as

applications in sensing and microfluidics. A schematic picture of a typical SAW device design is shown in Fig. 5.6 [167].
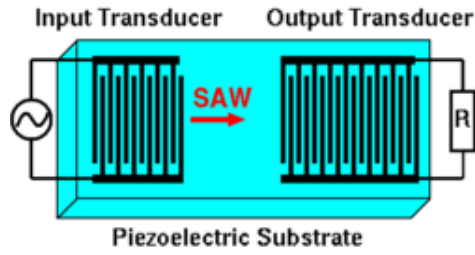

Figure 5.6 Schematic picture of a typical SAW device design [167].

The width of the individual IDT was designed to be the same dimension as the gaps between the IDTs, both of which are a quarter of the wavelength of the SAW resonator. For example, the wavelength of the SAW resonator was 16 µm while the width of the individual IDT was designed as 4 µm. This yields a resonance frequency of about 249.50 MHz, when the SAW velocity is 3992 m/s based on the Equation (5.9), where f is the resonance frequency, v is the wave velocity, and λ is the wavelength. The number of IDTs in each transducer determines the power of the wave generated, while longer IDTs provide more uniformity on the wave travelling direction. A normalized metal thickness range for the IDTs was designed from 0.4% to 4% of the wavelength [189].

$$f = \frac{v}{\lambda}$$
(5.9)

The reflection grating structures have also been considered for enhancing the amplitude of the resonance. The maximum reflectivity of a shorted grating (shown in Fig. 5.7a) is slightly higher than that of an open grating (shown in Fig. 5.7b) [189].

(a)

(b)
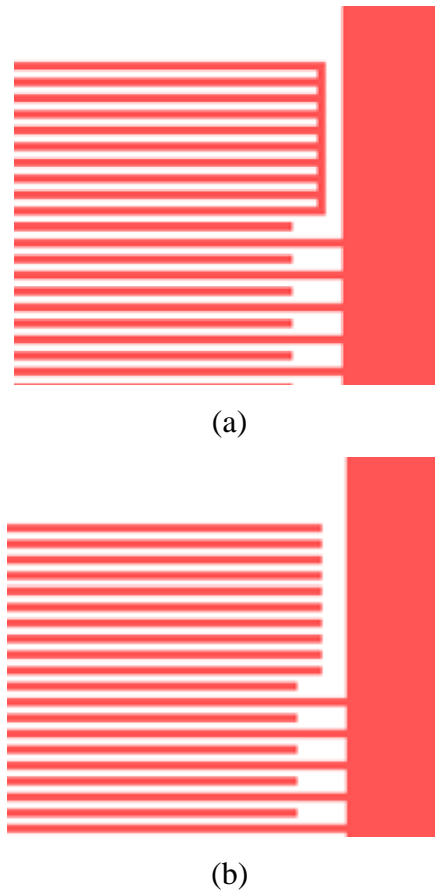
Figure 5.7 SAW transducer with (a) shorted grating reflector, (b) open grating reflector.

A 5-inch photomask was designed using the design software L-Edit (Tanner Research, Inc.). the mask was produced by Delta Mask (Netherlands) with patterned Cr film on a soda lime glass substrate. The layout of the mask, exported from the L-Edit file, is shown in Fig. 5.8, which includes 4 single and 9 dual SAW resonators. The SAW resonators were designed with IDTs widths of 4, 8, and 16 μm, and lengths of 2.9, 3.9 and 4.9 mm with distances between the SAW transducers of 1.5, 2, 3, 4, and 5 mm being used. The reflection grating structures were also included in the mask design. More detailed information of the photomask design is shown in Table 5.10 and 5.11.
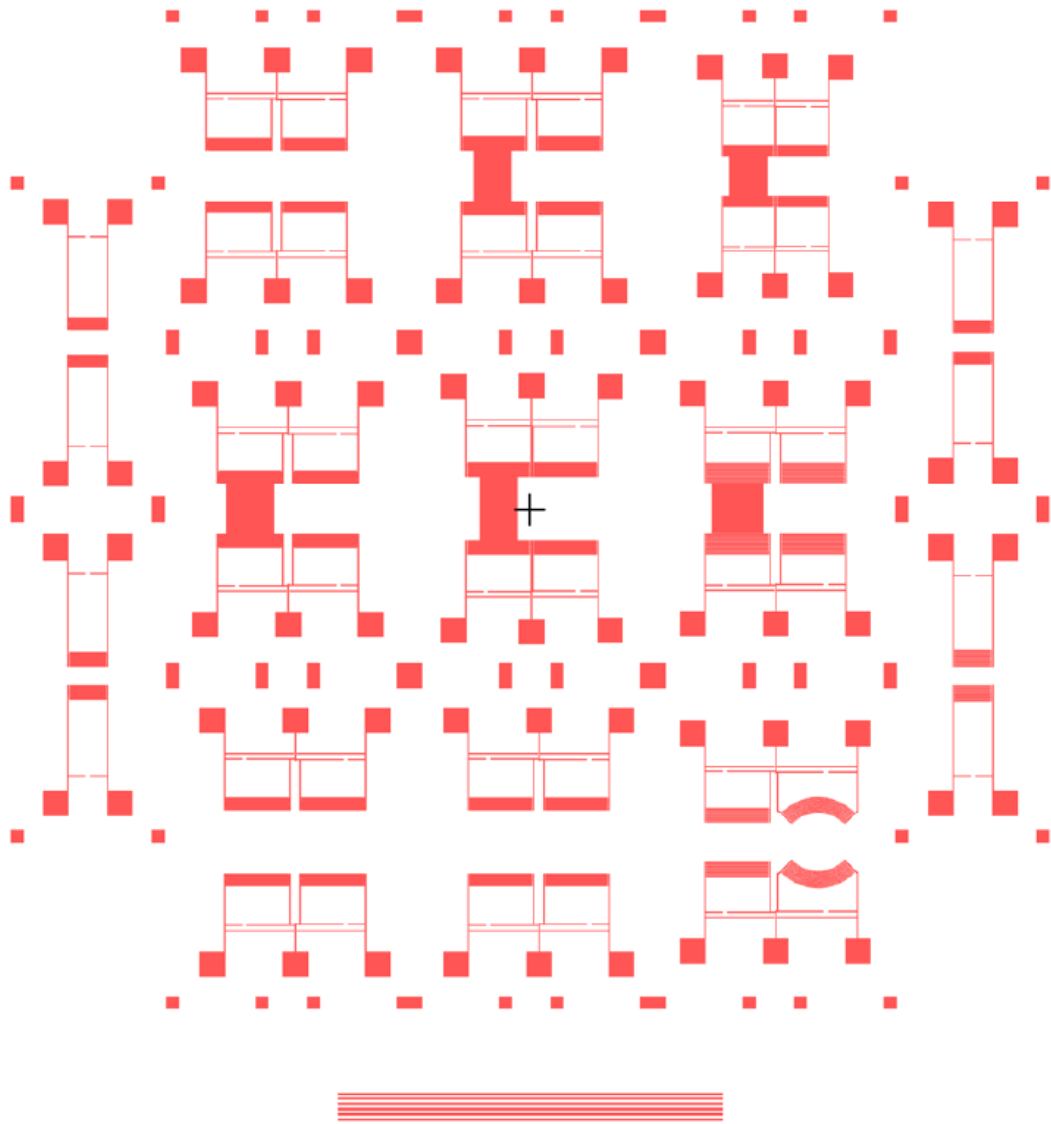
Figure 5.8 Layout of the photomask for SAW devices fabrication.

Table 5.10 Schematic layout of the SAW photomask design.

	D1	D4	D7	
S1				S3
	D2	D5	D8	
S2				S4
	D3	D6	D9	

Table 5.11 Details of the SAW photomask design.

	IDT width	IDT length	IDT No.	Central Gap	Reflector
S1	4 μm	2.9mm	60	2mm	No
S2	8 μm	2.9mm	30	1.5mm	Yes
S3	8 μm	2.9mm	30	1.5mm	No
S4	16 μm	2.9mm	20	1.5mm	No
D1	4 μm	4.9mm	60	4mm	No
	4 μm	4.9mm	30	4mm	No
D2	4 μm	4.9mm	60	4mm	Yes
	4 μm	4.9mm	60	4mm	Yes
D3	4 μm	4.9mm	60	5mm	No
	4 μm	4.9mm	60	5mm	No
D4	8 μm	4.9mm	30	4mm	Yes
	8 μm	4.9mm	30	4mm	Yes
D5	8 μm	4.9mm	30	5mm	Yes
	8 μm	4.9mm	30	5mm	Yes
D6	8 μm	4.9mm	30	5mm	No
	8 μm	4.9mm	30	5mm	No
D7	8 μm	3.9mm	30	3mm	No
	8 μm	3.9mm	30	3mm	No
D8	16 μm	4.9mm	20	4mm	Yes
	16 μm	4.9mm	20	4mm	Yes
D9	16 μm	4.9mm	20	3mm	No
	16 μm	2.825 mm	20	3mm	No

Fabrication of the SAW based sensors was carried out on both regular lithium niobate (white LiNbO$_3$) and chemically reduced lithium niobate (black LiNbO$_3$) substrates. Aluminum of thickness 300 nm was sputtered as the metal layer, which was patterned using an aluminum etchant at $45 \pm 2^{\circ}$C to form the IDT structures following UV photolithography and development of the mask pattern. The composition of aluminum etchant is shown in Table 5.12. The SAW based sensors were successfully fabricated (Fig. 5.9). Characterisation studies of the fabricated SAW sensors were carried out using Zygo interferometer (Zygo Corporation, USA), and the results of one of the fabricated SAW sensors with IDT width of 16 μm are shown in Fig. 5.10.
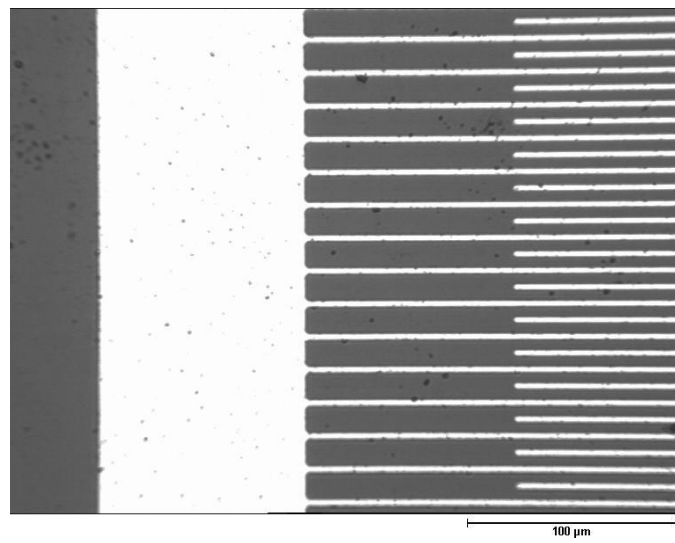
(a)
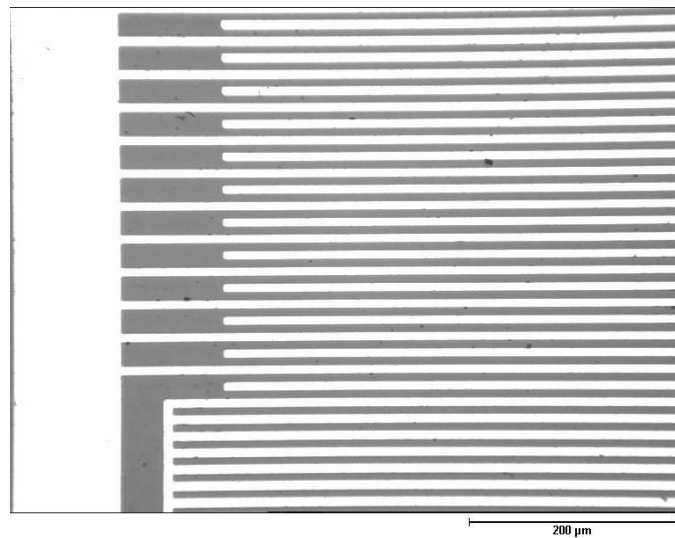
(b)

Figure 5.9 Fabricated SAW sensors

(a) with IDTs width of 4 μm on black LiNbO$_3$ substrate;

(b) with IDTs width of 8 μm and shorted grating reflector on regular LiNbO$_3$ substrate.

93

Table 5.12 Composition of aluminum etchant.

Solution	Ratio by volume
H_3PO_4	16
HNO_3	1
CH_3COOH	1
H_2O	2
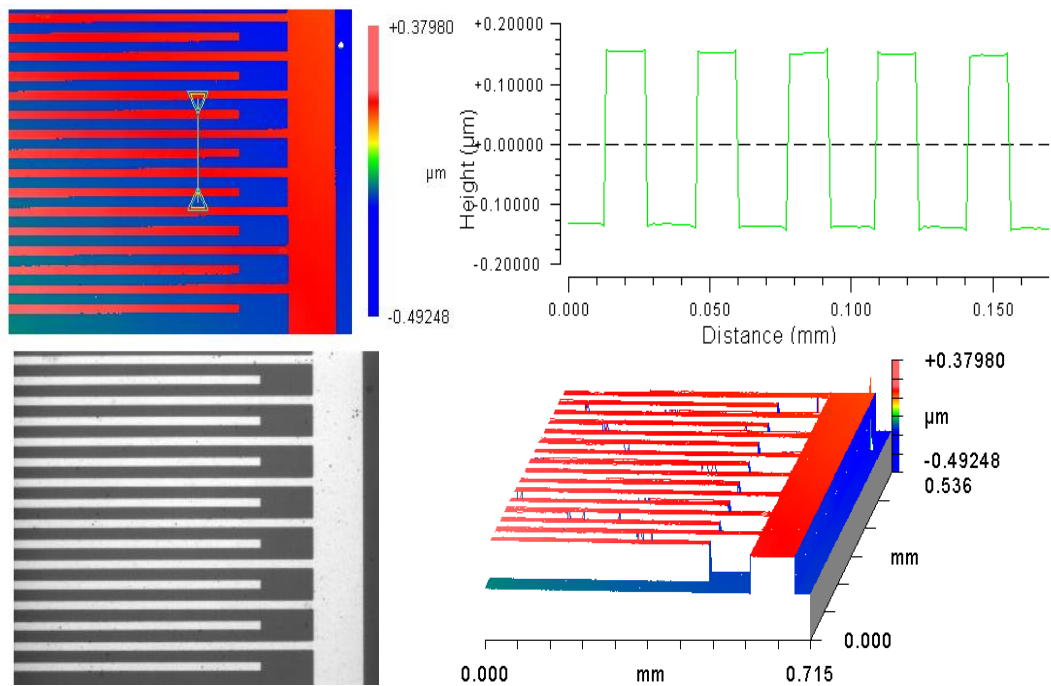
Figure 5.10 Test results of SAW sensor obtained using a Zygo interferometer.

5.5   Testing of SAW Based Sensors

The contact pads of the SAW sensors were designed with dimensions of 1 mm $\times$ 1 mm. A HP 8510 network analyzer, shown in Fig. 5.11, was used to measure the transmission and reflection signals of the fabricated SAW sensors. SMA connectors (Tyco Electronics Corporation, USA), shown in Fig. 5.12, have been used to connect the SAW sensors to the HP 8510 network analyzer for measurement. The description details of these connections are shown in Table 5.13 [190].

Figure 5.11 HP 8510 network analyzer.

Figure 5.12 SMA connector from Tyco Electronics Corporation [190].

Table 5.13 Description of SMA connector from Tyco Electronics Corporation [190].

Connector type	SMA Coaxial
Impedance	50R
Contact material	Brass
Contact plating	Gold
Body style	Straight socket
Termination method	Solder
Mounting type	PC board
Material	Stainless Steel
Insulator Material	PTFE
Number of mating cycles	500
Contact resistance	3mR
Insulation Resistance	500MR
Operating temperature	- 65 to 165 ℃
Voltage rating	AC 500V
Max operating frequency	18 GHz

Two different contacts between SAW pads and SMA connectors have been designed and used for characterisation of SAW sensors. For the first design, shown in Fig. 5.13, the SAW sensor has been attached on a wire board, and connected to copper wires soldered with silver loaded epoxy (RS Components Ltd, UK). The Ag/epoxy is used for repairing electrical connections and general conductive bonding applications. The ground connections were achieved through the metal layer at the back side of the wire board. The resistivity of the cured silver loaded epoxy compound is less than 0.005 ohm cm [191]. As shown in Fig. 5.14, a test stage has also been well designed and fabricated by the university mechanical workshop. The SAW sensor has been placed on the test stage with 3M test clips (3M United Kingdom plc, UK) for connecting between the contact pads and the SMA connectors [192]. The ground connections were achieved using soldered wire.

During measurements, there was no observed difference between the wire board and the test clip setups. The test clip connection was used for the characterisation of the SAW device before the BCB layer was coated and patterned. The Ag loaded epoxy based connection has been used for characterisation of SAW devices after the BCB layer was coated and patterned for humidity sensing. This is because the BCB polymer cannot be properly spin coated after the epoxy contact was made, which results in a non-flat surface.

(a)

(b)

(c)
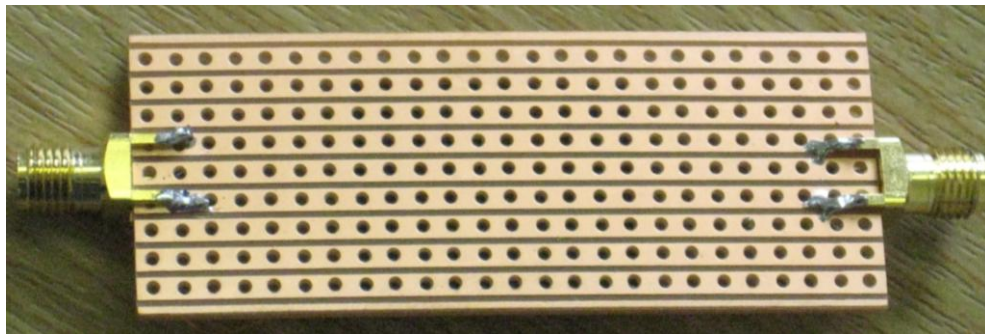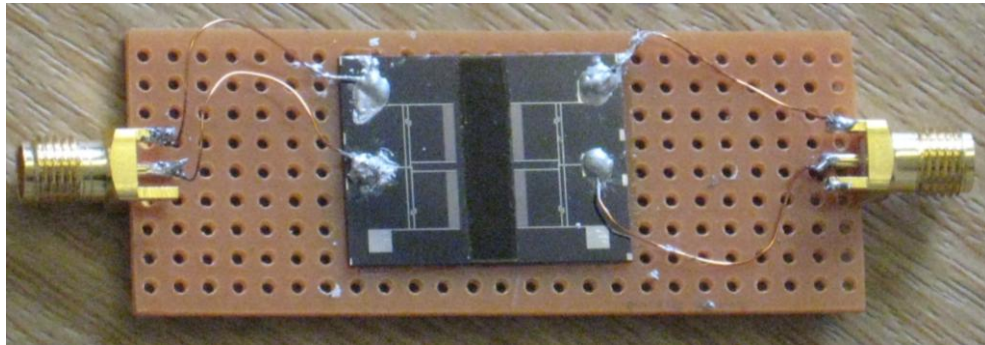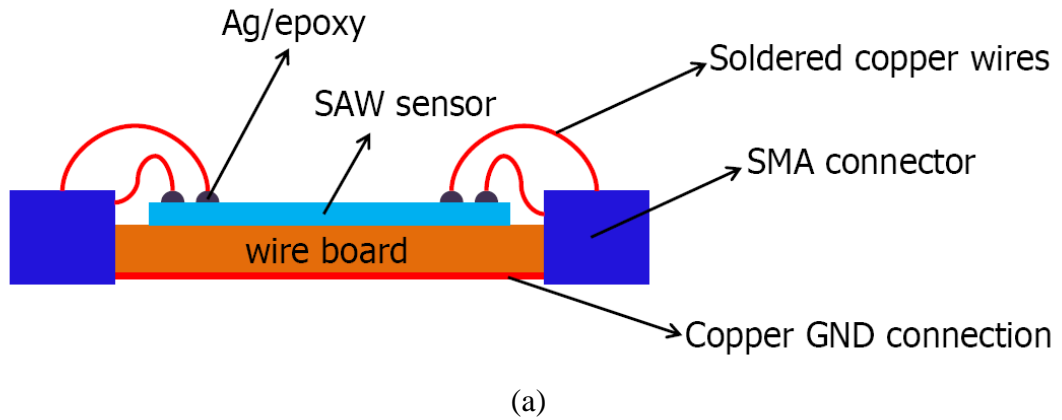
Figure 5.13 Test setup with wire board and Ag/epoxy connection (a) schematic setup; (b) top view; and (c) bottom view.
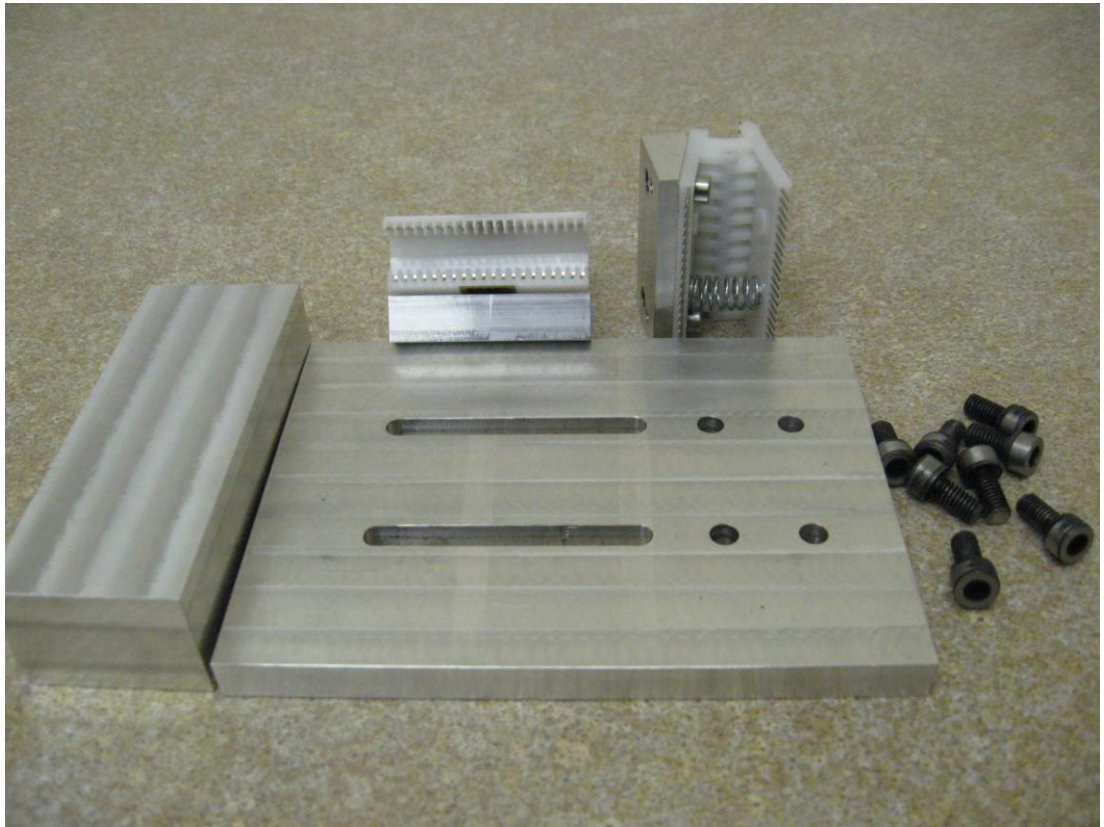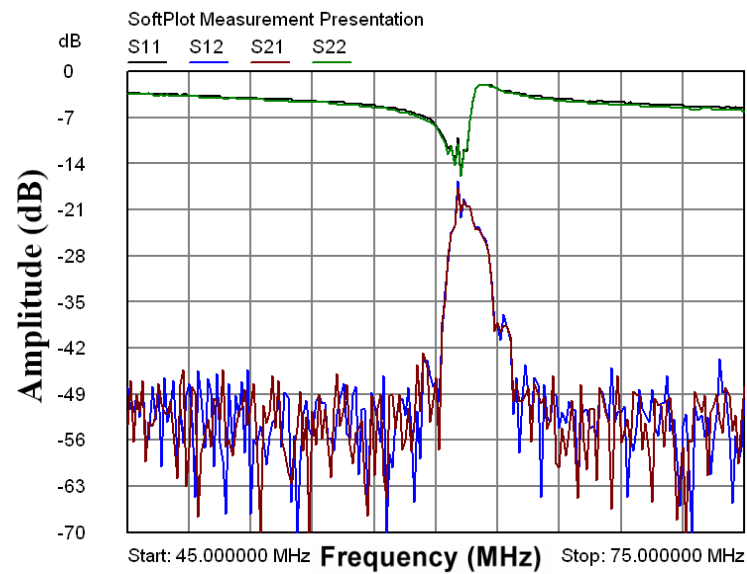
(a)
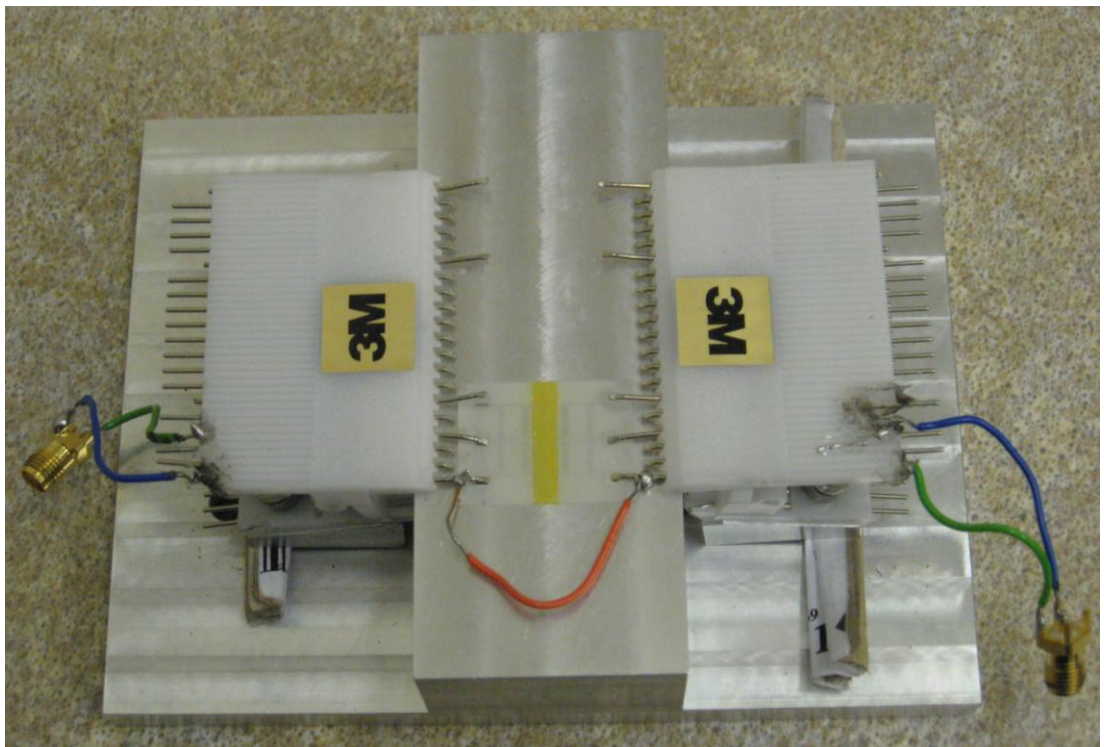
(b)

Figure 5.14 Test setup with 3M test clips (a) before assembly and (b) after assembly

with SMA connectors.
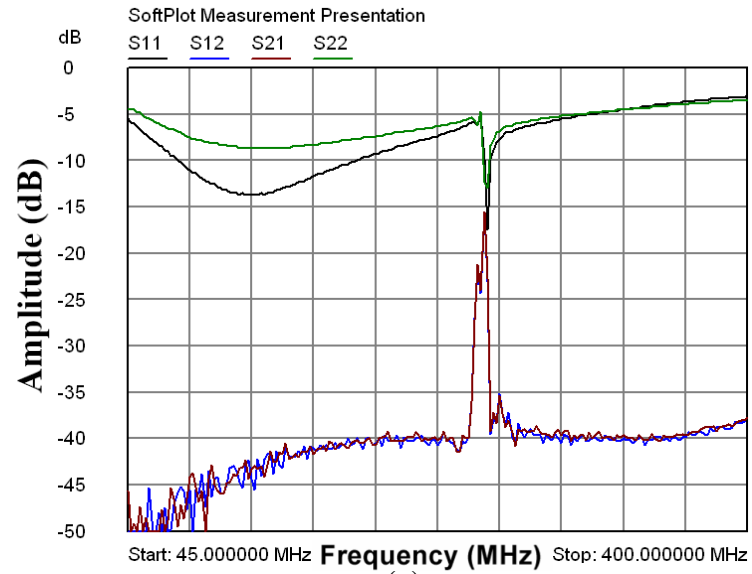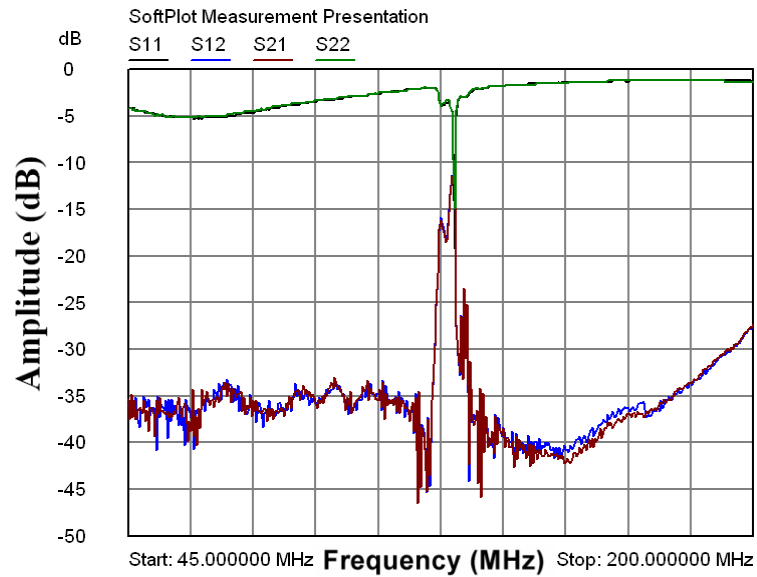
Figure 5.15 Test results of SAW sensors with IDTs widths at (a) 4 μm, (b) 8 μm, and (c) 16 μm before the fabrication of BCB films.

Before spin coating of the BCB films, the test results of SAW sensors on regular LiNbO$_3$ substrates with IDTs widths at 4, 8, and 16 μm are shown in Fig. 5.15, with S11 & S22 corresponding to the reflection signals and S12 & S21 corresponding to the transmission signals. The resonance frequencies of the fabricated SAW devices were measured as 248.60, 124.82, and 62.38 MHz, respectively, while the theoretical values are 249.50, 124.75, and 62.19 MHz based on Equation (5.9) (with SAW velocity of 3992 m/s for 128 ° cut LiNbO$_3$ substrates). A comparison of SAW sensors fabricated on regular and chemically reduced LiNbO$_3$ substrates are shown in Fig. 5.16. The resonance frequencies were the same for the sensors on both substrates.
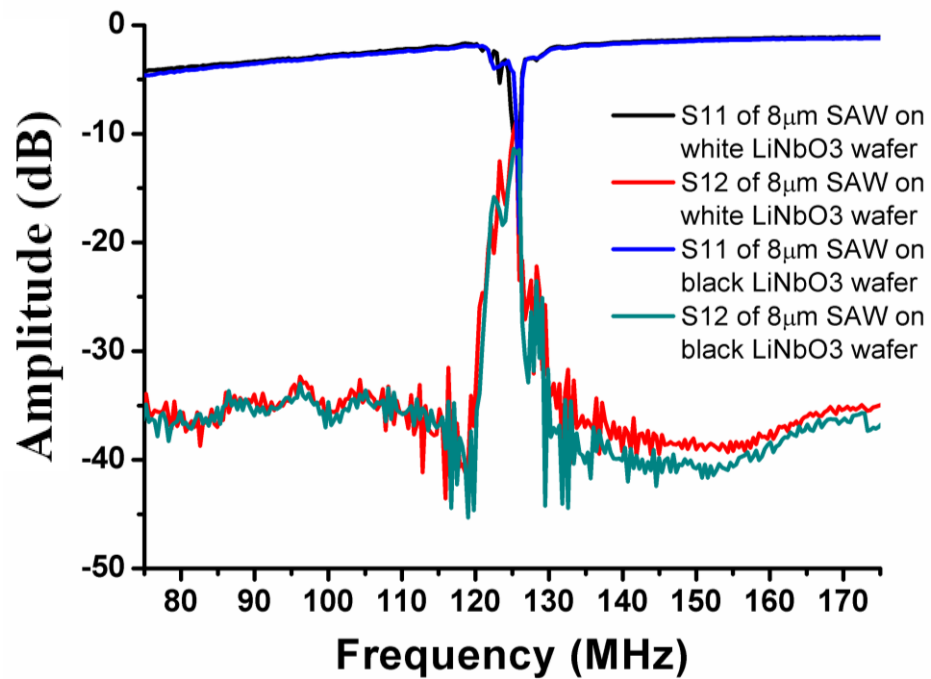

Figure 5.16 Comparison of SAW sensors based on different substrates.

Quality factor (Q factor) is a dimensionless parameter which describes how under-damped an oscillator or resonator is, or equivalently, characterizes a resonator's bandwidth relative to its centre frequency [193]. Fig. 5.17 shows the Q factor as defined by Equation (5.10),

$$Q = \frac{f}{\Delta f}$$

(5.10)

where f is the resonance frequency of the SAW sensor and Δf is the -3dB bandwidth [194]. The enhancement of Q factor by the reflection grating structures has also been studied with fabricated SAW sensors with IDT widths of 8 μm on regular LiNbO$_3$ substrates. The test results are shown in Fig. 5.18. The measured Q factor of the sensor with reflection grating structures was 740, which was about 27.4% higher than the sensor without reflection grating structures, which had a Q factor of 581.
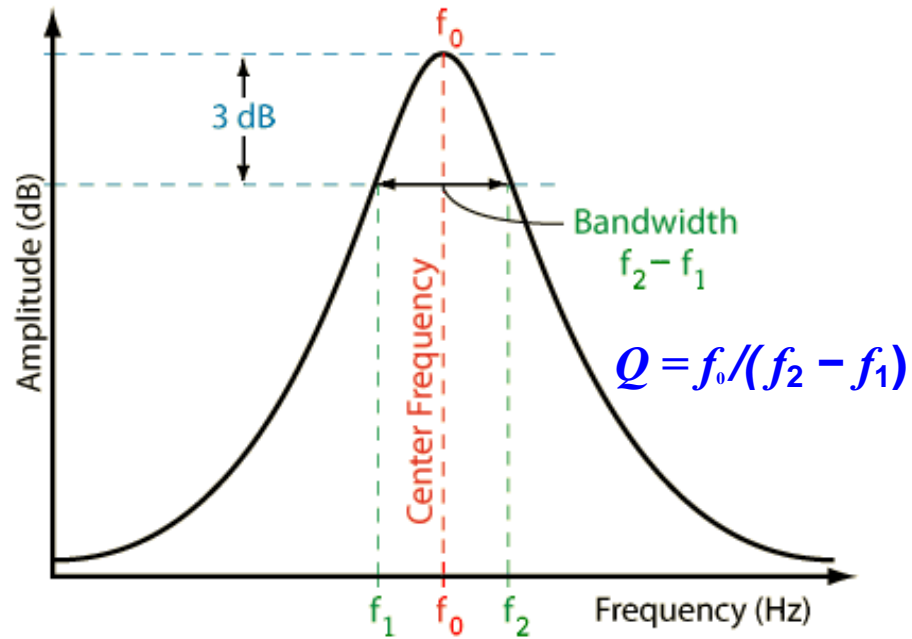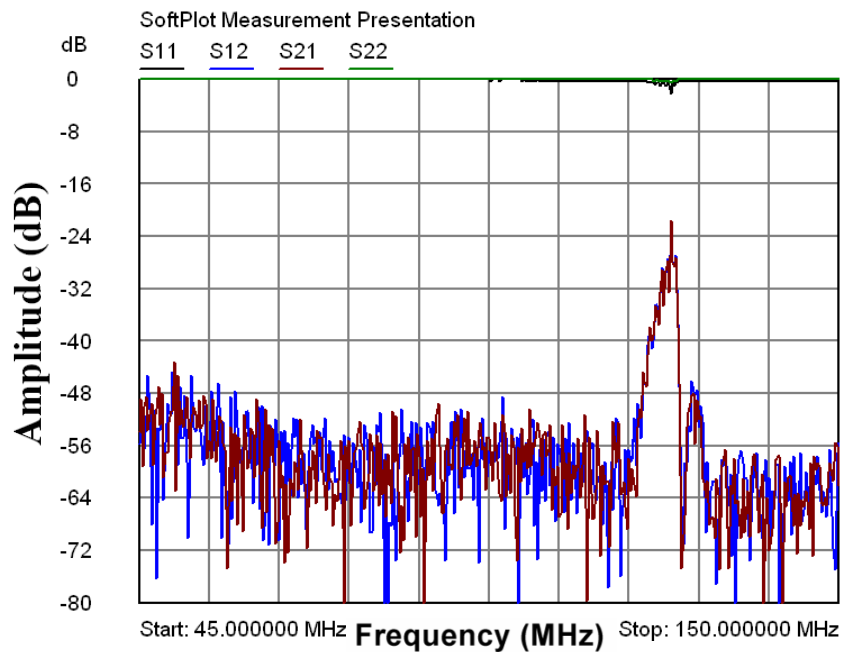

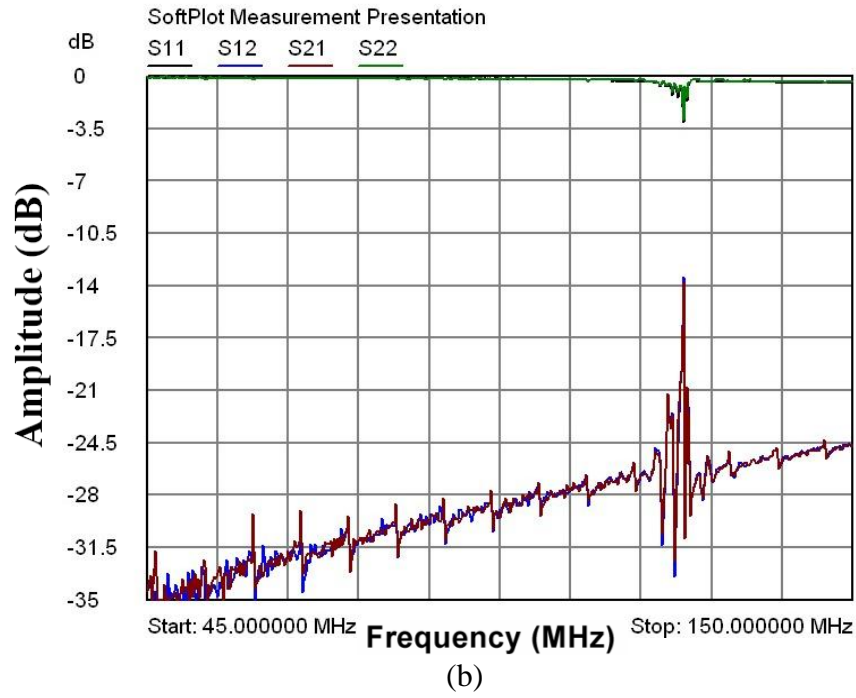Figure 5.17 Definition of Q factor of SAW sensors [194].

(a)

(b)

Figure 5.18 Comparison of SAW sensors (a) without and (b) with reflection gratings.

5.6   Temperature Dependence of Fabricated SAW Sensors

The measured normalized temperature coefficient of the ultrasonic velocities of lithium niobate were reported to be in the range from -2.035 to -0.684 $\times 10^{-4}$ / °C, which means that the resonance frequency of the SAW sensor with IDT widths of 16 μm, 62.19 MHz, may have shifted from 4.2 to 12.6 kHz with a temperature change of 1 °C [195]. It has also been reported that the SAW sensors based on chemically reduced lithium niobate substrates have worse temperature stability than the sensors fabricated on regular lithium niobate substrates, especially when the temperature is above 300 °C [196].

Fabricated on the regular lithium niobate substrate, a SAW sensor with an IDT width of 16 μm has been used for an experimental study of the temperature stability of the SAW devices. The testing stage used for temperature stability measurement is shown in Fig. 5.19. A hot plate has been used to heat up the SAW sensor and the substrate temperature was measured by a commercial thermocouple with a sensitivity of 0.1 °C. As shown in Fig. 5.20, the measured temperature dependence of the resonance frequency is about 4.26 KHz/°C in the temperature range between 24.7 and 80.1 °C. Meanwhile, the monitoring of resonance amplitude shifts versus temperature changes has also been carried out by using the same SAW sensor. The results in Fig. 5.21 show that the thermal effect of resonance amplitude is negligible in temperature range between 24.7 and 80.1 °C. This indicates that the SAW devices for humidity sensing are

102

stable and reliable using the monitoring resonance amplitude changes in the temperature range between 24.7 and 80.1 ℃
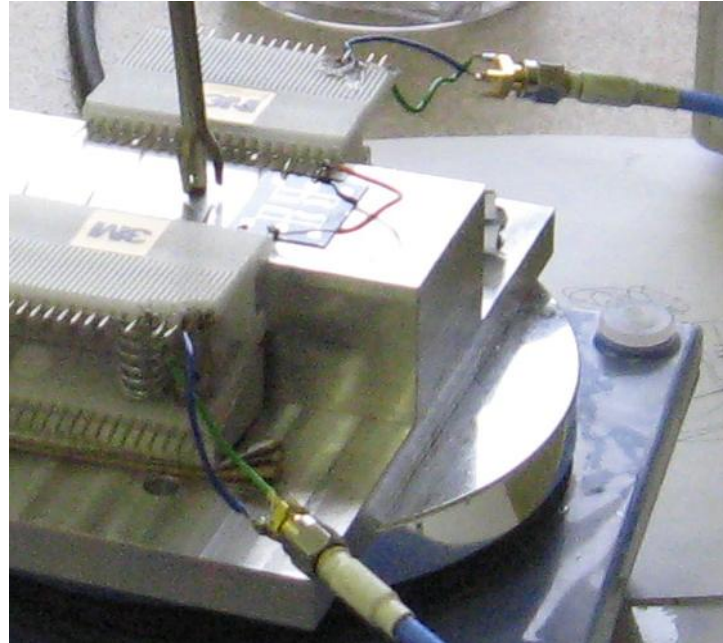

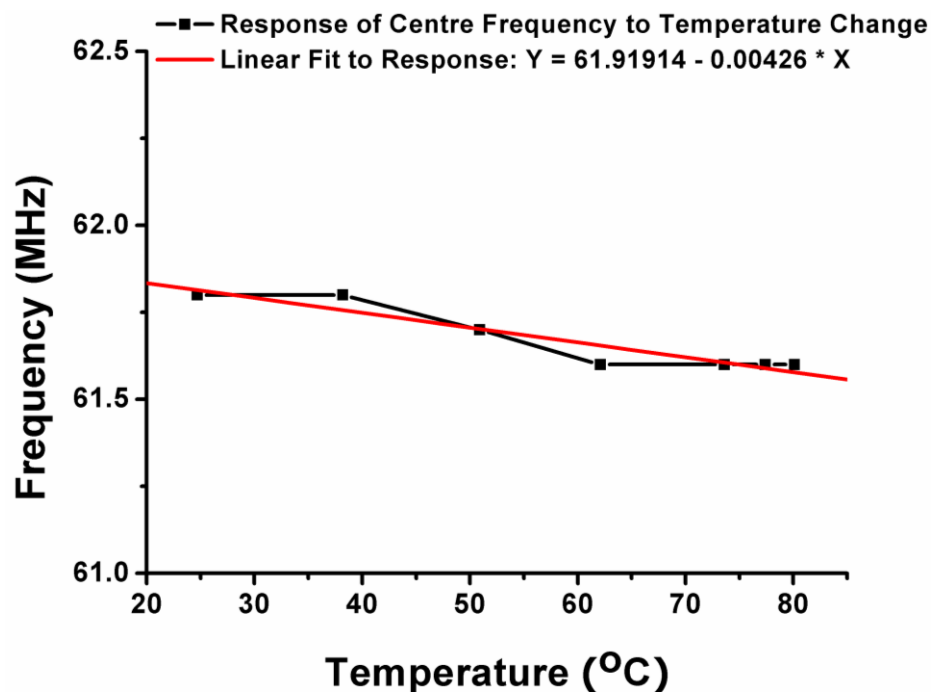Figure 5.19 Testing setup of temperature stability of SAW sensor.

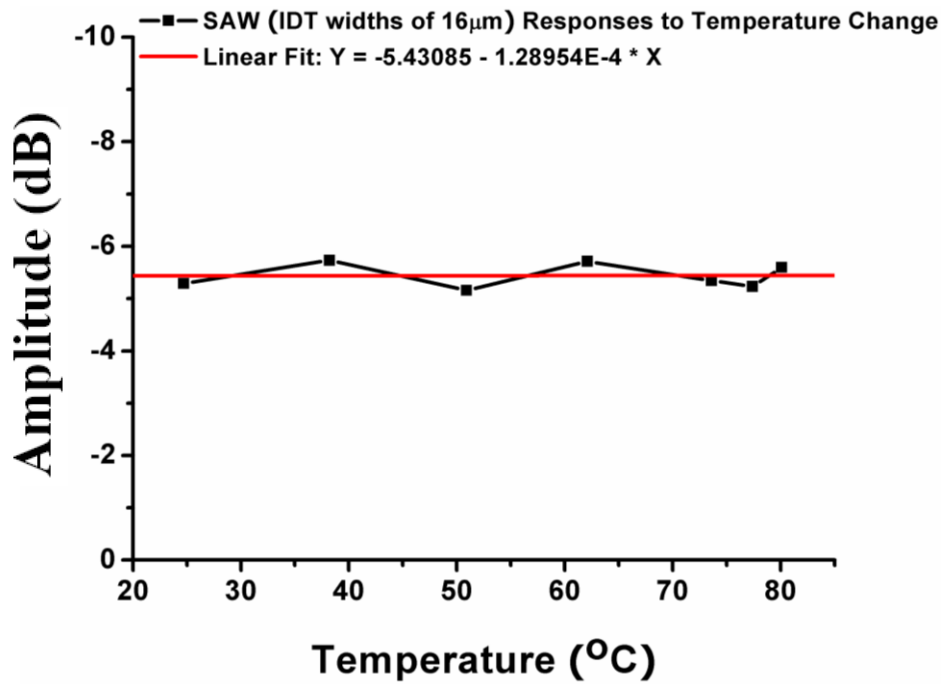
Figure 5.20 SAW resonance frequency versus temperature.

Figure 5.21 SAW resonance amplitude versus temperature.

5.7 BCB Film Based SAW Sensors for Humidity Detection

Following investigation on the IDT dimensions, substrates materials, reflection grating structures, and SAW temperature reliability, a BCB film (CYCLOTENE 4026-46) was coated on a SAW resonator sensor with IDT width of 8 μm for qualitative humidity sensing testing. The SAW sensor was fabricated on a regular $LiNbO_3$ substrate and designed without the reflection grating structures. The details of the spin coating process were: 500 rpm with acceleration of 100 r/s for 20 seconds, and then 3500 rpm with acceleration of 500 r/s for 100 seconds. A soft bake was carried out at 90 ℃ for 120 seconds after the spin coating process. The film thickness was confirmed using the Zygo interferometer. A uniform BCB film with thickness of 8.4 μm was obtained successfully. The schematic setup for the qualitative humidity sensing test is shown in Fig. 5.22.
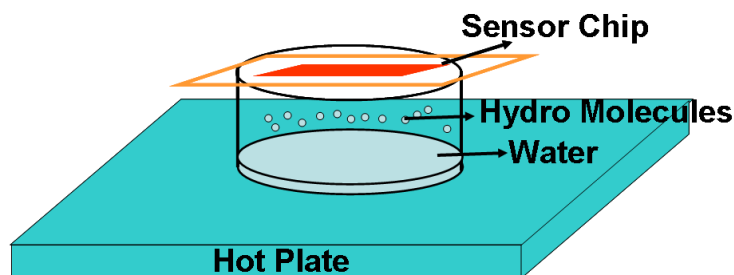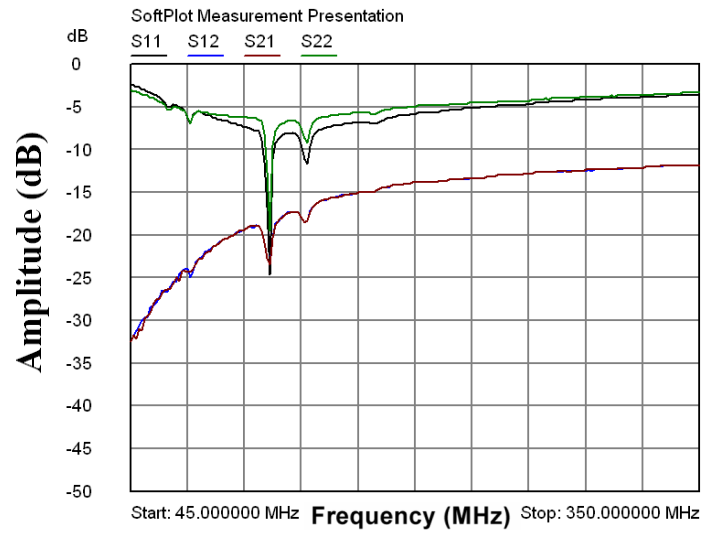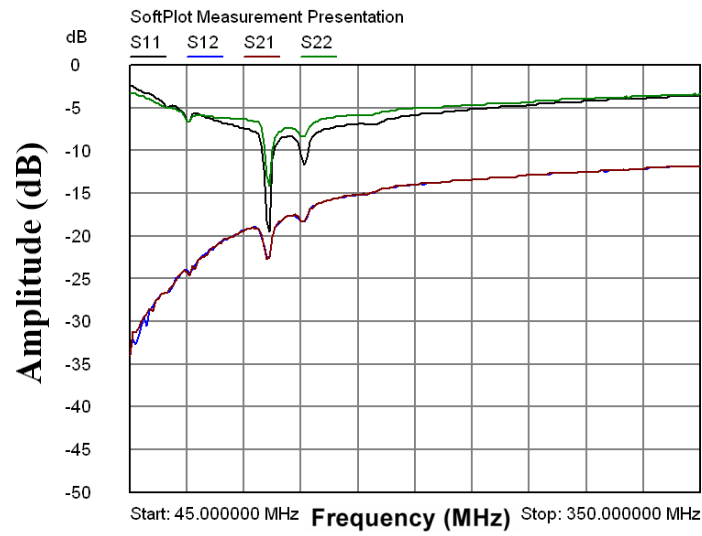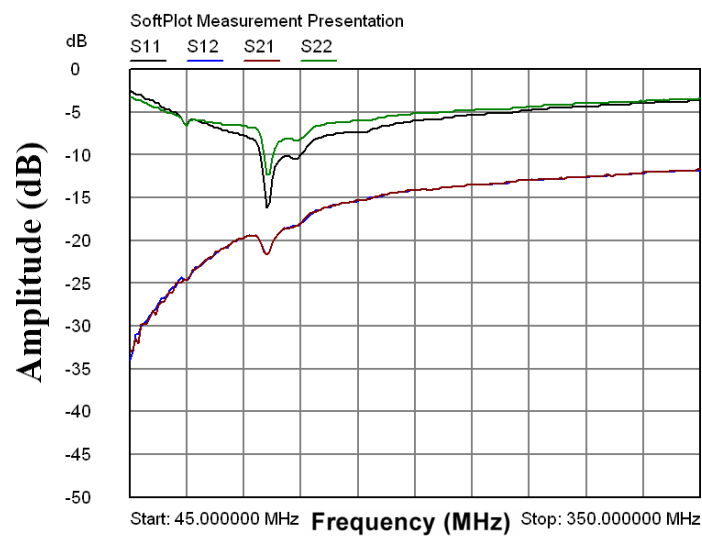

Figure 5.22 Schematic setup for the qualitative humidity sensing test.

(a)

(b)

(c)

Figure 5.23 Responses of qualitative humidity sensing test with BCB film based SAW

sensor at (a) Room RH level, (b) Middle RH level, and (c) High RH level.

The humidity levels were adjusted by controlling the temperature of the hot plate, resulting in changes of the saturated water vapour pressure at different temperatures. The results of the qualitative test, obtained using a HP8510 Network Analyzer, are shown in Fig. 5.23. As summarised in Fig. 5.24, an amplitude shift of reflection signals was recorded based on the humidity change. The transmission signals were totally lost, which was because the cover of BCB film at the aperture between the SAW transducers blocked the wave propagation while the reflex gain was enhanced significantly.
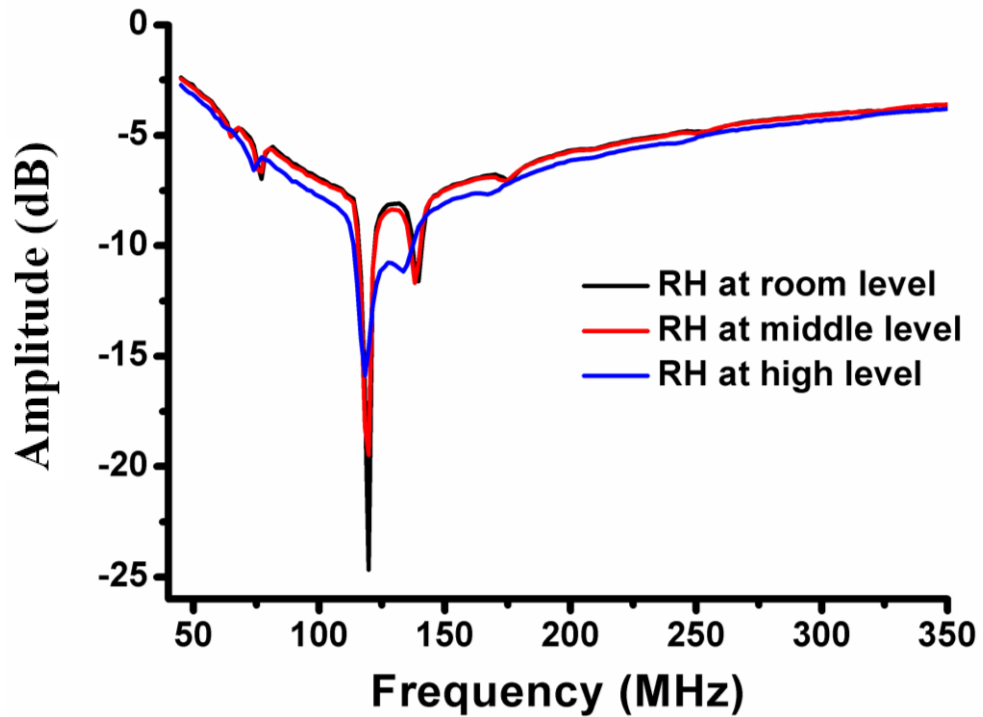
Figure 5.24 Qualitative test results with respect to the RH change.

A humidity controlled system was subsequently designed for the quantitative measurement of SAW based humidity sensors using BCB sensing films. The design and test set up are shown in Fig. 5.25. The quantitative BCB film based SAW humidity sensing tests were carried out at RH levels controlled by dry/wet nitrogen flow and monitored by a humidity probemeter (N18FR Maplin Electronics Ltd, UK). SAW resonator sensors with IDT widths of 8 μm, fabricated on regular LiNbO3 substrate and designed with reflection grating structures, have been used for this quantitative humidity monitoring.
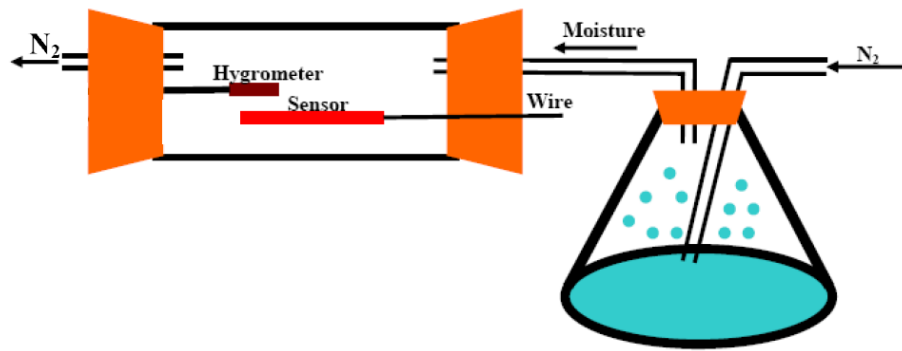
(a)
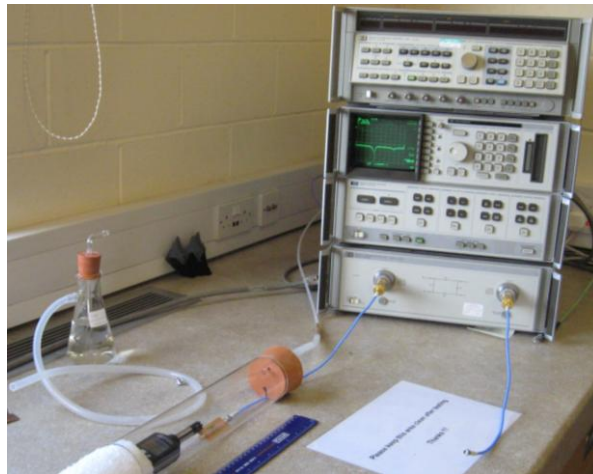
(b)
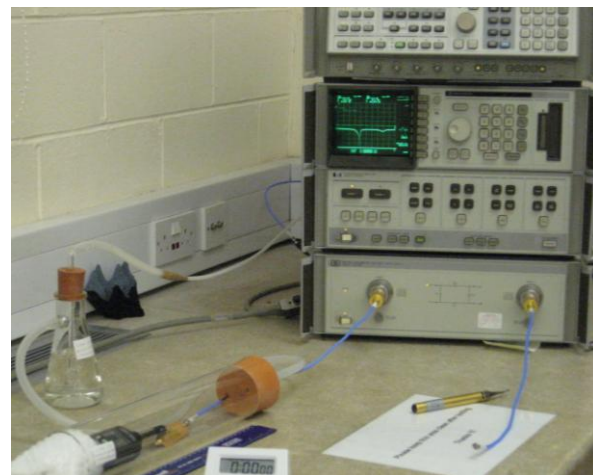
(c)

Figure 5.25 Test setup for the quantitative humidity sensing detection (a) Schematic diagram of the test set up, (b) RH level below room environment controlled using a dry N_2, and (c) RH level above room environment controlled using a wet N_2.

The BCB film was produced by spin coating at 500 rpm with acceleration at 100 r/s for 20 seconds, and then 5000 rpm with acceleration of 500 r/s for 150 seconds. A soft bake was carried out at 80 °C for 120 seconds after the spin coating process. Using a Zygo

interferometer, the BCB film thickness was measured to be 7.0 μm. At a humidity range of 0% to 100% RH, an accuracy of ±3.5% RH, and a resolution of 0.1% RH, the humidity probe meter (Maplin Electronics Ltd, UK) showed stable and controllable humidity levels were achievable below 10% RH using a dry N_2 flow and above 90% RH using a wet N_2 flow (Fig. 5.26). Using the test setup as shown in Fig. 5.25, the reflection responses at each stable RH point from 8.6% to 91.7% RH were recorded and are shown in Fig. 5.27. The amplitude shifts of the reflection responses are displayed in Fig. 5.28. Using the BCB film as the moisture absorbing layer, the test results followed a linear relation, and with 7.0 μm thick BCB film as the moisture absorbing layer, the sensitivity of the fabricated SAW sensor was about 0.26 dB/RH% monitored using reflection signals.

(a)

(b)

Figure 5.26 Humidity probe reading while humidity level was at
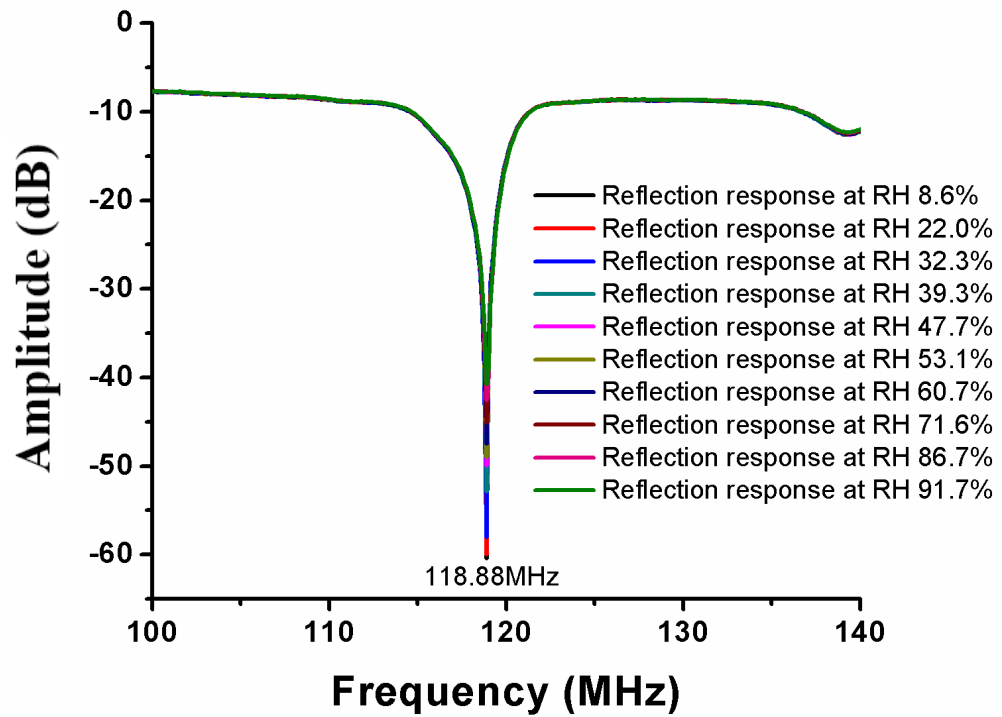
(a) 8.7% and (b) 90.6%.

108

Figure 5.27 Reflection responses to the humidity changes

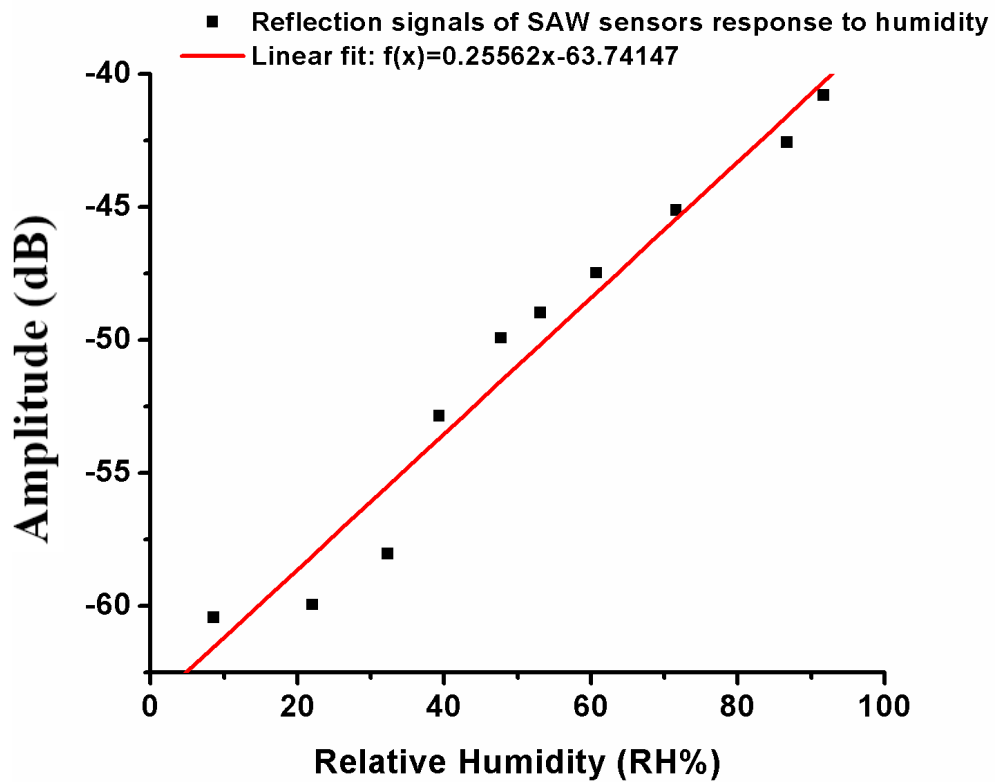monitored by 7.0 μm BCB film based SAW sensor.

Figure 5.28 Amplitude shifts of the reflection responses based on the humidity changes.

5.8   Summary

The properties of the BCB films, for humidity sensing application, have been summarized. Both regular and chemically reduced lithium niobate piezoelectric substrates for SAW sensors have been studied. The performances of both types were observed to be the same for both the resonance frequency and amplitude. The SAW velocity of the 128 ° cut lithium niobate substrates is about 3992 m/s, which has been selected for the fabrication of the BCB film based SAW sensors for humidity detection. After a theoretical study of SAW resonators, a soda lime glass based photomask was designed and fabricated with IDT designs at widths of 4, 8, and 16 μm. The sensors were fabricated on both regular and chemically reduced lithium niobate substrates with sputtered aluminium as the metal IDT. The aluminium was patterned using a wet etching method. Two types of connections, silver loaded epoxy and test clips, showed no difference with respect to SAW resonance testing.

Successfully fabricated sensors with different IDT widths have been used for: (1) investigation of the IDT dimension effects; (2) substrates effects; (3) enhancement of reflection grating structures; and (4) the temperature dependence. Resonance signals from the SAW sensors were monitored using a HP 8510 network analyzer. The measured resonance frequencies of the fabricated SAW sensors were 248.60, 124.82, and 61.20 MHz for designs of IDT widths of 4, 8, and 16 μm respectively. Resonance frequencies were the same for the sensors on both regular and chemically reduced $LiNbO_3$ substrates. Slight difference of the amplitudes was observed. Devices on the chemically reduced $LiNbO_3$ substrates offered lower amplitudes compared to those on the regular $LiNbO_3$ substrates. Test results also showed that the Q factor of a SAW sensor with IDT width at 8 μm was increased by 27.4%, from 581 to 740, by the application of shorted reflection grating structures. A shift of resonance frequency with temperature was measured as 4.26 KHz/ °C using a fabricated SAW sensor with IDT width of 16 μm. This value is almost at the minimum value of the thermal stability according to references [195, 196]. SAW sensors with different IDT widths have been used for the investigation, because of limited number of devices available.

Qualitative humidity sensing tests were carried out with a BCB film of thickness of 8.4 μm. A significant amplitude change of the reflection signals was recorded based on the humidity change. Quantitative humidity sensing detection was subsequently performed

with a SAW sensor coated with the BCB film of thickness of 7.0 μm. Humidity levels were achieved between 8.6% and 90.6% RH by adjusting the dry/wet nitrogen flow. The test results show a linear relationship between humidity and frequency. Based on the reflection signals, a sensitivity of 0.26 dB/RH% was demonstrated.

Chapter 6   Methods for Sensor Integration

After the design, fabrication and testing of the metal thin film based temperature sensors and the BCB film based SAW humidity sensors, assembly of piezoresistive pressure sensors on $LiNbO_3$ substrates was developed to look at sensor integration. Pressure sensors with different operating range (0 to 1.5 bar and 0 to 7 bar) have been selected for the sensor integration work. The final stage of integration combines the temperature, humidity, and pressure sensors on a single substrate for embedded health monitoring in Microsystem. Integrated multi-sensors were designed on both $LiNbO_3$ and ZnO/Si substrates and were successfully fabricated on the $LiNbO_3$ substrate.

6.1   Piezoresistive Pressure Sensor

Based on the piezoresistive effect discussed in ***Section 2.3.3.2***, P+ type highly doped peizoresistors can be fabricated on a Si membrane as shown in Fig. 6.1. The advantages of this structure include fabrication with standard MEMS processes, easily controlled time and energy for ion implantation, and output with DC signal. With either vacuum or a constant pressure in the sealed cavity, changes in outside pressure result in piezoresistive changes, which are monitored using a Wheatstone bridge DC test circuit.
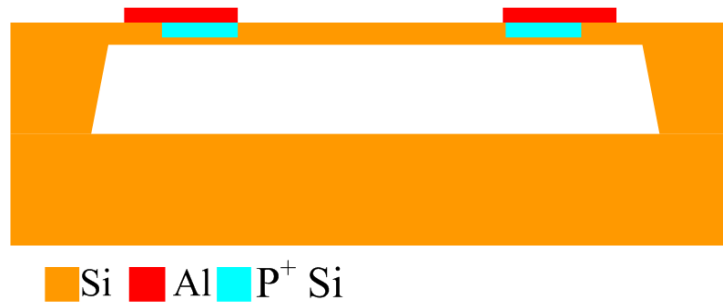
Figure 6.1 Schematic cross section of piezoresistive pressure sensor
based on Si – Si bonding.

As shown in Fig. 6.2, the silicon based piezoresistive pressure sensors incorporate a boron implantation region used to create the sensing piezoresistors. High concentration boron diffusion doped P-wells are used to form the good Ohmic contacts to Al patterned contact pads. By simplifying the photolithography process, an optimised implantation process flow shown in Fig. 6.3, has been used for the fabrication of prototype piezoresistive pressure sensors. Both the boron implantation and the high concentration

boron diffusion have been achieved in one step using a SiO$_2$ mask layer in thickness of 200 nm [197].
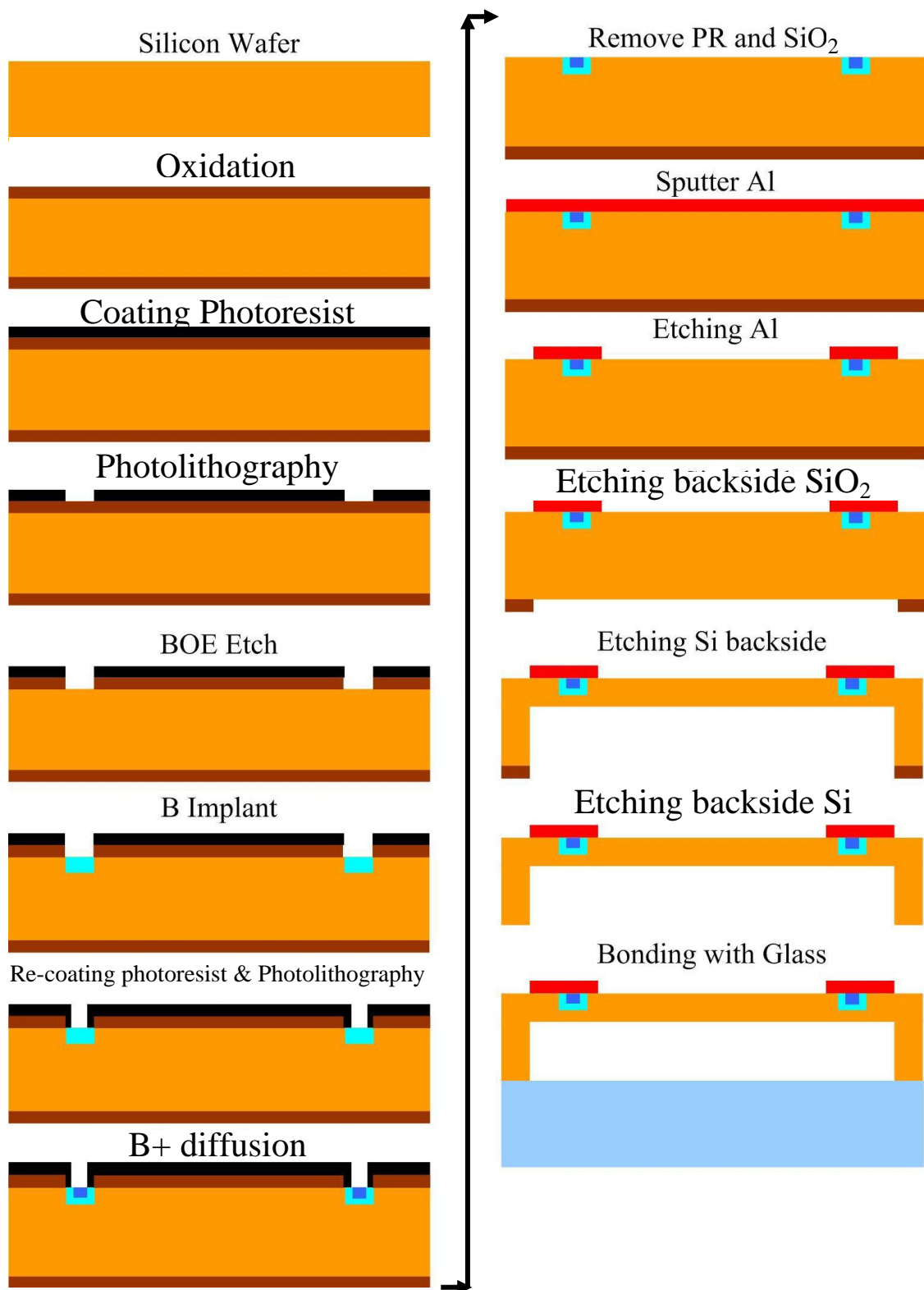
Figure 6.2 Process flow of Si based pizoresistive pressure sensor based on Si – Glass bonding [197].
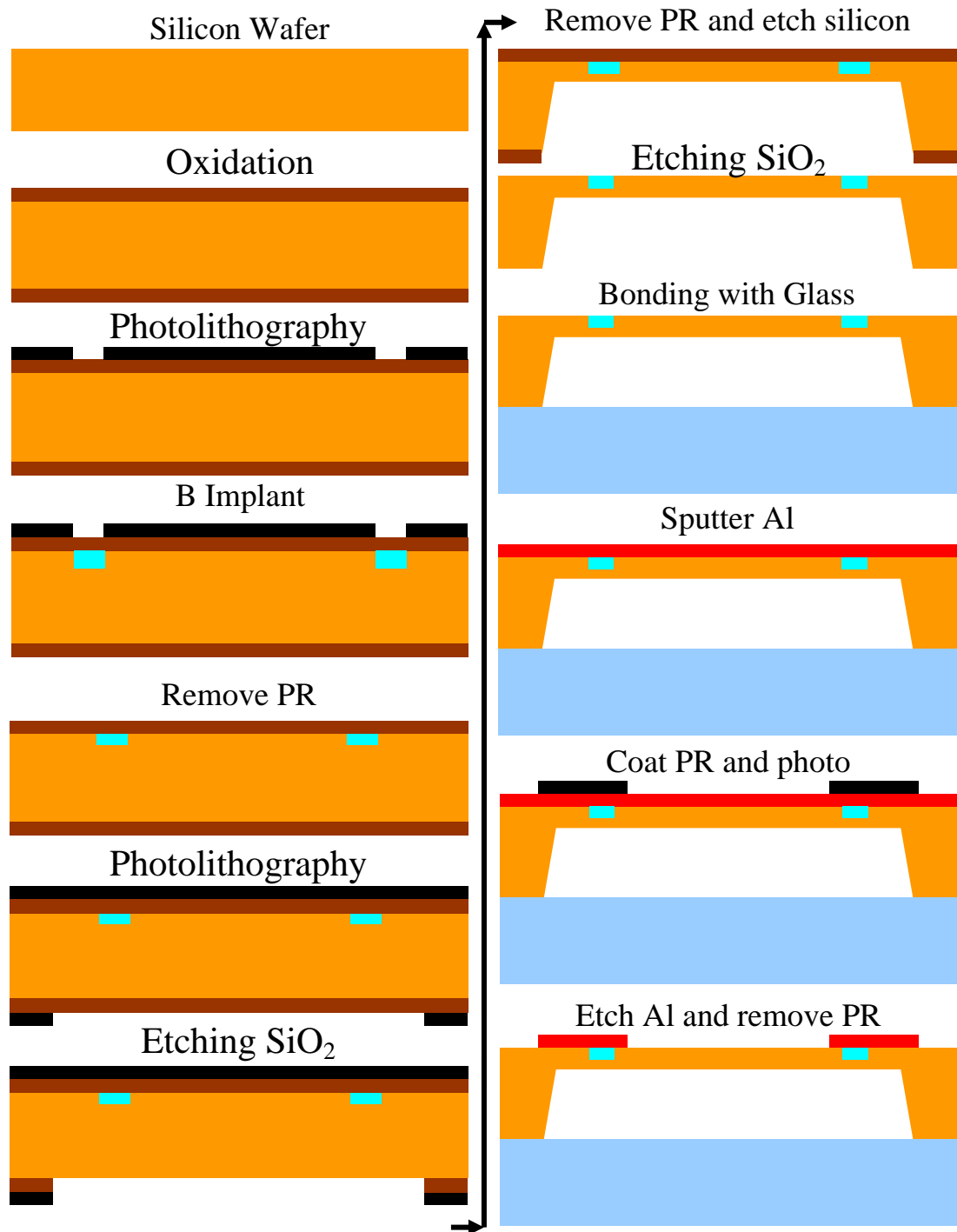
Figure 6.3 Optimised process flow of boron implantation [197].

To create piezoresistive sensing structures using the optimised implantation process, AZ6112 photoresist was first spin coated onto the wafer after oxidation. During the UV photolithography process, the wafer was soft baked at 90°C for 120 seconds and hard baked at 120°C for 120 seconds. The energy for the boron ion implantation was 60 keV, which formed the sensing piezoresistive layer with doping concentration of 7.5×10^{14}/cm^3. An Ohmic contact layer containing larger doping concentration of about

$10^{19}/cm^3$ was also formed at the interface underneath the 200 nm thick SiO_2 mask layer. After ion implantation, an annealing process was carried out at temperature of $950\,^oC$ in a dry nitrogen environment for 40 minutes [197]. The pressure sensors were provided by Shanghai Institute of Microsystem and Information Technology (SIMIT), China.
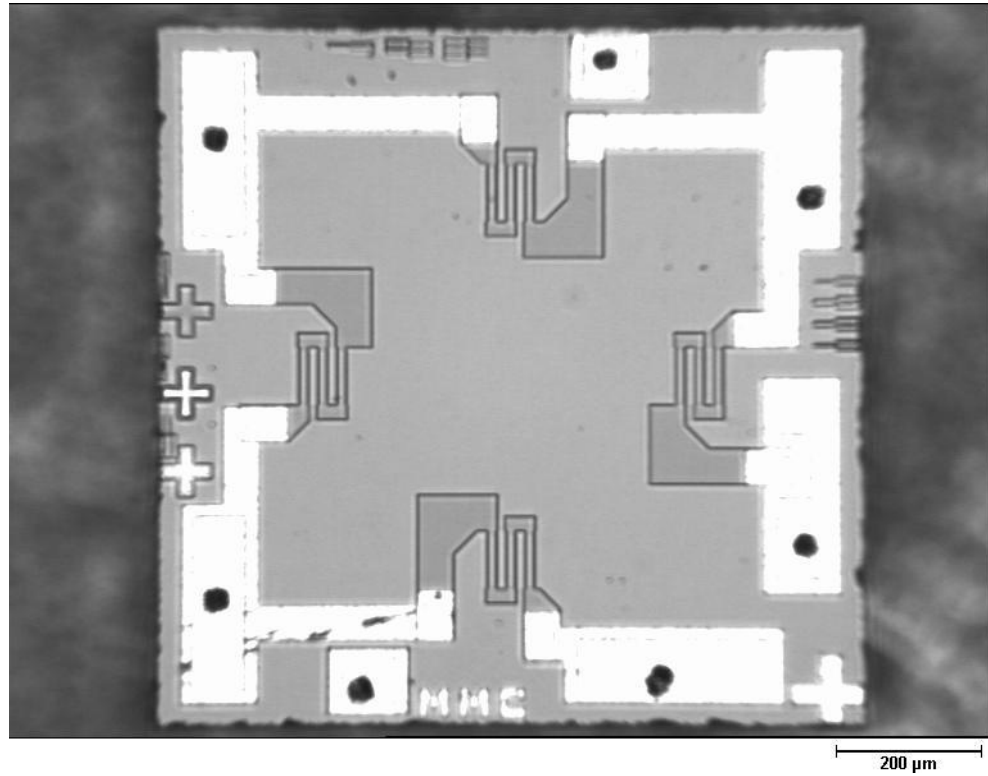
Figure 6.4 Top view of the fabricated prototype piezoresistive pressure sensor.
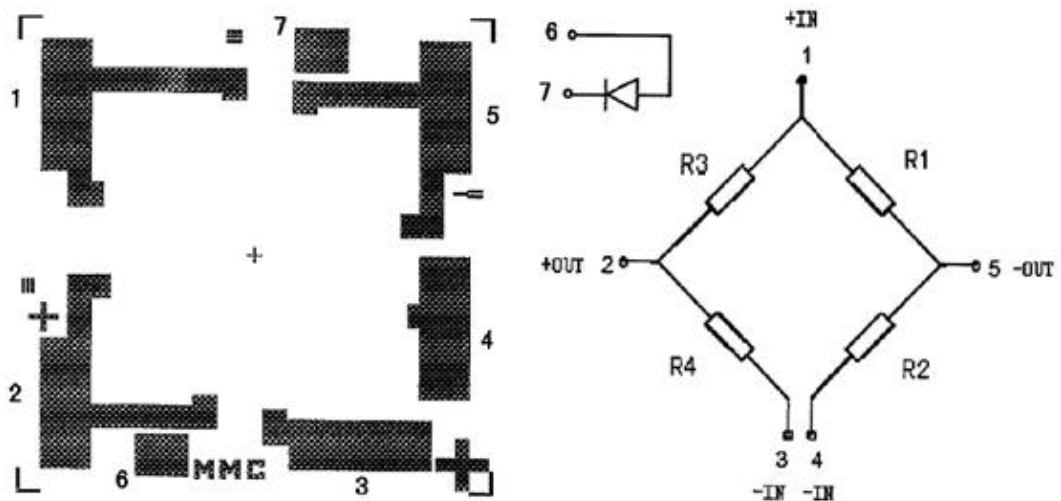
Figure 6.5 Schematic layout of the contact pads.

The top view picture of the fabricated prototype piezoresistive pressure sensor is shown in Fig. 6.4. The area of the full sensor was about 1 mm $\times$ 1 mm. 4 piezoresistors have

been fabricated to make up each device in the Wheatstone bridge. A schematic layout of the contact pads is shown in Fig. 6.5. The dimensions of the contact pads were about 0.3 mm $\times$ 0.105 mm, and the thickness of the aluminium contact pads was between 300 and 400 nm. Using a 5 V DC power supply to provide the input current, pressure changes result in a change in the sensor output voltage of the order of mV. As shown in Fig. 6.6, a standard wire bonding process was used to electrically connect the positive input (Pad 1), positive output (Pad 2), negative input (Pads 3 and 4), and negative output (Pad 5).

(a)
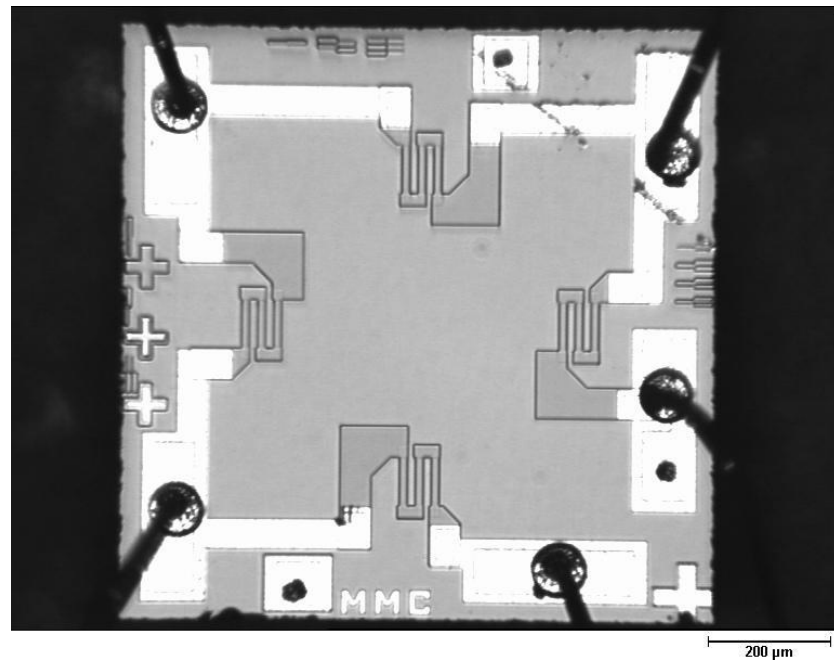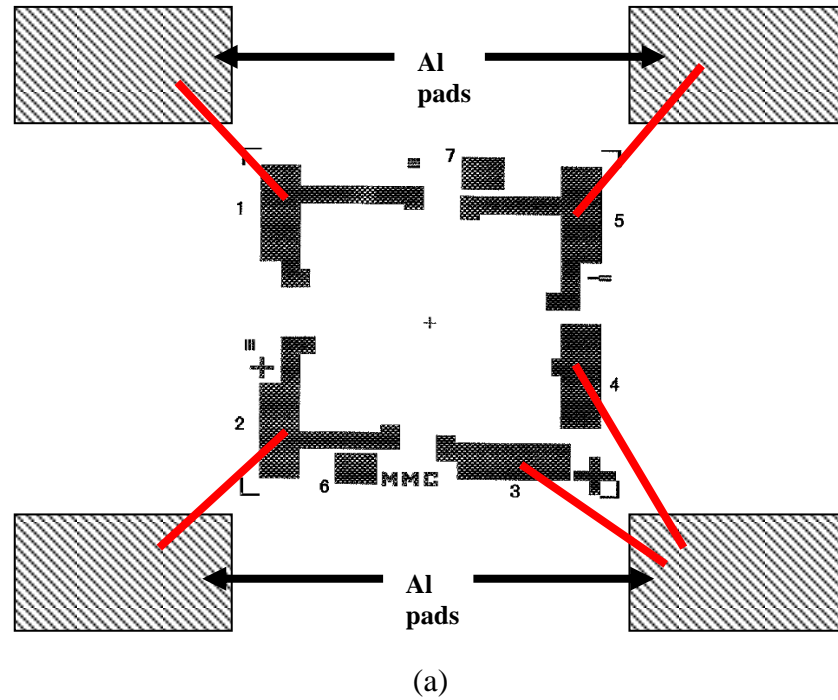
(b)

Figure 6.6 (a) Schematic layout and (b) photo of wire bonded pressure sensor.

6.2 Design of Integrated Multi-Sensors

There is a growing interest in integrating health monitoring functions for advanced electronic systems in order to make a timely decision for system repair or replacement in safety critical applications. Microsystem health monitoring can improve the cost-effectiveness of inspection and maintenance of the systems. With increasing miniaturization and heterogeneous integration of electronic systems enabled by the system-in-package (SiP) technology [47-49], it is becoming difficult to conduct electrical tests using the conventional methods because of limited access to the electrical contacts in stacked packages. Therefore it is necessary to use intelligent health monitoring approaches to determine the status of such systems. Health monitoring methods have already been developed for large systems and large structures, such as aircraft and aerospace vehicles [53-57]. For health monitoring in compact or miniaturized electronic systems, integrated sensors are essential. Fig. 6.7 shows a schematic illustration of an electronic system with integrated sensors for health monitoring. In this case an IC chip and a MEMS chip are integrated on a chip carrier. The health monitoring sensors are integrated with the MEMS chip. For 3-D systems, the microsystem health monitoring sensors or chips can be embedded in the system in package (SiP) structures.
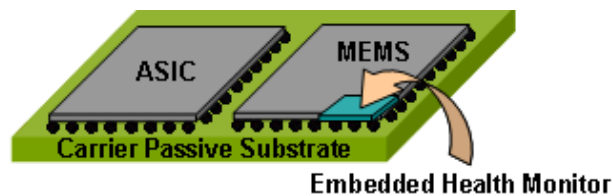
Figure 6.7 Schematic illustration of a microsystem with a health monitoring chip attached [198].

Integration methods have been used to develop microsystem health monitoring applications in advanced electronic systems. For health monitoring in electronic systems, it is necessary to monitor multiple parameters inside a package in order to assess the condition of a microsystem under operation. It is also necessary to monitor the environmental parameters within a microsystem package such as temperature, humidity and pressure. Two sensors single chip integration approaches have been developed. Fig. 6.8 (a) shows a schematic layout of integrated sensors on a $LiNbO_3$ substrate. In this case metal thin film based temperature sensors and SAW based humidity sensors are fabricated on the substrate. A micromachined piezoresistive

pressure sensor is also assembled onto the same chip in order to obtain three integrated sensors on the same substrate. The alternative approach has all of these 3 sensors on a silicon substrate as illustrated in Fig. 6.8 (b). The temperature sensors are fabricated either using a sputtered platinum thin film or using an electron beam evaporated nickel thin film on the substrates. The pressure sensor is produced using the bulk silicon micromachining techniques. The SAW based humidity sensor is fabricated on a piezoelectric thin film such as ZnO or AlN that can be deposited on the silicon substrate by sputtering.

(a)

(b)
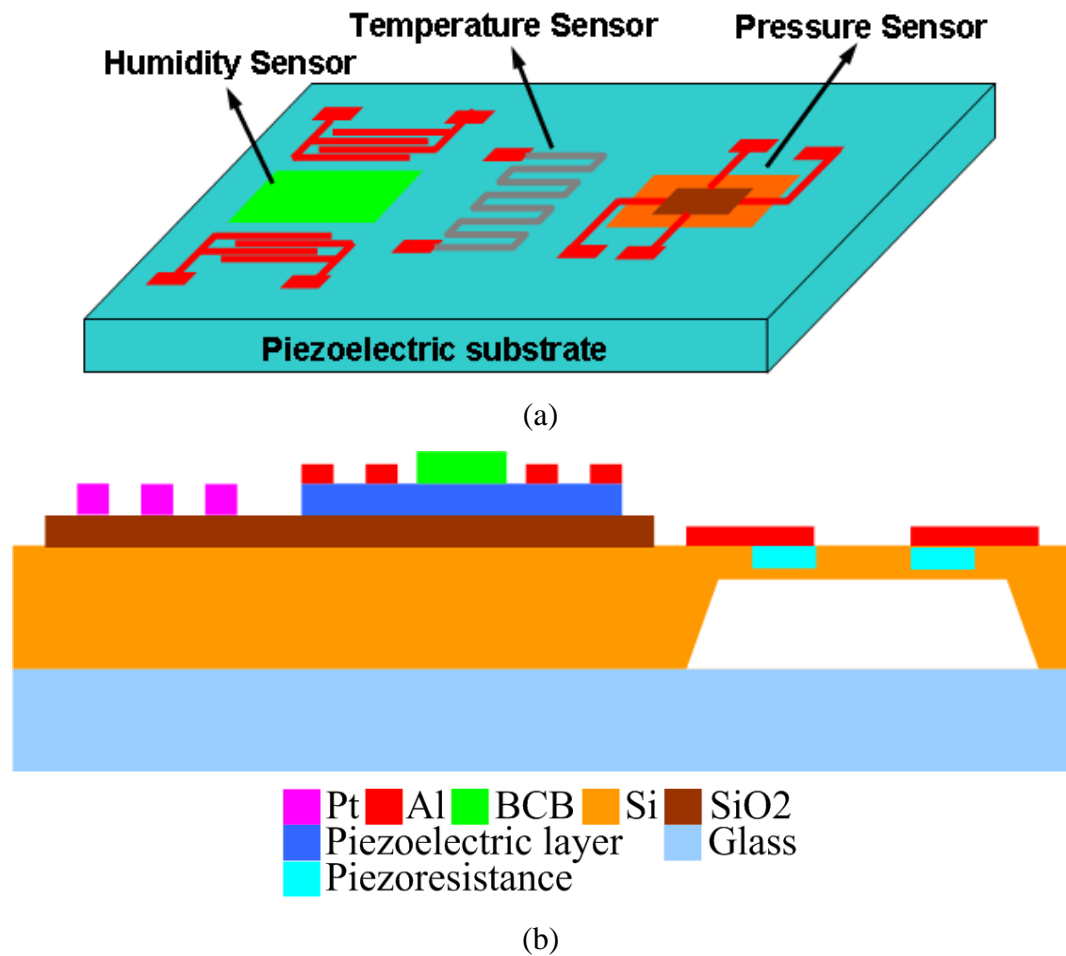
Figure 6.8 Designs of integrated multi-sensors for embedded health monitoring based on (a) piezoelectric substrate (such as $LiNbO_3$) and (b) silicon substrate.

6.3   Fabrication Process of Integrated Multi-Sensors

6.3.1   Design for Integrated Sensors on LiNbO3 Substrate

The fabrication process flow of $LiNbO_3$ based integrated multi-sensors is shown in Fig. 6.9. The platinum thin film temperature sensor is first fabricated by sputtering Pt film of thickness between tens and hundreds of nanometres, which is then patterned into

meander structures using UV photolithography and ion beam etching. The IDTs of the SAW humidity sensor and the contact pads of the pressure sensor can be achieved together in the same process by sputtering an aluminium layer, which is patterned by wet etching. The platinum patterns are able to survive in the aluminium etchant as they remain on the substrate even after the aluminium etch. The BCB moisture capture film of the humidity sensor is fabricated by spin coating and UV photolithography processing. The sensor simply consists of the patterned BCB polymer. The silicon based pre-fabricated piezoresistive pressure sensor would be assembled onto the substrate by hybrid integration with cured glue. Wire bonding process is then used to provide the interconnections between the bond pads on the sensor and bond lines on the substrate.
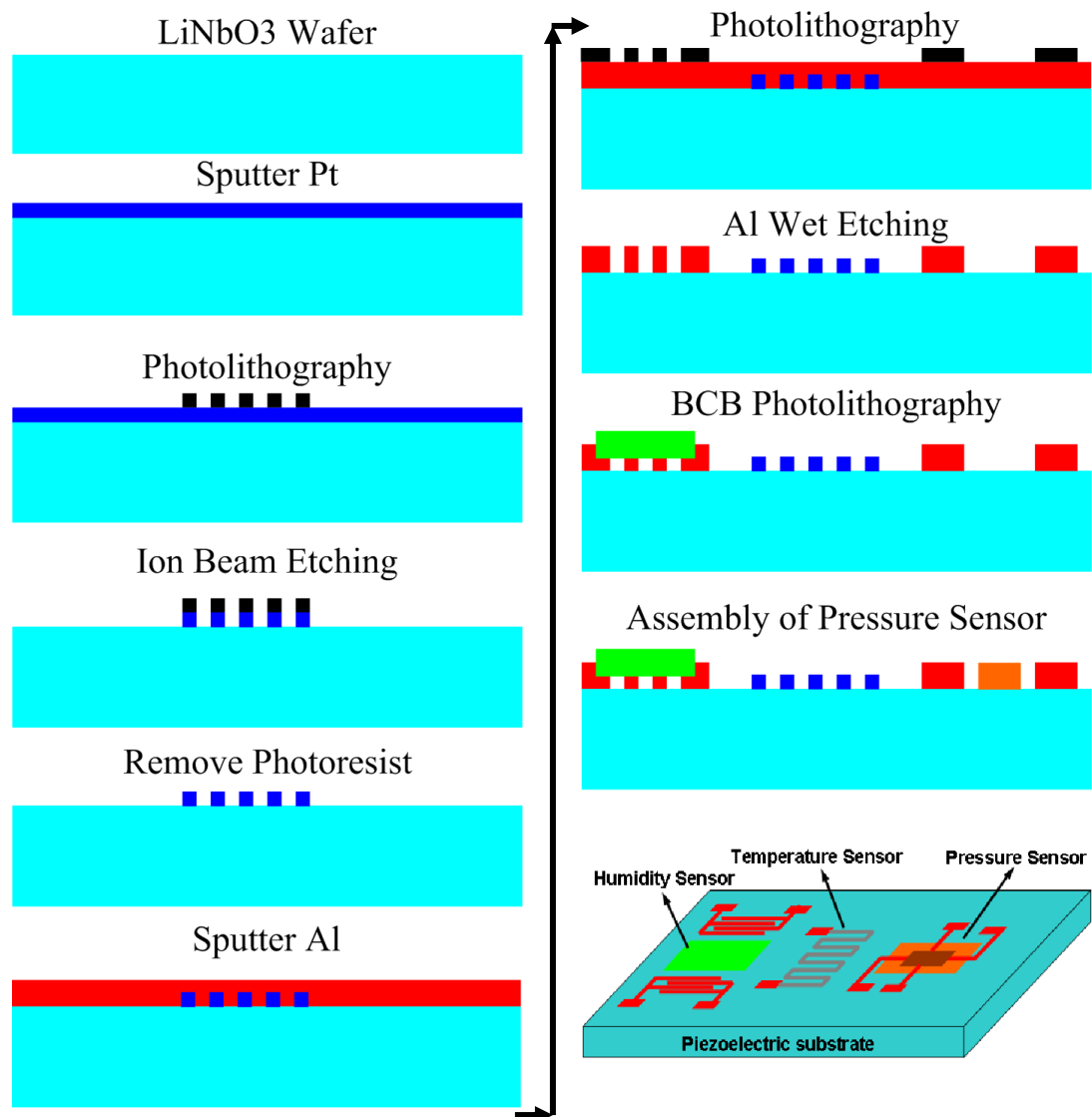
Figure 6.9 Fabrication processes of integrated multi-sensors on LiNbO$_3$ substrate.

6.3.2   *Optimised Design for Integrated Sensors on LiNbO₃ Substrate*

Because of the high cost of platinum, it was decided to investigate the use of nickel as the metal layer of the temperature sensor. Nickel thin film has been developed for replacing the platinum layer in the lift-off process, the details of which are shown in Fig. 6.10. Fabrication of the SAW sensors and the contact pads of the pressure sensors were carried out as the same process as the platinum based process. After the photolithography process for pre-patterning, nickel thin film is deposited by electron beam evaporation. Then, it is patterned by the lift-off process. Finally, the BCB moisture capture films and the pre-fabricated pressure sensors are integrated onto the LiNbO₃ substrate using the same UV photolithography, hybrid integration, and wire bonding techniques.
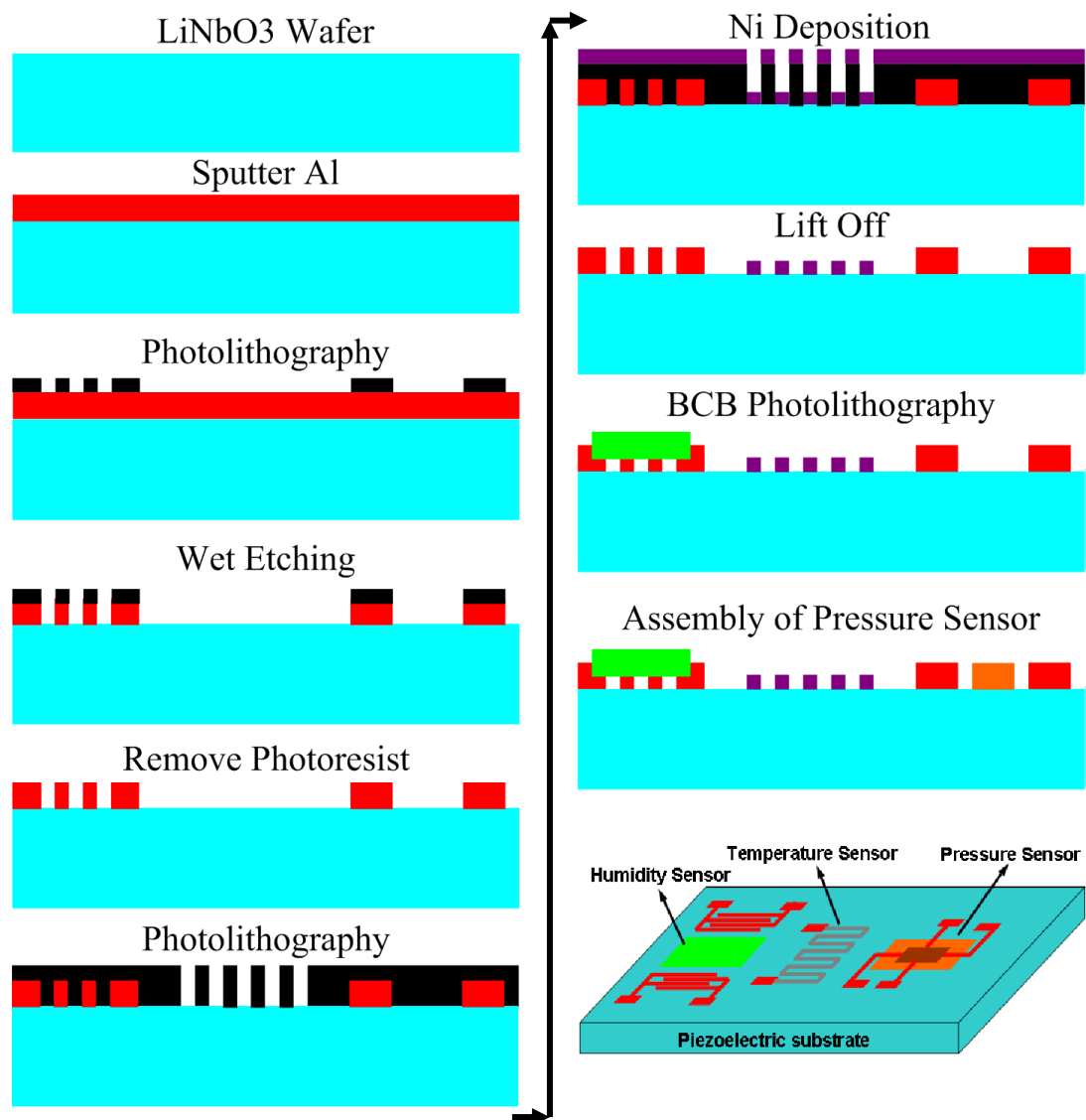
Figure 6.10 Optimised fabrication processes for fabrication of integrated multi-sensors on LiNbO₃ substrates with nickel thin film based temperature sensors.

6.3.3 Design for Integrated Sensors on Silicon Substrate

The temperature, humidity and pressure sensors have also been designed to be fabricated on a silicon substrate. In this process, piezoelectric film is deposited on the silicon substrate to act as the piezoelectric material in the fabrication of SAW based humidity sensors. The details of the fabrication processes are shown in Fig. 6.11. Both the sensors and the integration methods are suitable for applications in heath monitoring in microsystems.
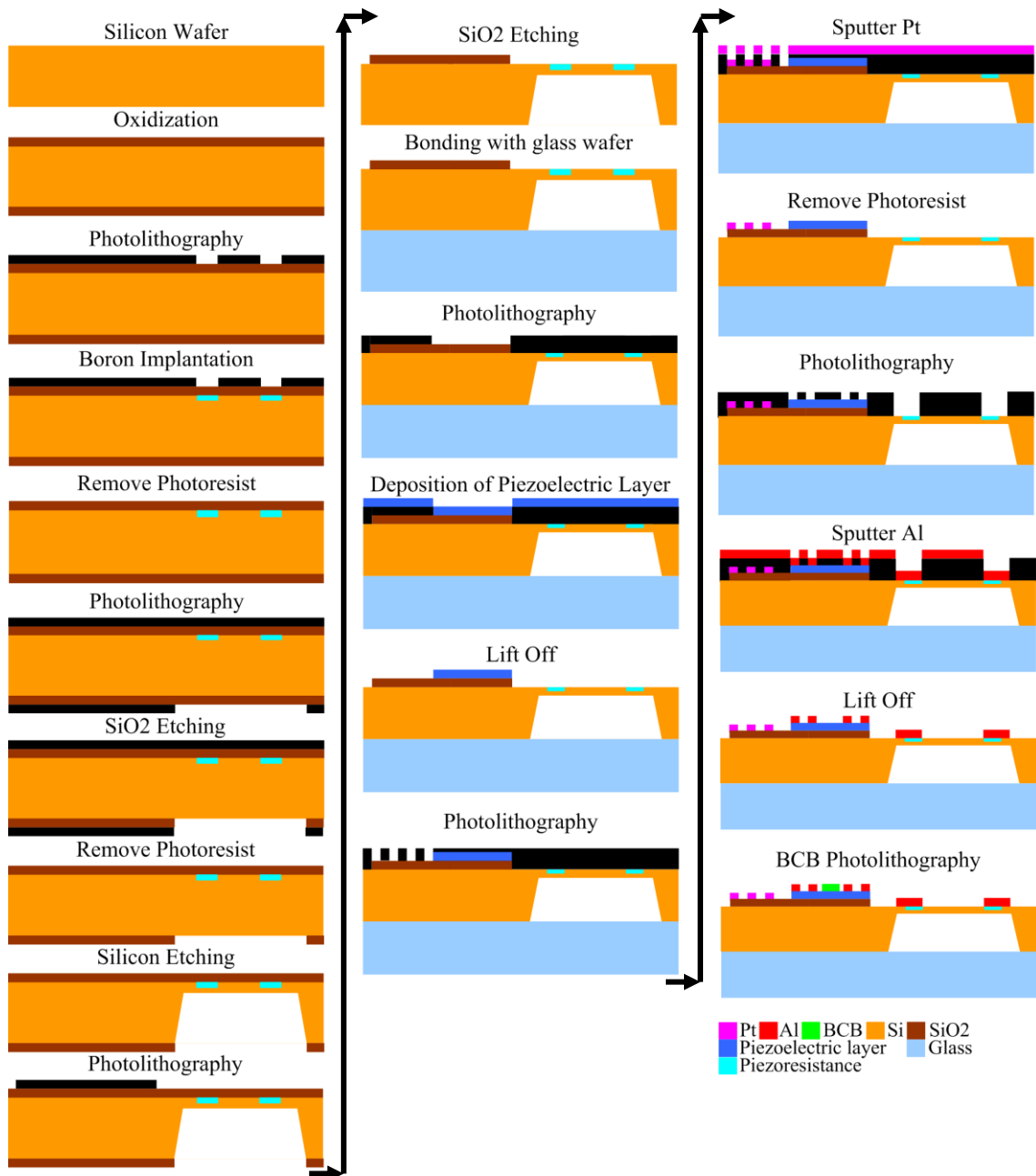
Figure 6.11 Process design of integrated multi-sensors on silicon substrate.

6.4 Fabrication of Integrated Multi-sensors

Based on fabrication capabilities, the LiNbO$_3$ based integration process with platinum thin film temperature sensors, shown in Fig. 6.9, has been carried out to fabricate the integrated multi-sensors. Two 5-inch photomasks were designed for fabrication on the integrated sensors on a LiNbO$_3$ substrate (100mm diameter). The green patterns in Fig. 6.12 represent the Pt film based temperature sensors, and the red patterns are the Al structures for both the IDT of the SAW humidity sensors and the contact pads of the piezoresistive pressure sensors. The widths of Pt meander structures of the temperature sensors were designed as 3, 5, and 10 μm. The widths of the IDTs of the SAW humidity sensors were designed as 4, 8, and 16 μm. A picture of the integrated multi-sensors is shown in Fig. 6.13. The structures for monitoring the pressure sensors and SAW humidity sensors response to temperature change were also included in these mask designs (shown in Fig. 6.14).
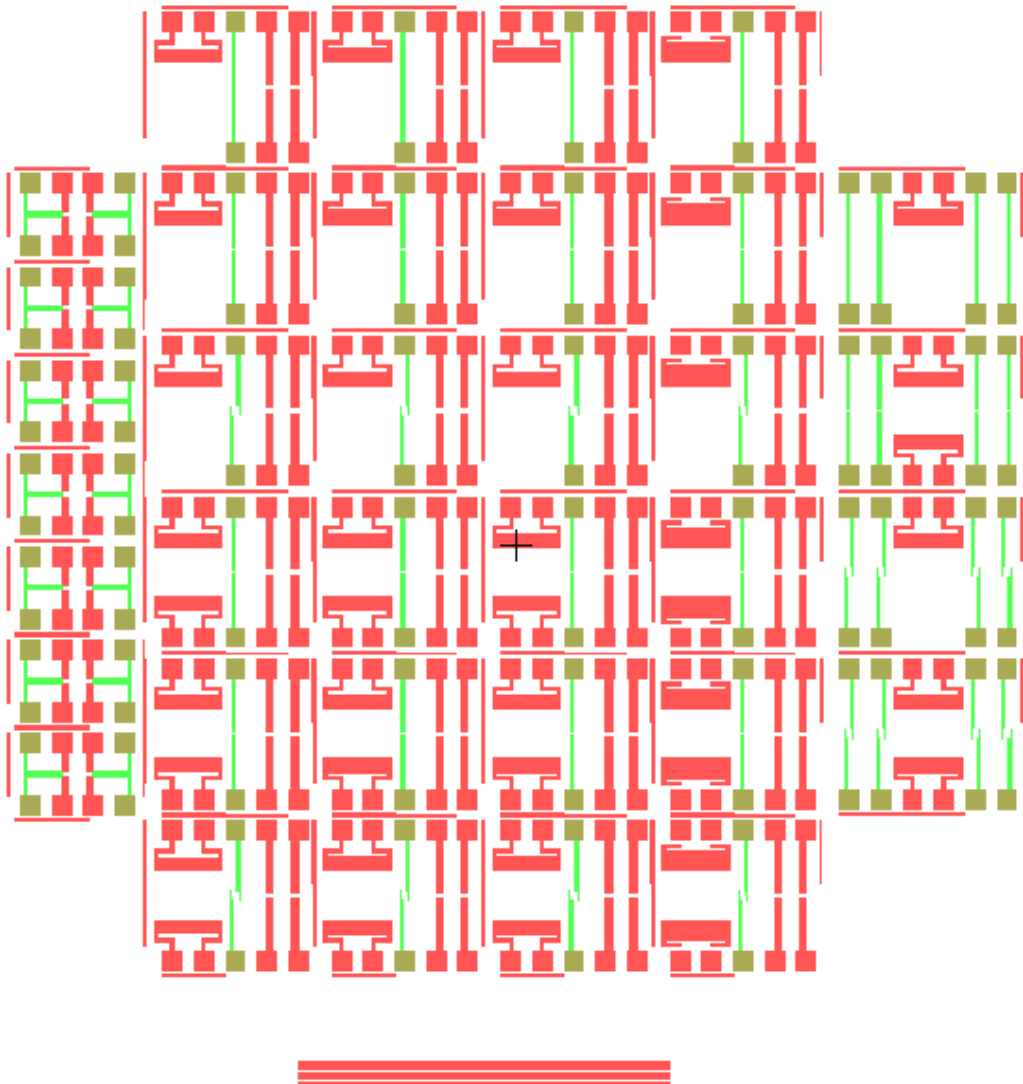
Figure 6.12 Design of photomasks for the integrated multi-sensors.
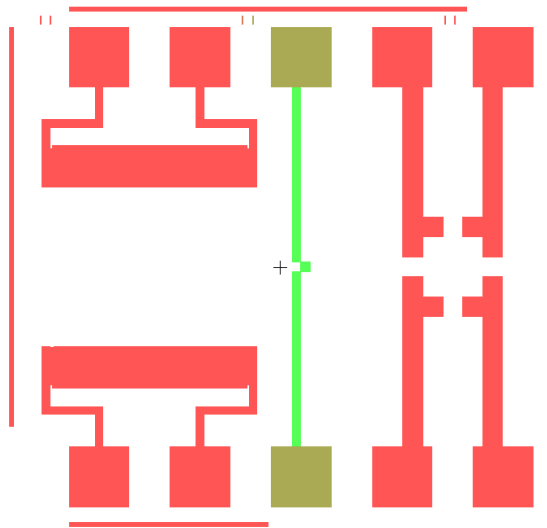
Figure 6.13 Layout of the integrated multi-sensors.
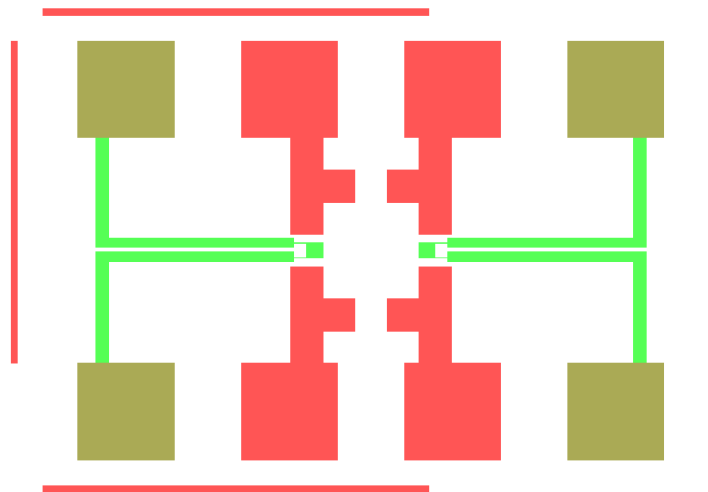
(a)
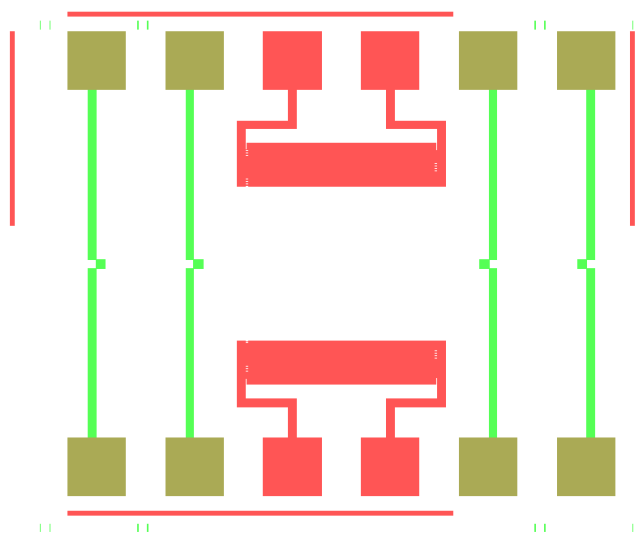
(b)

Figure 6.14 Layout of the designs for monitoring (a) the pressure sensor and (b) the
SAW humidity sensor responses versus temperature change.

Using the fabrication process outlined in Fig. 6.9, a titanium intermediate layer was first sputtered using a Denton Vacuum Deposition System at power of 300 W for 120 seconds resulting in a film having a thickness of 30 nm. Then, the platinum temperature sensing layer was sputtered with the same deposition system at power of 200 W for 300 seconds resulting in a film in thickness of 100 nm. During both sputtering processes, the temperature of $LiNbO_3$ substrate was kept constant at 25^oC. The AZ6112 photoresist was spin coated and patterned using UV photolithography. Fig. 6.15 shows a picture of meander patterns in AZ6112 photoresist after the photolithography process. Using the photoresist mask pattern, the platinum film was etched using an ion-beam etching method with an IonFab 300 Plus (Oxford Instruments) at a power of 300 W for 70 seconds. Fig. 6.16 shows a picture of meander platinum patterns after the ion-beam etching process and after removing the photoresist.
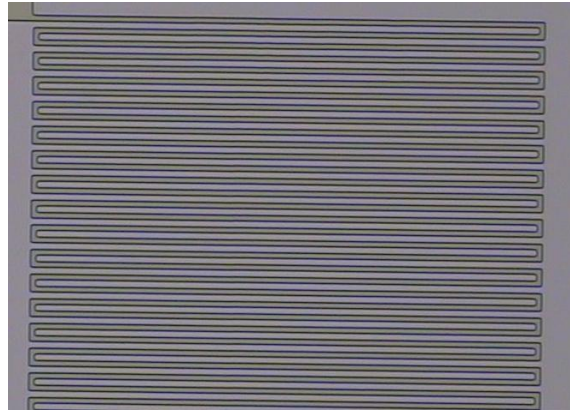
Figure 6.15 Picture of AZ6112 photoresist patterns on platinum film before the ion-beam etching process.

Figure 6.16 Picture of platinum patterns after the ion-beam etching process.

After fabrication of the platinum thin film based temperature sensors, the SAW sensors and the Al contact pads of the pressure sensors were fabricated by deposition of aluminium using a Varian 3180 Sputtering System. This 300 nm thick aluminium layer was subsequently patterned using a wet etching method.

Due to an error during the fabrication process, the SAW device of the integrated sensors was short-circuited and was unable to function. The platinum thin film based temperature sensors have already been successfully fabricated on LiNbO$_3$ substrate and the process design has been now established. So, the fabrication process of LiNbO$_3$ based integrated sensors with nickel thin film temperature sensors (shown in Fig. 6.10) was thus selected to obtain integrated sensors by considering the fabrication cost.

Instead of the combined platinum sputtering and wet etching processes, the lift-off process for patterning electron beam evaporated nickel thin films was developed. By using the negative photoresist, the same photomasks in Fig. 6.12 have been used for the design of fabrication process shown in Fig. 6.10. Negative photoresist, AZ5214, was spin coated on after the Al patterning for forming SAW devices and contact pads for piezoresistive pressure sensors. The process steps for fabrication of the Ni temperature sensors are shown in Fig. 6.17 ((a) to (c) for 5 μm meander structures and (d) to (f) for 10 μm meander structures. Fig. 6.17 (a) and (d) show the pictures of negative photoresist patterned by UV photolithography before the Ni deposition. Fig. 6.17 (b) and (e) show the pictures after Ni thin film deposition by electron beam evaporation. Fig. 6.17 (c) and (f) show the pictures after the Ni lift off process.

After fabrication of both aluminium and nickel layers, the BCB moisture sensing films were patterned, and the pre-fabricated piezoresistive pressure sensor was hybrid integrated onto the LiNbO3 substrate using a cured glue (PERMABOND 820 Cyanoacrylate, Permabond Engineering Adhesives Ltd. UK). The electrical contacts were then completed using the standard wire bonding process. The integrated multi-sensors, shown in Fig. 6.18, were successfully fabricated with a footprint of 13 mm $\times$ 12 mm, based on the optimised fabrication processes shown in Fig. 6.10.

<div align="center">(a)   (b)   (c)</div>

<div align="center">(d)   (e)   (f)</div>
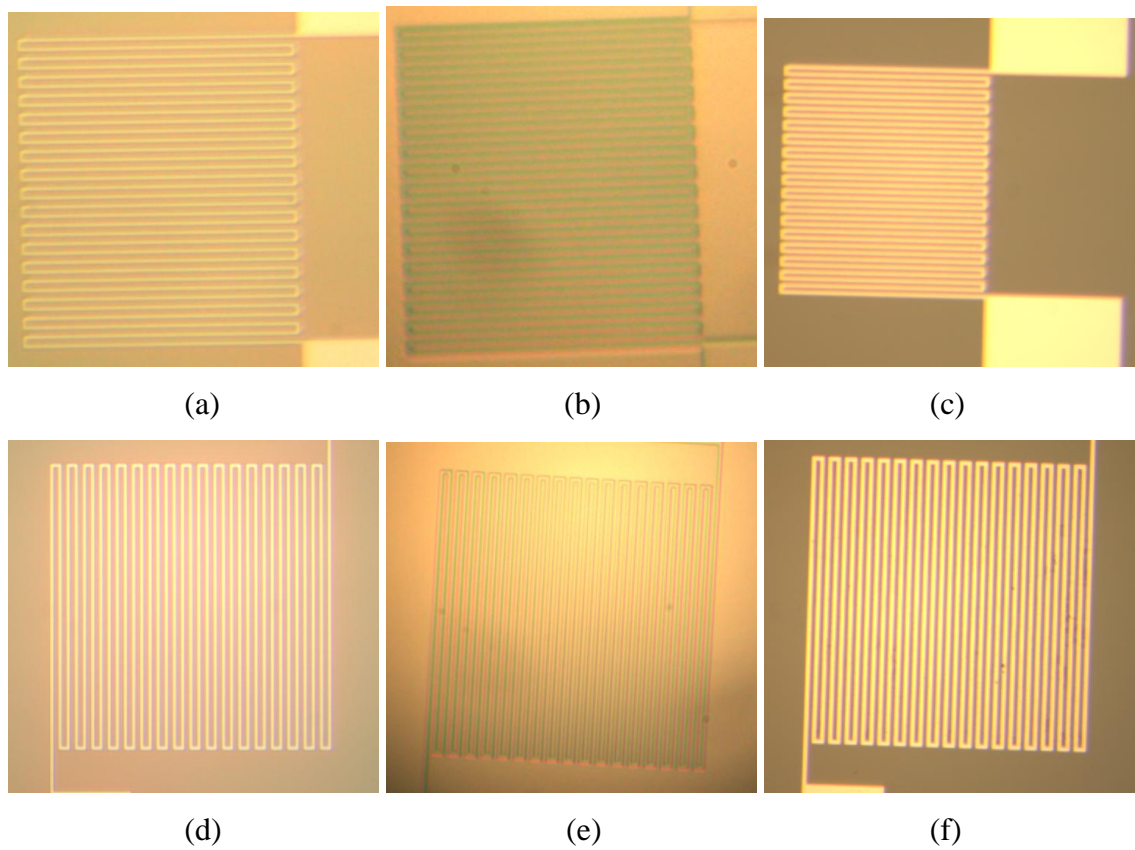
Figure 6.17 Picture of Ni meander structures with width of 5 µm (a) patterned negative photoresist, (b) e-beam evaporated Ni film, (c) fabricated Ni temperature sensor after the lift off; and picture of Ni meander structures with width of 10 µm (d) patterned negative photoresist, (e) e-beam evaporated Ni film, (f) fabricated Ni temperature sensor after the lift off.
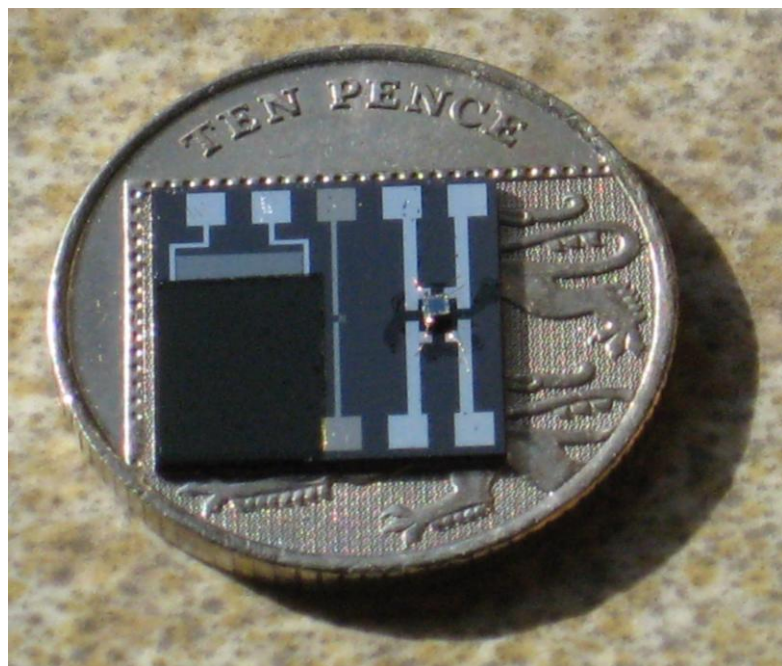
<div align="center">Figure 6.18 Fabricated integrated multi-sensors.</div>

6.5 Characterisation of Fabricated Integrated Multi-sensors

The integrated multi-sensors were successfully fabricated as shown in Fig. 6.18. Characterisation of the integrated microsystem health monitoring sensors was then carried out based on characterisation studies of the individual sensors. The characterisation of the fabricated SAW sensors was carried out using a ZYGO interferometer and a HP8510 Network Analyzer. Thickness and width of fabricated SAW IDTs were studied using a ZYGO interferometer. The results in Fig. 6.19 show that the fabrication process achieves good quality and uniformity. The thickness of the aluminium IDTs was about 378±2 nm, and the tolerance of the aluminium IDT finger width was within ±2.5% (≤0.4 μm).
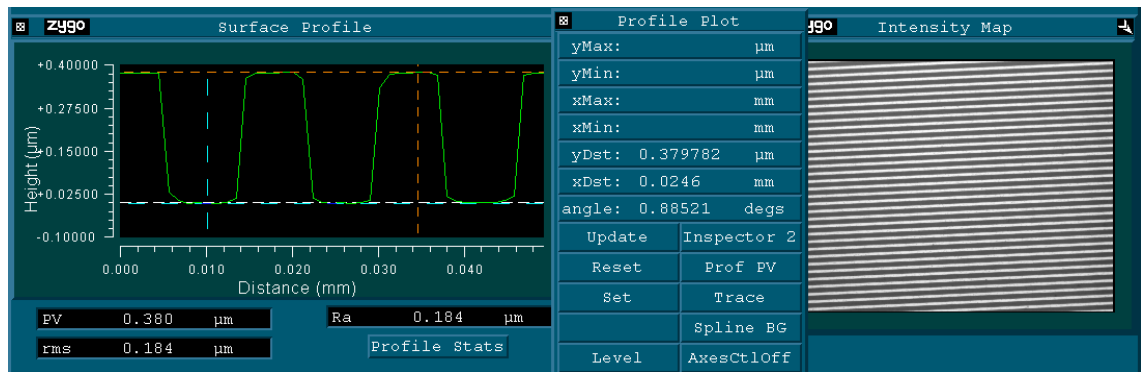
(a)
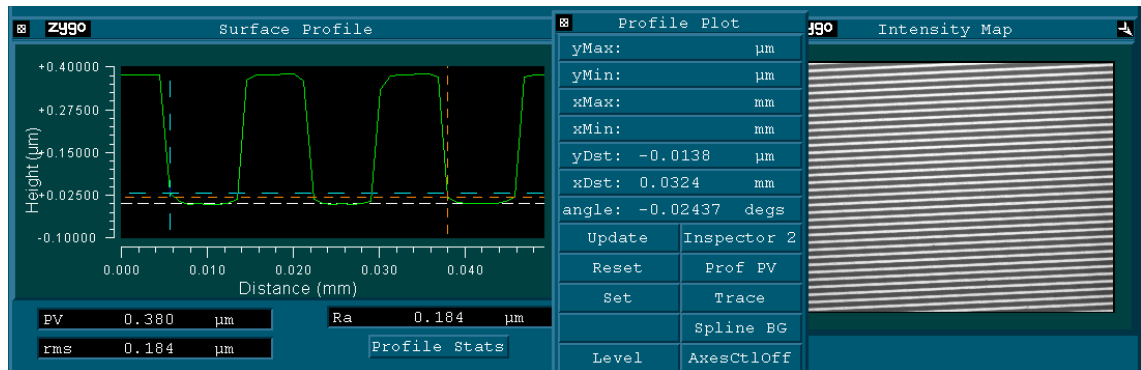
(b)
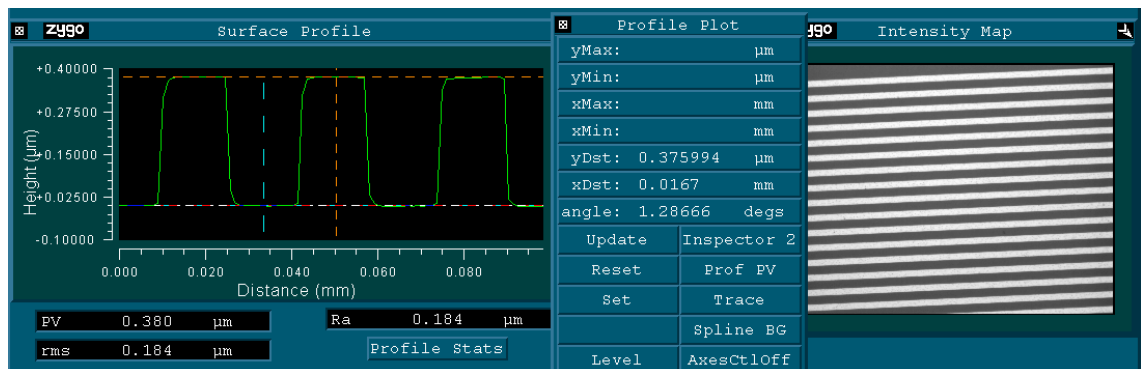
(c)
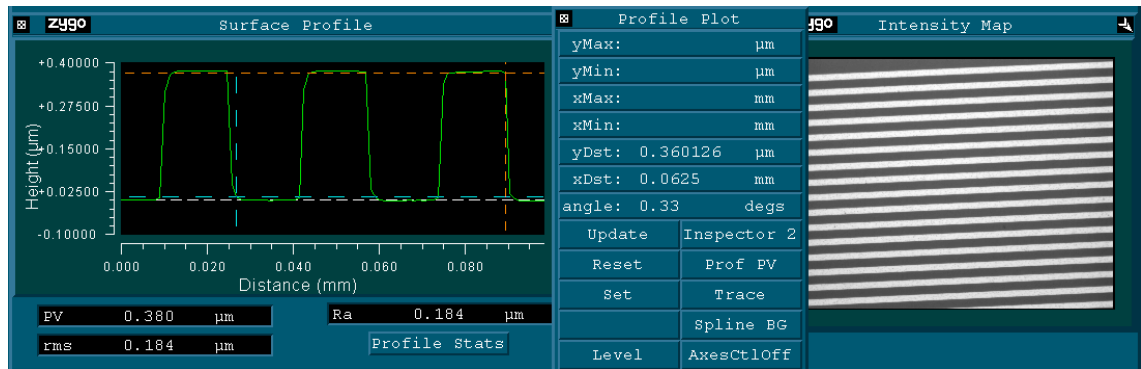
(d)

Figure 6.19 Designed IDT-8 μm with fabricated Al layer of (a) thickness 380 nm, (b) width 8.1 μm; and designed IDT-16 μm with fabricated Al layer of (a) thickness 376 nm, (d) width 15.6 μm.

Using a patterned BCB film, SAW based humidity sensors were characterised using HP8510 Network Analyzer with previously designed test clips connections, and the results at room humidity level are shown in Fig. 6.20. The resonance frequency of this 8 μm IDT width SAW device was recorded at 125.15 MHz and the amplitude was measured at -29.76 dB. More important for the sensing application, all the noise signals of the operating device were below -50 dB. The fabricated BCB film based SAW device on the chip of integrated multi-sensors is suitable for the humidity monitoring applications using the reflection signals.
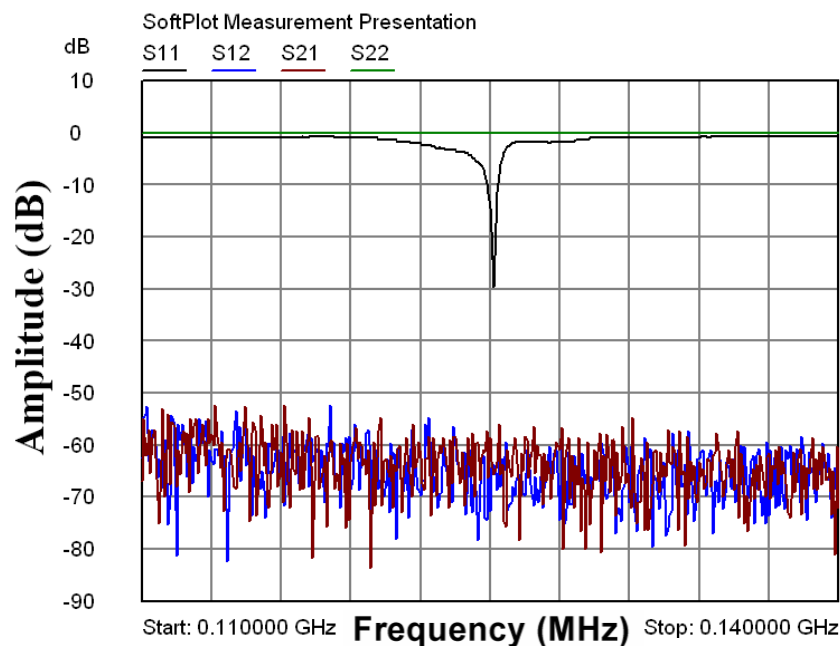
Figure 6.20 Reflection sensing signal of fabricated SAW humidity sensors (IDT widths of 8 μm).

The nickel thin film temperature sensors, with meander structure of widths of 5 and 10 μm, have also been fabricated successfully for the integrated multi-sensors, using a lift off process (shown in Fig. 6.17 (c) and (f)). Characterisation of the nickel thin film sensors was carried out using a ZYGO interferometer. Test results on these sensors show that the nickel thin film of thickness 18.6 nm was successfully obtained (shown in Fig. 6.21 (a)), and tolerance of the fabricated meander track widths was less than ±1%. This nickel thin film temperature sensing thermoresistor was then characterised using a multimeter, and a resistance of about 13.77 kΩ was recorded (shown in Fig. 6.22). The nickel thin film based temperature sensors on the chip of integrated multi-sensors are suitable for the temperature monitoring applications based on their physical characteristics as thermistors.
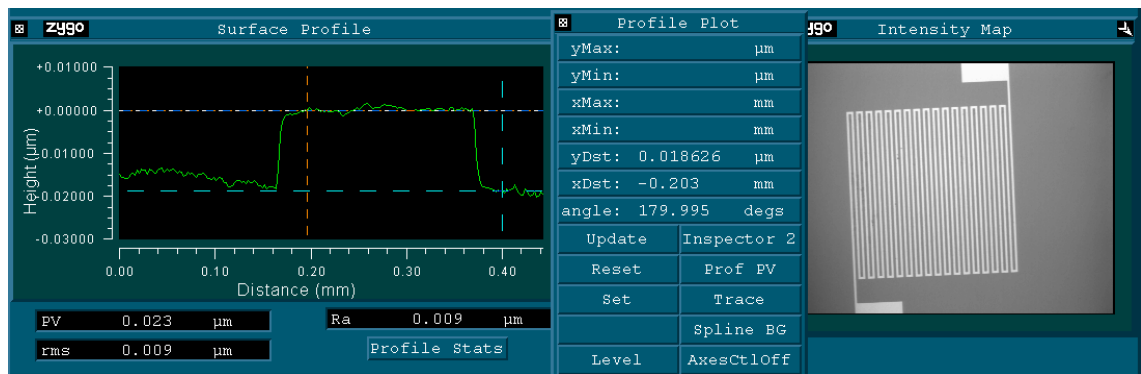
(a)
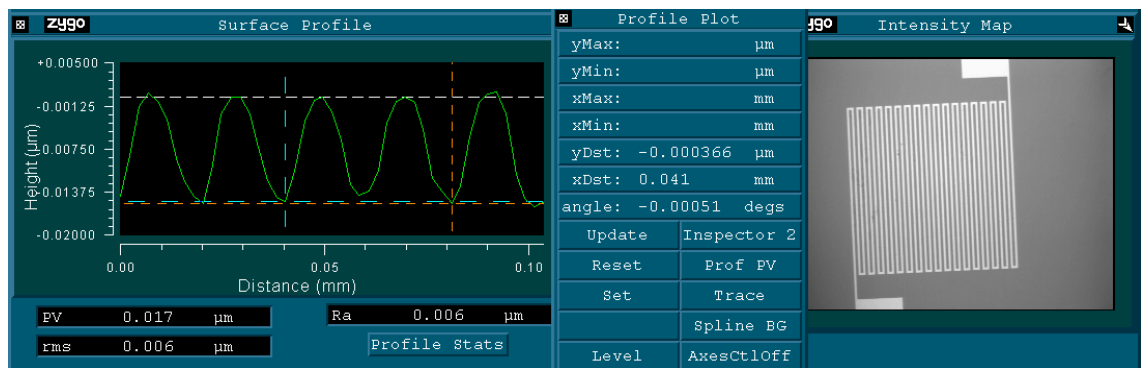
(b)

Figure 6.21 Test results of ZYGO interferometer shows (a) the thickness of nickel film was about 18.6 nm and (b) the designed 10 μm meander structures were fabricated with width of about 10.2 μm.

Figure 6.22 Resistance of Ni thin film temperature sensor on the chip of integrated
sensors being measured with the multimeter.

Figure 6.23 Wire bonded piezoresistive pressure sensor integrated on the multi-sensor
chip by hybrid integration.

The piezoresistive pressure sensors were successfully assembled using a commercial glue (PERMABOND 820 Cyanoacrylate, Permabond Engineering Adhesives Ltd. UK) and electrically connected using the standard wire bonding process. Fig. 6.23 shows that the gold wire contacts were successfully obtained and the piezoresistive pressure sensors are suitable for this hybrid integration process for achieving the integrated microsystem health monitoring sensor applications.

6.6   Temperature Monitoring Chip

Temperature monitoring chips have also been designed and fabricated successfully. The photomasks designs have been shown in Fig. 6.14 (a) and (b). These temperature monitoring chips could be used for self monitoring and automatic correction of piezoresistive pressure sensors, accelerometers, and all other kinds of temperature sensitive microsensors and microsystems. A picture of a fabricated temperature monitoring chip attached with a piezoresistive pressure sensor is shown in Fig. 6.24, which includes two temperature sensors located at the left and right edges of the pressure sensor. A picture of a SAW based temperature monitoring chip is shown in Fig. 6.25, which can be used for real time temperature monitoring and self correction for SAW based resonators, sensors, and filters.
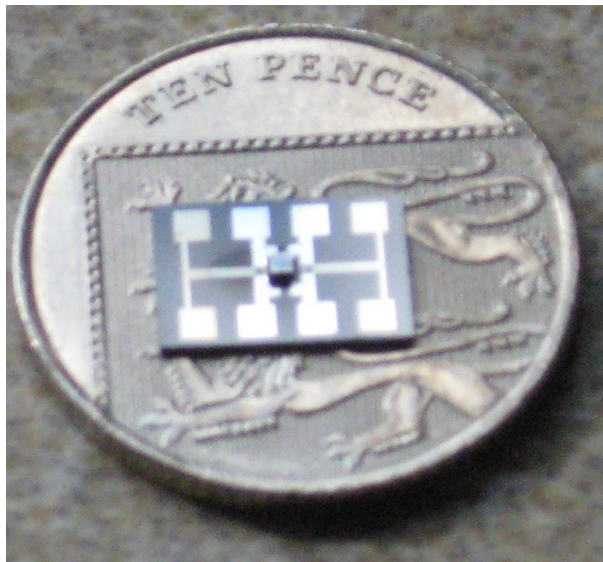
Figure 6.24 Pressure sensor attached on a fabricated temperature monitoring chip.
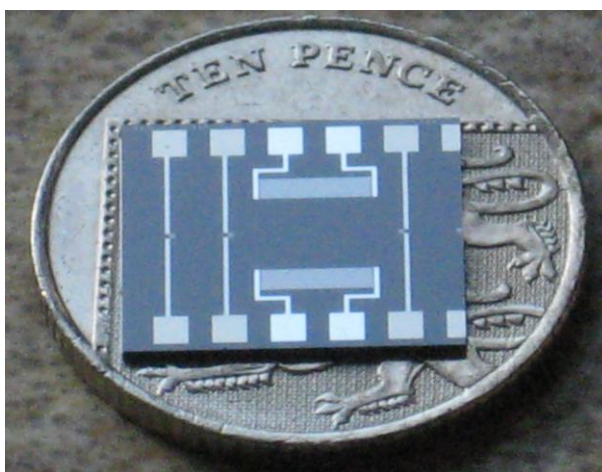
Figure 6.25 Fabricated temperature monitoring chip for SAW devices.

6.7   Summary

A highly boron doped silicon layer was selected for making peizoresistors into piezoresistive pressure sensors. The sensors consist of a vacuum or constant pressure sealed cavity, monitored using a Wheatstone bridge in a DC test circuit. An optimised process for boron implantation has been used for producing pre-fabricated piezoresistive pressure sensors supplied by a research partner. Using a SiO_2 resistant layer of thickness 200 nm to mask the wafer during the ion implant, both the boron implantation and the high concentration boron diffusion could be achieved in one process step.

For applications in heath monitoring in miniature electronic systems, fabrication processes of integrated multi-sensors were designed based on both $LiNbO_3$ and silicon substrates. By considering the fabrication cost, the nickel thin film based fabrication has been further developed and optimised using $LiNbO_3$ substrates. Both the sensor structures and the fabrication processes were studied in detail. Fabrication of integrated multi-sensors based on $LiNbO_3$ substrate has been investigated. Two 5-inch photomasks were designed for fabricating the integrated multi-sensors on 100 mm diameter $LiNbO_3$ substrates. Both IDTs of SAW devices and the contact pads of pressure sensors were fabricated using sputtered Al film, which was patterned using a wet etching method. The temperature sensor was produced using electron beam evaporated Ni thin film, which was patterned using a lift off process. A piezoresistive pressure sensor was hybrid integrated using cured glue and electrically connected using the standard wire bonding process. Successfully fabricated integrated multi-sensors, in a footprint of 13 mm × 12 mm, were characterised using the ZYGO interferometer, HP8510 Network Analyzer, multimeter and microscope. In the integrated multi-sensors, the SAW

humidity sensor was obtained with IDT of thickness of 378±2 nm and different IDTs widths of 8 and 16 μm with a tolerance of about ±2.5%. The resonance frequency of the 8 μm IDT width SAW device was recorded as 125.15 MHz and amplitude was measured at -29.76 dB, while all the noise signals were below -50 dB. The nickel thin film temperature sensor was successfully fabricated with meander structure widths of 5 and 10 μm. Fabricated nickel thin film was 18.6 nm thick and tolerance of track widths was less than ±1%, resulting a resistance of 13.77 kΩ with a meander line width of 10 μm. The integrated piezoresistive pressure sensor was observed using a microscope and was shown to have good electrical interconnects.

A temperature monitoring chip has also been considered and fabricated, and these are suitable for self monitoring of temperature. Also the operating tolerance allows for the automatic correction of temperature sensitive microsensors and microsystems, such as piezoresistive pressure sensors and accelerometers. The work has successfully demonstrated the flexibility of integration of multi-sensors for microsystem health monitoring applications.

Chapter 7   Conclusions and Future Work

7.1   Conclusions

Simulation, fabrication, integration and characterisation of high sensitivity, miniature temperature and humidity sensors has been investigated in this PhD thesis. Platinum thin film temperature sensor arrays have been successfully used for embedded real time monitoring of a laser assisted polymer bonding process. The structure designs, process flows and fabrication of integrated multi-sensors for embedded health monitoring of microsystems have also been investigated in detail. Using an optimised fabrication process and hybrid method, integrated multi-sensors have been successfully fabricated on a LiNbO$_3$ substrate with a footprint of 13 mm $\times$ 12 mm with multi monitoring functions for temperature, humidity and pressure.

Based on the theoretical analysis and FEM simulations, the metal thin film temperature sensors have been designed in meander structures with track widths of 3, 5, 7 and 10 μm. The footprint of the thin film temperature sensor with a 3 μm track width was just 240 μm $\times$ 250 μm. Deposited by sputtering and patterned by ion-beam etching process, the platinum based temperature sensors have been fabricated and allow a good linear response. Nickel based sensors have also been fabricated successfully using electron beam evaporation and wet etching methods. The nickel based sensor with 5 μm of track width had a sensitivity of 32.25mV/K at a constant current of 0.1mA. An annealing process was subsequently used to stabilise the Ni thin film sensor. After the annealing process, the corresponding temperature coefficients of resistance (TCR) of the platinum based sensors were determined to be from $1.78 \times 10^{-3} / \degree C$ to $2.26 \times 10^{-3} / \degree C$ at 20 $\degree C$.

An experimental study of accurate temperature monitoring in a laser assisted BCB polymer bonding process for MEMS packaging was carried out using an embedded thin film microsensor array. Beam forming optical elements were used to generate top-hat and frame-shaped beam profiles. The results showed that the amplitude and characteristic of the laser generated temperature change not only depends on the laser power but also depends on the package assembly to be bonded and the configuration of materials in the bonding setup. Three kinds of package assemblies were studied, including silicon cap to glass substrate, glass cap to silicon substrate and silicon cap to silicon substrate. Using a frame-shaped beam, the temperature at the centre of the

bottom substrate was obtained as ~50°C lower compared to that obtained using a top-hat beam. The reduction of temperature at the centre device packaging area is highly beneficial for MEMS packaging of temperature sensitive devices. Using a single exponential function to describe the temperatures characteristics, results show that the thermal constants of package assemblies are largely independent of the beam profiles but highly dependent on the thermal arrangement of the materials underneath the bottom substrate.

Utilizing the moisture capture capabilities of BCB films, SAW based humidity sensors have been designed and fabricated on 128° cut lithium niobate piezoelectric substrates. The sensors use IDTs with widths of 4, 8 and 16 μm. Measured using a HP8510 Network Analyzer, the resonance frequencies of the fabricated SAW sensors were 248.60, 124.82, and 61.20 MHz, respectively. These are in good agreement with the theoretical values of 249.50, 124.75, and 62.19 MHz (with SAW velocity of 3992 m/s for 128° cut LiNbO$_3$ substrates). Two test configurations, using silver loaded epoxy and using test clips, were developed using two types of metal contact connections. There was a negligible difference between results of measurement using the two different connection configurations. Test results on SAW sensor show that the chemically reduced lithium niobate substrates had the same piezoelectric properties as regular lithium niobate substrates. The measured Q factor of a SAW sensor with IDT width of 8 μm was increased 27.4%, from 581 to 740 by the application of the reflection grating structures. The temperature change resulted in shift of the SAW resonance frequency by 4.26 kHz/°C, around 34 ppm change in the resonance frequency of 124.82 MHz. Based on the reflection signals of the BCB based SAW humidity sensors, a sensitivity of 0.26 dB/RH% was achieved under controlled humidity level between 8.6% and 90.6% RH.

After the design, fabrication and testing of the metal thin film based temperature sensors and the BCB films based SAW humidity sensors, the structure designs and the fabrication processes were performed on both LiNbO$_3$ and ZnO/Si substrates for applications in heath monitoring of miniature electronic systems. Prototype piezoresistive pressure sensors operating at different ranges of 0 to 1.5 bar and 0 to 7 bar were selected for the hybrid integration on a single chip with the temperature and humidity sensors. Two 5-inch photomasks were designed for fabricating the integrated multi-sensors on the LiNbO$_3$ substrates. The widths of metal thin film meander structures of the temperature sensors were designed as 3, 5, and 10 μm. The widths of

the IDTs of the SAW humidity sensors were designed as 4, 8, and 16 μm. The aluminium structures for both the IDT of the SAW humidity sensors and the contact pads of the piezoresistive pressure sensors were fabricated with just one process step. This saves one photomask as well as the cost of UV photolithography process time. Using an optimised fabrication process, the integrated multi-sensors were successfully fabricated on a LiNbO$_3$ substrate with a footprint of 13 mm $\times$ 12 mm with multi monitoring functions for temperature, humidity and pressure sensing applications.

7.2 Future work

In the work described in this thesis, high sensitivity miniature temperature, humidity and pressure sensors have been successfully integrated on a single substrate. The sensors have the potential to be used for not only the health monitoring of Microsystems but also for intelligent process controls and embedded conditional monitoring applications. In hybrid integration and SiP technologies, integrated multi-sensors can meet the challenges of test and reliability validation. This provides low-cost integration of functions for self-testing of system interconnects. Key parameters can be monitored in mission mode and a level of fault tolerance/self-repair can be achieved.

After successful fabrication and characterisation, the integrated multi-sensors could be used for other applications such as intelligent process control and embedded conditional monitoring. By further studying of the long term stability, packaging technology would be properly considered for sensor protection, especially for the BCB based SAW humidity sensors, which will lead to the enhancements of both sensitivity and the reliability of the operating sensors. A reduction of SAW reflection amplitude and sensor's sensitivity was observed after 41 days of the initial test (shown in Fig. 7.1). This may be because the BCB sensing film was contaminated since the unpackaged sensor was operated outside the cleanroom environment. Meanwhile, the linear relationship between the relative humidity level and the amplitude of the SAW reflection signals could be interesting to be studied and discussed in theoretical details.
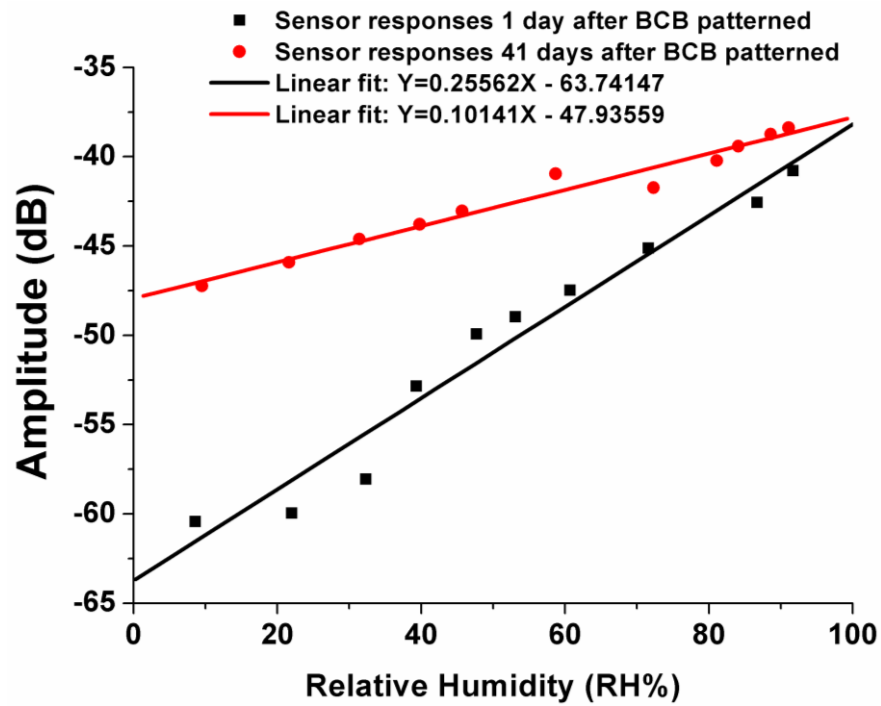
Figure 7.1 Stability test of BCB film based SAW humidity sensor.

Other thin film materials with moisture absorbing abilities instead of BCB, such as polyimide, fluoropolyol (FPOL), and polyvinyl-alcohol (PVA), could also be used for the LiNbO$_3$ based integrated microsystem health monitoring sensors. Meanwhile, BCB resins with different thicknesses available from Dow Chemical Company (USA) could also be used for SAW humidity sensing in order to determine the optimised film thickness and meet different humidity sensing requirements. This could also be achieved by using either a multi spin coating process to achieve thicker BCB films or spin coating with the diluted BCB resins to achieve thinner BCB sensing films.

Additional sensors with different sensing functions could also be considered for further development of the integrated multi-sensors. Further study of the combination of fabrication and integration processes based on a variety of substrates such as silicon, glass, piezoelectric substrates including LiNbO$_3$ and PZT, Low Temperature Co-Fired Ceramics (LTCC), and polymer based flexible substrates could be performed.

References

[1] M.X. Sham, Y.C. Chen, L.W Leung, et al., "Challenges and Opportunities in System-in-Package (SiP) Business", 7th International Conference on Electronic Packaging Technology (ICEPT '06), 26-29 Aug. 2006 Page(s):1–5.

[2] V. Garg, S. Lacy, D.E. Schimmel, et al., "Incorporating multi-chip module packaging constraints into system design", Proceedings of European Design and Test Conference, 1996 (ED&TC 96), 11-14 March 1996 Page(s):508–513.

[3] System in a Package (SIP), www.SiliconFarEast.com.

[4] Rao Tummala, "SoC vs. MCM vs SiP vs. SoP", Advanced Packaging, ap.pennnet.com, July, 2006.

[5] Seunghee Park, Chung-Bang Yun and Daniel J. Inman, "A Self-contained Active Sensor System for Health Monitoring of Civil Infrastructures", 5th IEEE Conference on Sensors, 2006, Oct. 2006 Page(s):798–802.

[6] Yan Yu and Jinping Ou, "Design of wireless intelligent sensor for structural health monitoring", Proceedings of Intelligent Sensors, Sensor Networks and Information Processing Conference, 2004, 14-17 Dec. 2004 Page(s):1–5.

[7] B. Nickerson and R. Lally, "Development of a smart wireless networkable sensor for aircraft engine health management", IEEE Proceedings of Aerospace Conference, 2001, Volume 7, 10-17 March 2001 Page(s):3255–3262.

[8] S. George, "Development of a vibration-powered wireless temperature sensor and accelerometer for health monitoring", IEEE Proceedings of Aerospace Conference, 2006, 4-11 March 2006 Page(s):1-8.

[9] S.A. Lewis and T.G. Edwards, "Smart sensors and system health management tools for avionics and mechanical systems", Digital Avionics Systems Conference, 1997. 16th DASC., AIAA/IEEE Volume 2, 26-30 Oct. 1997 Page(s):8.5(1)-8.5(7).

[10] J. Bryzek, "Impact of MEMS technology on society", Sensors and Actuators A, Vol 56, 1996 Page(s):1-9.

[11] K. Gilleo, "MEMS challenge: can this technology catch the internet lightwave", IMECE 2000 MEMS Symposium, Orlando, Nov 5-10, 2000 Page(s):615-622.

[12] http://www.zyvex.com/nanotech/feynman.html (Date: 30/10/2010)

[13] http://www.same-conference.org/same_2003/images/documents/tutorials/Tutorial_3_MEMS_P1 (Date: 30/10/2010)

[14] http://www.aero.org/publications/helvajian/helvajian-1.html (Date: 30/10/2010)

[15] http://robotics.eecs.berkeley.edu/~pister/245/Notes/Intro.pdf (Date: 30/10/2010)

[16] M. Abraham, W. Ehrfeld, V. Hessel et al., "Microsystem Technology: Between Research and Industrial Application", Microelectronic Engineering, Volumes 41-42, March 1998, Page(s): 47-52.

[17] S. Wu，Q. Lin，Y. Yuen, et al.,"MEMS flow sensors for nanofluidic applications", IEEE Proc of 13th Annual International Conference on MEMS, Miyazaki(Japan), 23-27 Jan 2000 page(s): 745-750.

[18] Khalil Najafi, "Smart Sensors", J. Micromech. Microeng, 1(1991) page(s): 86-102.

[19] Elena Gaura and Robert Newman, Smart Mems and Sensor Systems, illustrated edition, Imperial College Press, Sep 2006.

[20] Liao CanXing, Li Xingshan, Zhang Ping, and Dai Jing, A Review on Optimal Sensor Placement for Health Monitoring, 8th International Conference on Electronic Measurement and Instruments (ICEMI) 2007, Page(s): 4-170 - 4-173.

[21] T. Becker, M. Kluge, J. Schalk, K. Tiplady, C. Paget, U. Hilleringmann, T. Otterpohl, Autonomous Sensor Nodes for Aircraft Structural Health Monitoring, IEEE Sensors Journal, Volume: 9 , Issue: 11, 2009, Page(s): 1589 - 1595.

[22] R.K. Draney, High Temperature Sensor for Bearing Health Monitoring, 2008 IEEE Aerospace Conference, Page(s): 1 - 7.

[23] A. Zalt, V. Meganathan, S. Yehia, O. Abudayyeh, and I. Abdel-Qader, Evaluating sensors for bridge health monitoring, 2007 IEEE International Conference on Electro/Information Technology, Page(s): 368 - 372.

[24] S. Fatikow and U. Rembold, Microsystems Technology and Micro-robotics, Springer-Verlag, Berlin, 1997.

[25] D. Qu and S. Gao, "Researches on Microelectromechanical Systems and Its

Applications", SCIENCE & TECHNOLOGY REVIEW, No.4 (204) page(s):17-21.

[26] J.M. Bustillo, R.T. Howe and R.S. Muller, "Surface micromachining for microelectromechanical systems", Proceedings of the IEEE, Volume 86, Issue 8, Aug. 1998 Page(s):1552–1574.

[27] http://www.aero.org/publications/helvajian/helvajian-2.html (Date: 30/10/2010)

[28] G.T.A. Kovacs, N.I. Maluf and K.E. Petersen, "Bulk micromachining of silicon", Proceedings of the IEEE, Volume 86, Issue 8, Aug. 1998 Page(s):1536-1551.

[29] M. Esashi, "Microsystems by Bulk Micromachining", 30th European Microwave Conference, Oct. 2000 Page(s):1-4.

[30] M. Esashi, Y. Haga, "Silicon bulk micromachining", 1st Annual International Conference On Microtechnologies in Medicine and Biology, 12-14 Oct. 2000 Page(s):7-12.

[31] http://www.suss.com/applications/wafer_bonding/ (Date: 30/10/2010)

[32] Laura Peters, "Wafer Bonding Enables New Technologies and Applications", http://www.semiconductor.net/article/CA331034.html (Date: 30/10/2010)

[33] M.A. Schmidt, "Wafer-to-wafer bonding for microstructure formation", Proceedings of the IEEE, Volume 86, Issue 8, Aug. 1998 Page(s):1575–1585.

[34] Z.H. Zhu, F.E. Ejeckam, Y. Qian, etc.., "Wafer bonding technology and its applications in optoelectronic devices and materials", IEEE Journal of Quantum Electronics, Volume 3, Issue 3, June 1997 Page(s):927-936.

[35] http://www.freepatentsonline.com/4170472.html (Date: 30/10/2010)

[36] V.L. Spiering, J.W. Berenschot, M. Elwenspoek, etc.., "Sacrificial wafer bonding for planarization after very deep etching", Journal of Microelectromechanical Systems, Volume 4, Issue 3, Sept. 1995 Page(s):151-157.

[37] Z. Tong, "MEMS Technology and Process Equipments", Equipment for Electronic Products Marufacturing, Vol33, No.1, 2004, page(s):5-11.

[38] Wannok Sio, "MEMS (Microelectromechanical System)", Oct. 2002,

http://www.engr.ku.edu/~rhale/ae510/websites_f02/mems.pdf
(Date: 30/10/2010)

[39] Salvatore A. Vittorio, "Review Article: MicroElectroMechanical Systems (MEMS)", Oct. 2001, http://www.csa.com/discoveryguides/mems/overview.php (Date: 30/10/2010)

[40] J.A. Walraven, "Introduction to applications and industries for microelectromechanical systems (MEMS)", Test Conference, 2003. Proceedings. ITC 2003. International, Volume 1, Sept. 30-Oct. 2, 2003 Page(s):674–680.

[41] http://www.answers.com/topic/multi-chip-module (Date: 30/10/2010)

[42] http://www.eleceng.adelaide.edu.au/Personal/alsarawi/node12.html (Date: 30/10/2010)

[43] http://www.cmac.com/dms/services/manufacture/packaging/MCMs.php (Date: 30/10/2010)

[44] Toshio Sudo, "Present and Future Directions for Multichip Module Technologies", VLSI Circuits, 1994. Digest of Technical Papers, 1994 Symposium on JUNE 9-11, 1994 Page(s):51–54.

[45] R.H. Bruce,W.P. Meuli and Ho Jackson, "Multi Chip Modules", Design Automation, 1989. 26th Conference on 25-29 June 1989, Page(s):389 – 393.

[46] V. Garg, S. Lacy, D.E. Schimmel, etc., "Incorporating multi-chip module packaging constraints into system design", European Design and Test Conference, 1996. ED&TC 96. Proceedings, 11-14 March 1996 Page(s):508 – 513.

[47] Robert C. Pfahl, "System in Package Technology", International Electronics Manufacturing Initiative, 2005.

[48] Jani Miettinen, Matti Mantysalo, Kimmo Kaija, and Eero O. Ristolainen, System Design Issues for 3D System-in-Package (Sip), Proceedings of 54th Electronic Components and Technology Conference, 2004, Vol.1, Page(s): 610 - 615.

[49] J. Miettinen, M. Mantysalo, K. Kaija, etc., "System design issues for 3D system-in-package (SiP)", Electronic Components and Technology Conference, 2004. Proceedings. Volume 1, 1-4 June 2004 Page(s):610–615.

[50] www.elecdesign.com, "Packaging Rides The Z Axis Into The Third Dimension", Penton Media, Inc.. (Date: 30/10/2010)

[51] http://www.eetimes.com/news/design/showArticle.jhtml?articleID=188701766& pgno=1 (Date: 30/10/2010)

[52] Joseph Adam and Mark Bird, SiP Technology Offers Packaging Alternatives for Design, Source: http://www.electroiq.com/index/display/packaging-article-display/211535/articles/advanced-packaging/volume-13/issue-9/features/cover-story/sip-technology-offers-packaging-alternatives-for-design.html (Date: 30/10/2010)

[53] A. Mishra, F.M. Gondal, A.A. Afrashteh, etc., "Embedded wireless sensors for aircraft/automobile tire structural health monitoring", 2nd IEEE Workshop on Wireless Mesh Networks (WiMesh), 2006 Page(s):163 – 165.

[54] G.B.Tait and R.S. Rogowski, "Fibre Bragg grating sensors for real-time health monitoring of aerospace vehicles", Quantum Electronics and Laser Science Conference, 22-27 May 2005, Volume 2, Page(s):924 – 926.

[55] J.W. Borinski, S.A. Meller, W.J. Pulliam, etc., "Aircraft health monitoring using optical fiber sensors", Proceedings of Digital Avionics Systems Conferences (DASC), 7-13 Oct. 2000. Volume 2, Page(s):6D1/1 - 6D1/8.

[56] B. Nickerson and R. Lally, "Development of a smart wireless networkable sensor for aircraft engine health management", Proceedings of IEEE Aerospace Conference, 10-17 March 2001. Volume 7, Page(s):3255 – 3262.

[57] Seunghee Park, Chung-Bang Yun and Daniel J. Inman, "A Self-contained Active Sensor System for Health Monitoring of Civil Infrastructures", 5th IEEE Conference on Sensors, Oct. 2006. Page(s):798 – 802.

[58] G. Konstantinidis, P.D. Wilcox and B.W.Drinkwater, "An Investigation Into the Temperature Stability of a Guided Wave Structural Health Monitoring System Using Permanently Attached Sensors", Sensors Journal, IEEE. Volume 7, Issue 5, May 2007 Page(s):905 – 912.

[59] J.W. Borinski, C.D. Boyd, J.A. Dietz, etc., "Fiber optic sensors for predictive health monitoring", AUTOTESTCON Proceedings of IEEE Systems Readiness Technology Conference, 20-23 Aug. 2001, Page(s):250 – 262.

[60] S.E. George. M. Bocko and G.W. Nickerson, "Evaluation of a vibration-powered, wireless temperature sensor for health monitoring", IEEE Aerospace Conference 5-12 March 2005, Page(s):3775 – 3781.

[61] S. George, "Development of a vibration-powered wireless temperature sensor and accelerometer for health monitoring", IEEE Aerospace Conference 4-11 March 2006, Page(s):1 – 8.

[62] D. Nickles, D. Rauth, and J. Schmalzel, "Enhanced smart sensor for integrated system health management", IEEE Proceedings of Sensors Applications Symposium 2006, Page(s):208 – 212.

[63] Hossain, "An intelligent sensor network system coupled with statistical process model for predicting machinery health and failure", Sensors for Industry Conference, 2nd ISA/IEEE, 19-21 Nov. 2002, Page(s):52–56.

[64] S.A. Lewis and T.G. Edwards, "Smart sensors and system health management tools for avionics and mechanical systems", Digital Avionics Systems Conference (DASC) AIAA/IEEE, 26-30 Oct. 1997, Volume 2, Page(s):8.5 - 1- 8.5-7.

[65] C.Y. Wong, and S.J. Hood, "Impact of process monitoring in semiconductor manufacturing", Proceedings of 16th IEEE/CPMT International Electronics Manufacturing Technology (IEMT) Symposium, Vol. 1, Sep. 1994 Page(s): 221-225.

[66] C. Eaves-Walton, K. Hunt, and S. Redford, "Intelligent online process monitoring and fault isolation", IEE Colloquium on Condition Monitoring and Failure Diagnosis - Part 1, Vol. 1, Nov. 1988, page(s): 6/1-6/4,.

[67] Lin, K.C.; Marcadal, C.; Ganguli, S.; Zheng, Bo; Schmitt, J. and Chen, Ling "Characterization of copper CVD process by a process monitor", IEEE/SEMI Advanced Semiconductor Manufacturing Conference and Workshop, pp. 440-445, Sept. 1999.

[68] Kojima, T.; Miyajima, M.; Akaboshi, F.; Yogo, T.; Ishimoto, S. and Okuda, A. "Application of CMP process monitor to Cu polishing", IEEE Transactions on Semiconductor Manufacturing, Vol. 13, Issue 3, pp. 293-299, Aug. 2000.

[69] Brokelmann, M.; Wallaschek, J. and Hesse, H. "Bond process monitoring via self-sensing piezoelectric transducers", Proceedings of the IEEE International

Frequency Control Symposium and Exposition, pp. 125-129, Aug. 2004.

[70] Kalashnikov, A.N.; Ivchenko, V.; Challis, R.E. and Holmes, A.K. "Compensation for temperature variation in ultrasonic chemical process monitoring", 2005 IEEE Ultrasonics Symposium, Vol. 2 pp. 1151-1154, Sept. 2005.

[71] Suman, S.; Gaitan, M.; Joshi, Y. and Harman, G.G. "Wire-bonding process monitoring using thermopile temperature sensor", IEEE Transactions on Advanced Packaging, Vol. 28, Issue 4, pp. 685-693, Nov. 2005.

[72] Sopori, B.; Zhang, Yi; Chen, Wei and Madjdpour, J. "BSilicon solar cell process monitoring by PV-reflectometer", Conference Record of the 28th IEEE Photovoltaic Specialists Conference, pp. 120-123, Sept. 2000.

[73] http://en.wikipedia.org/wiki/Temperature_measure (Date: 30/10/2010)

[74] http://en.wikipedia.org/wiki/Temperature_measure#Temperature_measurement (Date: 30/10/2010)

[75] http://www.temperatures.com/ (Date: 30/10/2010)

[76] Peter Orrell, "how to measure temperature", Sensor Review, Vol. 15 No. 4, 1995, Page(s):28 – 30.

[77] http://www.temperatures.com/tcs.html (Date: 30/10/2010)

[78] http://www.facstaff.bucknell.edu/mastascu/elessonshtml/Sensors/TempThermCpl.html (Date: 30/10/2010)

[79] http://www.dbanks.demon.co.uk/ueng/thermsens.html (Date: 30/10/2010)

[80] J.J. Park and M. Taya, "Micro-temperature sensor array with thin-film thermocouples", Electronics Letters, Volume 40, Issue 10, 13 May 2004, Page(s):599 – 601.

[81] K. Miyazaki, T. Takamiya and H. Tsukamoto, "Fabrication of micro-thin film thermocouples", International Conference on Thermoelectrics (ICT), 17-21 Aug. 2003, Page(s):673 – 676.

[82] http://www.kele.com/tech/monitor/temperature/TRefTem4.html (Date: 30/10/2010)

[83] http://www.temperatures.com/rtds.html (Date: 30/10/2010)

[84] http://www.ussensor.com/technical_data.html (Date: 30/10/2010)

[85] T. Bernstein and Pao Ping Chang, "Calculation of Self-Heating Current for a Resistance Wire Temperature Sensor", IEEE Transactions on Industrial Electronics and Control Instrumentation (IECI), Vol. 16, Issue 1, July 1969 Page(s):99 – 102.

[86] http://www.allaboutcircuits.com/vol_1/chpt_12/6.html (Date: 30/10/2010)

[87] http://www.nuist.edu.cn/wlsy/show.aspx?id=517&cid=29 (Date: 30/10/2010)

[88] Julian W. Gardner, Microsensors: principle and application, Bookcraft (bath) Ltd. 1994, Great Britain. Chapter 5.

[89] http://hyperphysics.phy-astr.gsu.edu/hbase/Tables/rstiv.html (Date: 30/10/2010)

[90] http://www.lakeshore.com/temp/sen/prtd.html (Date: 30/10/2010)

[91] http://en.wikipedia.org/wiki/Infrared_thermometer (Date: 30/10/2010)

[92] M. Miiller, W. Budde, R. Gottfried-Gottfi-ied, etc., "A Thermoelectric Infrared Radiation Sensor With Monolithically Integrated Amplifier Stage And Temperature Sesnor", The 8th International Conference on Solid-state Sensors and Actuators, and Eurosensors IX. Stockholm, Sweden, 25-29, June 1995, Page(s):640 – 643.

[93] K. Shinzato, J. Ishii, Y. Shimizu, etc., "High-speed Infrared Radiation Thermometers for Measurement of Thermophysical Properties", IEEE SICE Osaka, Aug. 5-7.2002, Page(s):2077 – 2081.

[94] Wook Jae Yoo, Bongsoo Lee, Dong Hyun Cho, etc., "Infrared Radiation Thermometer Using a Silver Halides Optical Fiber for Biomedical Applications", IEEE SENSORS 2006, EXCO, Daegu, Korea. 22-25 Oct. 2006, Page(s):631-633.

[95] http://en.wikipedia.org/wiki/Optical_Fiber#Fiber_optic_sensors (Date: 30/10/2010)

[96] Zhiyi Zhang, K. T. V. Grattan and A. W. Palmer, "Fiber optic temperature sensor based on the cross referencing between blackbody radiation and fluorescence lifetime", Review of Scientific Instruments, May 1992, Vol. 63, Issue 5, Page(s):3177-3181.

[97] Jonghan Park, Gabriele Bolognini, Duckey Lee, etc., "Raman-Based Distributed Temperature Sensor With Simplex Coding and Link Optimization", IEEE PHOTONICS TECHNOLOGY LETTERS, VOL. 18, NO. 17, Sep. 2006, Page(s):1879-1881.

[98] V. 3. Kados and G. J. Sonek, "A Dewpoint Temperature Sensor Based on Nd3+-Doped Fiber Fluorescence", IEEE PHOTONICS TECHNOLOGY LETTERS, VOL. 7, NO. 10, Oct. 1995, Page(s):1198-1200.

[99] Alberto Álvarez-Herrero, H. Guerrero, T. Belenguer, etc., "High-Sensitivity Temperature Sensor Based on Overlay on Side-Polished Fibers", IEEE PHOTONICS TECHNOLOGY LETTERS, VOL. 12, NO. 8, Aug. 2000, Page(s):1043-1045.

[100] Javier Senosiain, Idoya Díaz, Ainhoa Gastón, etc., "High Sensitivity Temperature Sensor Based on Side-Polished Optical Fiber", IEEE TRANSACTIONS ON INSTRUMENTATION AND MEASUREMENT, VOL. 50, NO. 6, DECEMBER 2001, Page(s):1656-1660.

[101] Pak Lim Chu and Danny Wong, "Phase Sensitivity of Polarization-Maintaining Optical Fiber Used as Temperature Sensor", JOURNAL OF LIGNTWAVE TECHNOLOGY, VOL. LT-4. NO. I , JANUARY 1986, Page(s):41-49.

[102] C.F.R. Mateus and C.L. Barbosa, "Low Power, High Sensitivity Temperature Sensor Using Fiber Bragg Gratings and VCSEL", IEEE Lasers & Electro-Optics Society, Oct. 2006 Page(s):354 – 355.

[103] Tyson L. Lowder, Kevin H. Smith, Benjamin L. Ipson, etc., "High-Temperature Sensing Using Surface Relief Fiber Bragg Gratings", IEEE PHOTONICS TECHNOLOGY LETTERS, VOL. 17, NO. 9, Sep. 2005, Page(s):1926 – 1928.

[104] Bowei Zhang and Mojtaba Kahrizi, "High-Temperature Resistance Fiber Bragg Grating Temperature Sensor Fabrication", IEEE SENSORS JOURNAL, VOL. 7, NO. 4, Apr. 2007, Page(s):586– 591.

[105] Jian Ju, Zhi Wang, Wei Jin, etc., "Temperature Sensitivity of a Two-Mode Photonic Crystal Fiber Interferometric Sensor", IEEE PHOTONICS TECHNOLOGY LETTERS, VOL. 18, NO. 20, Oct. 15, 2006, Page(s):2168–2170.

[106] Hak-Rin Kim, Eunje Jang and Sin-Doo Lee, "Electrooptic Temperature Sensor

146

Based on a Fabry–Pérot Resonator With a Liquid Crystal Film", IEEE PHOTONICS TECHNOLOGY LETTERS, VOL. 18, NO. 8, APRIL 15, 2006, Page(s): 905– 907.

[107] http://en.wikipedia.org/wiki/Diode (Date: 30/10/2010)

[108] http://www.vias.org/feee/sensor_temp_diode.html (Date: 30/10/2010)

[109] Raimundo Carlos Silverio Freire, SCrgio Daher, and Gurdip Singh Deep, A Highly Linear Single p-n Junction Temperature Sensor, IEEE TRANSECTIONS ON INSTRUMENTATION AND MEASUREMENT, VOL. 43, NO. 2, APRIL 1994, Page(s): 127-132.

[110] Yu. M. Shwarts, A. V. Kondrachuk, M. M. Shwarts, L. I. Spinar, and E. F. Venger, The effect of heterojunction properties of the diode temperature sensors on low temperature current transfer and temperature response curves, the third international European conference on advanced semiconductor devices and microsystems, Smolenice Castle, Slovakia, 16-18 Pct. 2000, Page(s): 453-456.

[111] S. Santra, P. K. Guha, S. Z. Ali, I. Haneef, F. Udrea, and J. W. Gardner, SOI Diode Temperature Sensor Operated at Ultra High Temperatures – A Critical Analysis, IEEE SENSORS Conference 2008, Page(s): 78-81.

[112] A. Poyai, E. Ratanaudomphisut, J. Supadech, N. Klunngien, C. Hruanan, and S. Sophitpan, Improving Sensitivity of p-n Junction Temperature Sensor by Carrier Lifetime Modification, Advanced Materials Research Vols. 55-57 (2008) Page(s): 517-520.

[113] http://en.wikipedia.org/wiki/Humidity (Date: 30/10/2010)

[114] http://en.wikipedia.org/wiki/Humidity#Measuring_and_regulating_humidity (Date: 30/10/2010)

[115] http://www.71168.cn/2006/2006-8-17/2006817132500.shtml (Date: 30/10/2010)

[116] http://www.chinashidu.com.cn/news_detail.php?id=189&nowmenuid=18&cpath =&catid=0 (Date: 30/10/2010)

[117] http://special.power.net.cn/js/spgkjs/spcgqyyb/171733CD7G13EMXLTU321M S4HNP.shtml (Date: 30/10/2010)

[118] Mehmet Dokmeci and Khalil Najafi, "A High-Sensitivity Polyimide Capacitive

Relative Humidity Sensor for Monitoring Anodically Bonded Hermetic Micropackages", JOURNAL OF MICROELECTROMECHANICAL SYSTEMS, VOL. 10, NO. 2, JUNE 2001, Page(s):197– 204.

[119] Uksong Kang and Kensall D. Wise, "A High-Speed Capacitive Humidity Sensor with On-Chip Thermal Reset", IEEE TRANSACTIONS ON ELECTRON DEVICES, VOL. 47, NO. 4, Apr. 2000, Page(s):702– 710.

[120] A. Tetelin, C. Pellet and A. Achen, "Capacitive humidity sensors based on oxidized PhotoBCB polymer films: enhanced sensitivity and response time", IEEE conference on Sensors 30 Oct.-3 Nov. 2005, Page(s):564– 567.

[121] A. Tetelin and C. Pellet, "Accurate model of the dynamic response of a capacitive humidity sensor", Proceedings of IEEE Sensors, 22-24 Oct. 2003, Vol. 1, Page(s):378 – 383.

[122] Angie Tetelin and Claude Pellet, "Modeling and Optimization of a Fast Response Capacitive Humidity Sensor", IEEE SENSORS JOURNAL, VOL. 6, NO. 3, JUNE 2006, Page(s):714– 720.

[123] http://en.wikipedia.org/wiki/Pressure (Date: 30/10/2010)

[124] http://en.wikipedia.org/wiki/Stress (Date: 30/10/2010)

[125] Lecture- Pressure, stress, elastic moduli and density, Michigan State University, http://www.pa.msu.edu/~duxbury/courses/phy231/Lecture21.pdf
(Date: 30/10/2010)

[126] http://en.wikipedia.org/wiki/Strain_gauge (Date: 30/10/2010)

[127] Minhang Bao, "Analysis and Design Principles of MEMS Devices", 2005 Shanghai.

[128] Dazhong Jin, "Micromechanical resonant cantilever sensors for bio/chemical detection", PhD dissertation, May 2006, Shanghai.

[129] Xuemeng Chen, "Research of Piezoresistive Micromachined Gyroscope", PhD dissertation, May 2005, Shanghai.

[130] K.SIVAKUMAR, N.DASGUPTA and K.N.BHAT, "Sensitivity Enhancement of Polysilicon Piezo-resistive Pressure Sensors with Phosphorous Diffused Resistors", International MEMS Conference 2006, Journal of Physics:

Conference Series 34 (2006) 216–221.

[131] Lecture material, "Piezoresistivity", Montana State University TjK Reading: pp. 431-435 Chp 5-#14

[132] http://knol.google.com/k/saeed/mems/1xi2igbq9vg0e/2# (Date: 30/10/2010)

[133] Ranjit Singh, Low Lee Ngo, Ho Soon Seng, et al. "A silicon piezoresistive pressure sensor", Electronic Design, Test and Applications, 2002. Proceedings. The First IEEE International Workshop on 29-31 Jan. 2002, Page(s):181 – 184.

[134] Min-Xin Zhou, Qing-An Huang, Ming Qin, et al., "A Novel Capacitive Pressure Sensor Based on Sandwich Structures", JOURNAL OF MICROELECTROMECHANICAL SYSTEMS, VOL. 14, NO. 6, Dec. 2005, Page(s):1272 – 1282.

[135] K.R. Lee, K. Kim, Y.K. Kim, et al., "CAPACITIVE ABSOLUTE PRESSURE SENSOR WITH VACUUM CAVITY FORMED BY BONDING SILICON TO SOIWAFER FOR UPPER AIR OBSERVATIONS", 19th IEEE International Conference on Micro Electro Mechanical Systems, Istanbul. 2006, Page(s):618 – 621.

[136] http://www.allaboutcircuits.com/vol_1/chpt_12/6.html (Date: 30/10/2010)

[137] http://hyperphysics.phy-astr.gsu.edu/hbase/electric/restmp.html
(Date: 30/10/2010)

[138] http://en.wikipedia.org/wiki/Finite_element_method (Date: 30/10/2010)

[139] http://en.wikipedia.org/wiki/ANSYS, http://www.ansys.com (Date: 30/10/2010)

[140] F. Niklaus, H. Andersson, P. Enoksson, and G. Stemme, "Low Temperature Full Wafer Adhesive Bonding of Structured Wafers," Sensors and Actuators A, Vol. 92, No. 1 (2001), pp. 235-241.

[141] F. Niklaus, G. Stemme, J.Q. Lu and R.J. Gutmann, "Adhesive wafer bonding," J. Appl. Phys. 99, 031101 (2006).

[142] Dow Chemical Company, "Processing Procedures For CYCLOTENE 4000 Series Resin (DS3000 Immersion Develop Process)," pp. 1-9, Feb. 2005.

[143] Dow Chemical Company, "CYCLOTENE 4000 Resin Hot Plate Curing," dow/cyclotene/solution/4000 resins. (Date: 30/10/2010)

[144] Jourdain, P. De Moor, S. Pamidighantam, and H.A.C. Tilmans, "Investigation of the hermeticity of BCB-sealed cavities for housing (RF-)MEMS devices," Proc 15th Micro Electro Mechanical Systems Conf., Vegas, NV, Jan. 2002, pp. 667-680.

[145] J. Oberhammer, F. Nickaus, and G. Stemme, "Selective Wafer-level Adhesive Bonding with Benzocyclobutene for Fabrication of Cavities," Sensors and Actuators, Vol. 105, No. 3 (2003) pp. 297–304.

[146] Jourdain, P. De. Moor, K. Baert, I. De. Wolf, and H. A. C. Tilmans, "Mechanical and Electrical Characterization of BCB as A Bond and Seal Material for Cavities Housing (RF-) MEMS Devices," Journal of Micromechanics and Microengineering, Vol. 15, No. 7 (2005), pp. S89–S96.

[147] S. Seok, N. Rolland and P-A. Rolland, "Packaging Methodology For RF Devices Using A BCB Membrane Transfer Technique", Journal of Micromechanics and Microengineering, Vol. 16 (2006), pp. 2384–2388.

[148] S. Seok, N. Rolland and P-A. Rolland, "Design, Fabrication, and Measurement of Benzocyclobutene Polymer Zero-Level Packaging For Millimeter-Wave Applications," IEEE Transactions on Microwave Theory and Techniques, Vol. 55, No. 5 (2007), pp. 1040-1045.

[149] S. Seok, N. Rolland and P-A. Rolland, "Mechanical and Electrical Characterization of Benzocyclobutene Membrane Packaging," Proc 2007 Electronic Components and Technology Conference, Nevada USA, May 2007, pp. 1685-1689.

[150] F. Bardin, S. Kloss, C.H. Wang, A.J. Moore, A. Jourdain, I.De Wolf, and D.P. Hand, "Laser Bonding of Glass to Silicon Using Polymer for Microsystems Packagin", Journal of Microelectromechanical Systems, Vol. 16, Issue 3, June 2007, pp. 571-580.

[151] C. H. Wang, J. Zeng, K. Zhao, and H. L. Chan, "Chip Scale Studies of BCB Based Polymer Bonding for MEMS Packaging," Proc 58th Electronic Components and Technology Conf, Lake Buena Vista, FL, May 2008, pp. 1869-1873.

[152] Q. Wu, S. Kloss, N. Lorenz, C.H. Wang, A.J. Moore, and D.P. Hand, "Localised Laser joining of glass to silicon with BCB intermediate layer," Proceedings of

the 3rd Pacific International Conference on Application of Lasers and Optics, Apr. 2008, P202.

[153] D. Rebiere, C. Dejous, J. Pistre, J-F.Lipskier, and R. Planade, SAW organophosphorus sensors coated with fluoropolyol isomers: role of humidity and temperature on the sensitivity,1997 International Conference on Solid State Sensors and Actuators, 1997. TRANSDUCERS '97 Chicago USA, vol.2 pp.: 1331-1334.

[154] S. Furukawa, M. Obana, and T. Nomura, New SAW humidity sensor using double-coated hygroscopic film, 1995 IEEE Proceedings of Ultrasonics Symposium, vol.1, pp.: 539-542.

[155] Y.-T. Chen, and H.L. Kao, Humidity sensors made on polyvinyl-alcohol film coated saw devices, Electronics Letters Volume: 42, Issue: 16 (2006), pp.: 948-949.

[156] A. Tetelin, A. Achen, V. Pouget, C. Pellet, M. Topper, and J.-L. Lachaud, Water Solubility and Diffusivity in BCB Resins used in Microelectronic Packaging and Sensor Applications, Proceedings of the 2005 IEEE Instrumentation and Measurement Technology Conference (IMTC 2005), Vol. 2, pp.: 792-796。

[157] A. Tetelin, V. Pouget, J.-L. Lachaud, and C. Pellet, Dynamic behavior of a chemical sensor for humidity level measurement in human breath, IEEE Transactions on Instrumentation and Measurement Volume: 53 , Issue: 4, 2004. Page(s): 1262 - 1267.

[158] C. Laville, and C. Pellet, Comparison of three humidity sensors for a pulmonary function diagnosis microsystem, IEEE Sensors Journal, Volume: 2 , Issue: 2, 2002 , Page(s): 96 - 101.

[159] C. Laville, and C. Pellet, Interdigitated humidity sensors for a portable clinical microsystem, IEEE Transactions on Biomedical Engineering, Volume: 49 , Issue: 10, 2002 , Page(s): 1162 - 1167.

[160] Dow Chemical Company, "Processing Procedures For CYCLOTENE 4000 Series Resin (DS2100 Puddle Develop Process)," pp. 1-9, Feb. 2005.

[161] Dow Chemical Company, "Rework Procedures for CYCLOTENE 3000 Series and 4000 Series Resins," pp. 1-3, Feb. 2005.

[162] J. Wu, R. Pike, C.P. Wong, D. Scheck, W.B. Rogers, and P. Garrou, Evaluation of the environmental protection of photo BCB polymers (Cyclotene^{TM} 4000), Proceedings of 2000 International Symposium on Advanced Packaging Materials: Processes, Properties and Interfaces, 2000, pp.: 90 – 96.

[163] Lord Rayleigh "On Waves Propagated along the Plane Surface of an Elastic Solid", Proc. London Math. Soc. s1-17 (1885), pp.: 4-11.

[164] http://en.wikipedia.org/wiki/Piezoelectricity (Date: 30/10/2010)

[165] PZT Application Manual: The Piezoelectric Effect, Http://www.aurelienr.com/electronique/piezo/piezo.pdf (Date: 30/10/2010)

[166] Damjanovic, Dragan (1998). "Ferroelectric, dielectric and piezoelectric properties of ferroelectric thin films and ceramics". Reports on Progress in Physics 61 (1998), pp.: 1267–1324.

[167] B. Drafts, Acoustic wave technology sensors, IEEE Transactions on Microwave Theory and Techniques, Vol. 49, Issue: 4 (2001), pp.: 795-802.

[168] LITHIUM NIOBATE LiNbO$_3$, lmaz Optics, Inc. USA, http://www.almazoptics.com/LiNbO3.htm (Date: 30/10/2010)

[169] http://download.autodesk.com/us/algor/userguides/mergedProjects/setting_up_the_analysis/linear/Materials/piezoelectric_material_properties.htm
(Date: 30/10/2010)

[170] Lithium Niobate Material Quality Classification, Crystal Technology Inc. USA, http://www.crystaltechnology.com/docs/LNMaterialQuality.pdf
(Date: 30/10/2010)

[171] David Alan Cohen, LITHIUM NIOBATE MICROPHOTONIC MODULATORS, PhD thesis of GRADUATE SCHOOL UNIVERSITY OF SOUTHERN CALIFORNIA, May 2001.

[172] S. Jen, and R. Bobkowski, Black lithium niobate SAW device fabrication and performance evaluation, 2000 IEEE Ultrasonics Symposium, vol.1 (2000) pp.: 269-273.

[173] E.M. Standifer, D.H. Jundt, R.G. Norwood, and P.F. Bordui, Chemically reduced lithium niobate single crystals: processing, properties and improvements in SAW device fabrication and performance, Proceedings of the 1998 IEEE

International Frequency Control Symposium, pp.: 470-472.

[174] P.F. Bordui, D.H. Jundt, E.M. Standifer, R.G. Norwood, R.L. Sawin, and J.D. Galipeau, Chemically reduced lithium niobate single crystals: Processing, properties and improved surface acoustic wave device fabrication and performance, Journal of Applied Physics, Vol. 85, Issue: 7 (1999), pp.: 3766-3769.

[175] T. Shigematsu, and M.K. Kurosawa, Stability Improvement of Surface Acoustic Wave Motor using Chemically Reduced Lithium Niobate, International Solid-State Sensors, Actuators and Microsystems Conference, 2007 (TRANSDUCERS 2007), pp.: 1163-1166.

[176] Lithium Niobate Wafers Free of Pyro-Electric ffect,The Roditi International Corporation Ltd, UK. http://www.roditi.com/SingleCrystal/LiNbO3/liNBO3%20Black%20Wafers.html (Date: 30/10/2010)

[177] Principle Analysis of the SAW LC Resonator, http://adm.elecfans.com/baike/bandaoti/bandaotiqijian/20100308183034.html (Date: 30/10/2010)

[178] T.Nomura, K.Oofuchi, T.Yasuda, and S.Furukawa, SAW Humidity Sensor Using Dielectric Hygroscopic Polymer Film, 1994 IEEE Proceedings of Ultrasonics Symposium, 01 - 04 Nov 1994, Cannes , France, vol.1, pp.: 503 - 506.

[179] Jay W. Grate, Stephen J. Martin, and Richard M. White, Acoustic Wave Microsensors Part I, Analytical Chemistry, 1st Nov. 1993, Vol. 65, No. 21, pp.: 940 – 948.

[180] Peter A. Lieberzeit, Christian Palfinger, Franz L. Dickert, and Gerhard Fischerauer, SAW RFID-Tags for Mass-Sensitive Detection of Humidity and Vapors, sensors 2009, Vol 9, pp.: 9805-9815. http://www.mdpi.com/1424-8220/9/12/9805/pdf. (Date: 30/10/2010)

[181] Kofi Korsah, C.L. Ma, and Bill Dress, Harmonic frequency analysis of SAW resonator chemical sensors: application to the detection of carbon dioxide and humidity, Sensors and Actuators B Vol. 50, 1998, pp.: 110 – 116.

[182] William WILSON, and Gary ATKINSON, Comparison of Transmission Line

Methods for Surface Acoustic Wave Modeling, Sensors & Transducers Journal, Vol. 7, Special Issue, October 2009, pp.: 150 - 159.

[183] C.S. Hartmann Jr., D.T. Bell, and R.C. Rosenfeld, Impulse Model Design of Acoustic Surface-Wave Filters, IEEE Transactions on Microwave Theory and Techniques, Vol.: 21, Issue:4, Apr 1973, pp.: 162 - 175.

[184] C. Campbell, Surface Acoustic Wave Devices for Mobile and Wireless Communications, New York, NY, Academic Press, 1998.

[185] Yi Liu, and Tianhong Cui, Power consumption analysis of surface acoustic wave sensor systems using ANSYS and PSPICE, Microsyst Technol, Vol.: 13, 2007, pp.: 97 – 101.

[186] Ewald Benes, Martin Groschl, Franz Seifert, and Alfred Pohl, Comparison Between BAW and SAW Sensor Principles, ieee transactions on ultrasonics, ferroelectrics, and frequency control, vol. 45, no. 5, september 1998, pp.: 1314 - 1330

[187] C. Caliendo, E. Verona, A. D'Amico, A. Furlani, G. Iucci, and M.V. Russo, Surface acoustic wave humidity sensor, Sensors and Actuators B: Chemical, Vol. 16, Issues 1-3, October 1993, pp.: 288 - 292.

[188] Bill Drafts, Acoustic Wave Technology Sensors, IEEE TRANSACTIONS ON MICROWAVE THEORY AND TECHNIQUES, VOL. 49, NO. 4, APRIL 2001, pp.: 795 - 802.

[189] N. Saldanha, D. Puccio, and D. C. Malocha, Experimental Measurements and Modeling of Aluminum Reflection Gratings on YZ LiNbO$_3$ for OFC SAW Sensors, 2006 IEEE International Frequency Control Symposium and Exposition, pp.: 368-373.

[190] TYCO ELECTRONICS - 1-1478979-0 - SOCKET, SMA, PCB, STRAIGHT, http://uk.farnell.com/jsp/displayProduct.jsp?sku=1056377&CMP=KNC-GUK-FUK-GEN-SKU-G12&s_kwcid=TC|13123|1-1478979-0||S|b|3947627859 (Date: 30/10/2010)

[191] Technical Data Sheet of Silver Loaded Epoxy, RS Components Ltd. UK, http://docs-europe.origin.electrocomponents.com/webdocs/04ad/0900766b804aded0.pdf (Date: 30/10/2010)

[192] 3M - 923690-40 - TEST CLIP, DIL, 40WAY, http://uk.farnell.com/3m/923690-40/test-clip-dil-40way/dp/178277?Ntt=TEST+CLIP,+DIL,+40WAY (Date: 30/10/2010)

[193] http://en.wikipedia.org/wiki/Q_factor (Date: 30/10/2010)

[194] W.H. Haydl, and P.S. Cross, Fine tuning of surface-acoustic-wave resonator filters with metallisation thickness, Electronics Letters, Vol. 11, Issue: 12 (1975), pp.: 252-253.

[195] R.T. Smith, and F.S. Welsh, Temperature Dependence of the Elastic, Piezoelectric, and Dielectric Constants of Lithium Tantalate and Lithium Niobate, Journal of Applied Physics, Vol. 42, Issue: 6 (1971), pp.: 2219-2230.

[196] R. Hauser, L. Reindl, and J. Biniasch, High-temperature stability of $LiNbO_3$ based SAW devices, 2003 IEEE Symposium on Ultrasonics, Vol. 1, pp.: 192-195。

[197] Dazhong Jin, PhD thesis 2006, Micromechanical resonant cantilever sensors for bio/chemical detection, shanghai institute of microsystem and information technology, chinese academia of science.

[198] C.H. Wang, Y. Liu, M. Desmulliez, and A. Richardson. Integrated sensors for health monitoring in advanced electronic systems. Proceedings of 4th International Design and Test Workshop 2009, IDT 2009, Riyadh, Saudi Arabia. pp. 1-6.